# Applying Engineered Logjams and Dolosse for Streambank Stabilization

PUBLICATION NO. FHWA-HRT-21-028

FEBRUARY 2021

U.S. Department of Transportation
**Federal Highway Administration**

Research, Development, and Technology
Turner-Fairbank Highway Research Center
6300 Georgetown Pike
McLean, VA 22101-2296

## FOREWORD

Environmentally compatible and cost-effective strategies for stream stabilization are needed to protect transportation infrastructure adjacent to river corridors and sustain riverine functions. In this study, physical and numerical modeling of engineered logjams for stream stabilization is evaluated and proposed design guidelines are provided. The study will be useful for bridge and roadway personnel responsible for the hydraulic design of the Nation's transportation infrastructure. The study described in this report was conducted at the Federal Highway Administration Turner-Fairbank Highway Research Center J. Sterling Jones Hydraulics Laboratory.

Cheryl Allen Richter, Ph.D., P.E.
Director, Office of Infrastructure
Research and Development

# TECHNICAL DOCUMENTATION PAGE

| 1. Report No.<br>FHWA-HRT-21-028 | 2. Government Accession No. | 3. Recipient's Catalog No. |
|---|---|---|
| 4. Title and Subtitle<br>Applying Engineered Logjams and Dolosse for Streambank Stabilization | | 5. Report Date<br>February 2021 |
| | | 6. Performing Organization Code |
| 7. Author(s)<br>Oscar Suaznabar, Zhaoding Xie, Roger Kilgore, Sven Leon, Daniel Pastrich, Christoph Zuelow, Chao Huang (ORCID: 0000-0002-6034-8637), and Kornel Kerenyi | | 8. Performing Organization Report No. |
| 9. Performing Organization Name and Address<br>Genex Systems, LLC<br>11848 Rock Landing Drive, Suite 303<br>Newport News, VA 23606 | | 10. Work Unit No. |
| | | 11. Contract or Grant No.<br>DTFH61-16-D-00033-T-0003 |
| 12. Sponsoring Agency Name and Address<br>Office of Infrastructure Research and Development<br>Federal Highway Administration<br>6300 Georgetown Pike<br>McLean, VA 22101 | | 13. Type of Report and Period Covered<br>Research Report;<br>January 2016–August 2019 |
| | | 14. Sponsoring Agency Code<br>HRDI-40 |

15. Supplementary Notes
The Contracting Officer's Representative was Kornel Kerenyi (HRDI-40).

16. Abstract
Engineers at the Federal Highway Administration Western Federal Lands Highway Division are installing long-term streambank stabilization intended to preserve highway infrastructure as well as minimize environmental impacts. An emerging approach called "engineered logjams" (ELJs), which uses precast concrete dolosse (i.e., reinforced concrete blocks in a complex geometric shape), is being considered for use in the Upper Hoh River Road bank-stabilization project. ELJs mimic logjams found in nature. Such logjams can redirect the channel flow and mitigate destructive erosive forces. As an additional benefit, the logs and debris can create or enhance fish habitat. A 1:25 scale model of a proposed ELJ design was tested in a flume for different flow conditions on movable bed and bank material. The physical modeling was complemented by computational fluid dynamic (CFD) modeling to investigate the stability of proposed ELJ installations during floods and to advance the design of ELJs for streambank stabilization.

Several findings emerged from the cases evaluated in this research project: (1) ELJs proved to be effective in deflecting high-velocity approach flows away from the erodible streambank into the main channel; (2) results obtained from the ELJ model with loose bed and bank material showed that localized streambed scour around the structure does have an effect on its stability; (3) the effectiveness of structural modifications to the ELJs, such as the placement of key dolosse, addition of riprap, and partial burial of the ELJ was determined; and (4) a repeatable ELJ unit design can provide structural stability against high-velocity flows and streambed scour with an appropriate combination of wood and ballast meeting specific density and void ratio requirements. In addition, this study derived drag coefficients for this type of ELJ unit based on force measurements and CFD modeling. Future work is needed to evaluate the transferability of these findings to other ELJ types and configurations. This research study achieved the main goal of creating environmentally friendly streambank protection and local fish habitat. Findings from this research study will be of interest to river engineering designers who may build similar structures for streambank stabilization projects.

| 17. Key Words | 18. Distribution Statement |
|---|---|
| Engineered logjam, stream stabilization, dolos, dolosse, large woody debris, logjam stability, computational fluid dynamics | No restrictions. This document is available to the public through the National Technical Information Service, Springfield, VA 22161.<br>http://www.ntis.gov |

| 19. Security Classif. (of this report) | 20. Security Classif. (of this page) | 21. No. of Pages | 22. Price |
|---|---|---|---|
| Unclassified | Unclassified | 112 | N/A |

## SI* (MODERN METRIC) CONVERSION FACTORS

### APPROXIMATE CONVERSIONS TO SI UNITS

| Symbol | When You Know | Multiply By | To Find | Symbol |
|---|---|---|---|---|
| | | **LENGTH** | | |
| in | inches | 25.4 | millimeters | mm |
| ft | feet | 0.305 | meters | m |
| yd | yards | 0.914 | meters | m |
| mi | miles | 1.61 | kilometers | km |
| | | **AREA** | | |
| $in^2$ | square inches | 645.2 | square millimeters | $mm^2$ |
| $ft^2$ | square feet | 0.093 | square meters | $m^2$ |
| $yd^2$ | square yard | 0.836 | square meters | $m^2$ |
| ac | acres | 0.405 | hectares | ha |
| $mi^2$ | square miles | 2.59 | square kilometers | $km^2$ |
| | | **VOLUME** | | |
| fl oz | fluid ounces | 29.57 | milliliters | mL |
| gal | gallons | 3.785 | liters | L |
| $ft^3$ | cubic feet | 0.028 | cubic meters | $m^3$ |
| $yd^3$ | cubic yards | 0.765 | cubic meters | $m^3$ |
| | **NOTE**: volumes greater than 1,000 L shall be shown in $m^3$ | | | |
| | | **MASS** | | |
| oz | ounces | 28.35 | grams | g |
| lb | pounds | 0.454 | kilograms | kg |
| T | short tons (2,000 lb) | 0.907 | megagrams (or "metric ton") | Mg (or "t") |
| | | **TEMPERATURE (exact degrees)** | | |
| °F | Fahrenheit | 5 (F-32)/9<br>or (F-32)/1.8 | Celsius | °C |
| | | **ILLUMINATION** | | |
| fc | foot-candles | 10.76 | lux | lx |
| fl | foot-Lamberts | 3.426 | $candela/m^2$ | $cd/m^2$ |
| | | **FORCE and PRESSURE or STRESS** | | |
| lbf | poundforce | 4.45 | newtons | N |
| $lbf/in^2$ | poundforce per square inch | 6.89 | kilopascals | kPa |

### APPROXIMATE CONVERSIONS FROM SI UNITS

| Symbol | When You Know | Multiply By | To Find | Symbol |
|---|---|---|---|---|
| | | **LENGTH** | | |
| mm | millimeters | 0.039 | inches | in |
| m | meters | 3.28 | feet | ft |
| m | meters | 1.09 | yards | yd |
| km | kilometers | 0.621 | miles | mi |
| | | **AREA** | | |
| $mm^2$ | square millimeters | 0.0016 | square inches | $in^2$ |
| $m^2$ | square meters | 10.764 | square feet | $ft^2$ |
| $m^2$ | square meters | 1.195 | square yards | $yd^2$ |
| ha | hectares | 2.47 | acres | ac |
| $km^2$ | square kilometers | 0.386 | square miles | $mi^2$ |
| | | **VOLUME** | | |
| mL | milliliters | 0.034 | fluid ounces | fl oz |
| L | liters | 0.264 | gallons | gal |
| $m^3$ | cubic meters | 35.314 | cubic feet | $ft^3$ |
| $m^3$ | cubic meters | 1.307 | cubic yards | $yd^3$ |
| | | **MASS** | | |
| g | grams | 0.035 | ounces | oz |
| kg | kilograms | 2.202 | pounds | lb |
| Mg (or "t") | megagrams (or "metric ton") | 1.103 | short tons (2,000 lb) | T |
| | | **TEMPERATURE (exact degrees)** | | |
| °C | Celsius | 1.8C+32 | Fahrenheit | °F |
| | | **ILLUMINATION** | | |
| lx | lux | 0.0929 | foot-candles | fc |
| $cd/m^2$ | candela/m2 | 0.2919 | foot-Lamberts | fl |
| | | **FORCE and PRESSURE or STRESS** | | |
| N | newtons | 2.225 | poundforce | lbf |
| kPa | kilopascals | 0.145 | poundforce per square inch | $lbf/in^2$ |

*SI is the symbol for International System of Units. Appropriate rounding should be made to comply with Section 4 of ASTM E380. (Revised March 2003)

## TABLE OF CONTENTS

## LIST OF FIGURES

## LIST OF TABLES

# LIST OF ACRONYMS AND SYMBOLS

## Acronyms

| | |
|---|---|
| 2D | two-dimensional |
| 3D | three-dimensional |
| CFD | computational fluid dynamics |
| CS | cross section |
| ELJ | engineered logjam |
| ERDC | U.S. Army Engineer Research and Development Center |
| FHWA | Federal Highway Administration |
| LES | large eddy simulation |
| MFS | multifunctional flume system |
| MP | mile post |
| RANS | Reynolds-averaged Navier–Stokes |
| TFHRC | Turner-Fairbank Highway Research Center |
| USBR | United States Bureau of Reclamation |
| H:V | horizontal to vertical (ratio) |
| VOF | volume of fluid |
| WFLHD | Western Federal Lands Highway Division |
| WSRCO | Washington State Recreation and Conservation Office |

## Symbols

| | |
|---|---|
| $(Re_g)r$ | particle (grain) Reynold's number ratio |
| $(SG-1)_r$ | specific gravity minus 1 ratio |
| $A_{ADJ}$ | adjacent cross-sectional area |
| $A_{elj}$ | ELJ area orthogonal to the flow |
| $A_r$ | area ratio |
| $A_U$ | area in the upstream cross section |
| $A_{up}$ | effective projected area of the upstream face of the engineered logjam unit |
| $C_D$ | drag coefficient |
| $(C_D)_r$ | drag coefficient ratio |
| $D_r$ | particle diameter ratio |
| $FB$ | freeboard requirement |
| $F_B$ | buoyancy force of the submerged portion of the engineered logjam |
| $F_D$ | drag force |
| $F_{D\text{-}CFD}$ | computational fluid dynamics modeling drag force |
| $(F_D)_r$ | drag-force ratio |
| $F_{fs}$ | resisting force |
| $F_{T\text{-}CFD}$ | computational fluid dynamics modeling transverse force |
| $Fr$ | Froude number |
| $Fr_m$ | Froude number for the model |
| $Fr_p$ | Froude number for the prototype |
| $Fr_r$ | Froude number ratio |
| $F_T$ | transverse force |

| | |
|---|---|
| $F_x$ | force in the $x$ direction |
| $F_y$ | force in the $y$ direction |
| $F_z$ | force in the $z$ direction |
| $g$ | gravitational acceleration |
| $g_r$ | gravitational acceleration ratio |
| $H_{BANK}$ | bank height |
| $H_{elj}$ | design height of the engineered logjam |
| $H_{elj–FB}$ | minimum height of the engineered logjam unit based on the freeboard requirement |
| $H_{elj–SM}$ | minimum height of the engineered logjam unit based on a stability model |
| $k_{elj}$ | surface roughness of the engineered logjam |
| $L$ | characteristic length scale |
| $L_{elj}$ | length of an ELJ unit |
| $L_r$ | length ratio |
| $L_s$ | spacing length between ELJ units |
| $m_T$ | total engineered logjam mass |
| $Re$ | Reynolds number |
| $R_r$ | hydraulic radius ratio |
| $SF$ | safety factor |
| $S_r$ | slope ratio |
| $T_x$ | torque in the $x$ direction |
| $T_y$ | torque in the $y$ direction |
| $T_z$ | torque in the $z$ direction |
| $V_{ADJ}$ | velocity in the channel adjacent to the engineered logjam |
| $V_{Failure}$ | velocity at failure |
| $V_0$ | characteristic velocity |
| $v_r$ | velocity ratio |
| $V_M$ | characteristic velocity in the model |
| $V_P$ | characteristic velocity in the prototype |
| $V_U$ | velocity in the upstream approach |
| $W_{BED}$ | bed width |
| $W_{elj}$ | base width |
| $\beta$ | measure of orientation of the engineered logjam with respect to flow direction |
| $y_0$ | characteristic flow depth |
| $y_U$ | upstream flow depth |
| $\gamma_r$ | unit weight of water ratio |
| $\eta$ | porosity of the engineered logjam |
| $\theta_r$ | dimensionless shear stress ratio |
| $\mu$ | friction coefficient between the ELJ and the streambed |
| $\rho$ | density of water |
| $\rho_{elj}$ | average density of the engineered logjam unit |
| $\rho_r$ | density of water ratio |
| $\forall_{elj}$ | volume of the engineered logjam unit |

# CHAPTER 1. INTRODUCTION

In gravel-bed rivers, natural logjams can form stable "hard points" within the channel migration zone and limit bank erosion (Abbe et al. 2003a). It was this observation of natural processes that led to the expanding use of engineered logjams (ELJs) to address channel instabilities, including bank erosion, entrenchment, head cutting, and other undesirable trends that not only reduce the ecological function of rivers and streams but also threaten transportation and other infrastructure.

ELJs have been deployed to protect streambanks from erosion while increasing channel complexity and the ecological value of the riverine environment. While experience in designing and constructing ELJs is increasing, as discussed in the literature review in chapter 2, significant uncertainty about their design and long-term performance remains. Much of this uncertainty results from the complexity and variability of potential ELJ configurations as well as the unique nature of each site at which they may be applied.

This report describes an application of ELJs in two reaches of the Hoh River in Washington State intended to protect the Upper Hoh River Road. To support the design of this project, the Western Federal Lands Highway Division (WFLHD) of the Federal Highway Administration (FHWA) requested that FHWA's Turner-Fairbank Highway Research Center (TFHRC) investigate selected aspects of ELJ design procedures to not only support the Upper Hoh River Road project but also add to the knowledge base for other ELJ projects.

The remainder of this chapter provides a summary of the research objectives for this project and a description of the Upper Hoh River Road project. Chapter 2 summarizes a literature review on ELJs as well as modeling and analysis of ELJs to date. Chapter 3 and chapter 4 describe the physical and numerical modeling, respectively, conducted for this project. Chapter 5 summarizes the results of the experiments and provides design recommendations. Finally, chapter 6 summarizes the project. Appendix A provides design details from a WFLHD project, and appendix B illustrates recommended practices from this research through a design example.

## RESEARCH OBJECTIVES

The research described in this report was conceived and implemented specifically to support an ELJ design for protecting the Upper Hoh River Road and, more generally, informing similar future applications. However, the complexity of the structures and unique nature of each site will limit application of the findings. These limitations are discussed in chapter 5.

Given this context, the research objectives of this project were as follows:

- Validate the ELJ design proposed for the Upper Hoh River Road project.
- Identify improvements to the design through both physical and numerical modeling.
- Develop design recommendations, including drag coefficients, applicable to the Upper Hoh River Road project and other similar projects.

WFLHD designed the ELJ units for the Upper Hoh River Road project using the resources currently available for design. However, these resources (described in chapter 2) are often anecdotal in nature and not easily adapted to situations different from those addressed in the

reference. Therefore, significant uncertainty exists. One objective of this study was to validate the WFLHD ELJ design to reduce some of this uncertainty.

This study implemented physical and numerical modeling experiments as described in chapter 3 and chapter 4, respectively, to validate the WFLHD ELJ design and identify improvements to it. Improvements evaluated included anchoring, spacing, configuration, and other ELJ design variables.

Finally, the results of this research are formulated as design recommendations. Where generalizations are possible, the limits of those generalizations are described.

## BACKGROUND ON THE UPPER HOH RIVER ROAD PROJECT

One of the major roads leading into Olympic National Park in Washington State is Upper Hoh River Road, located off US Highway 101 on the western side of Olympic National Park. The road is the only entryway into the Hoh Rain Forest and to the Park Rain Forest Visitor Center. Upper Hoh River Road is approximately 18-mi long and parallels the Hoh River as shown in figure 1.[1]

Road management to provide constant, safe access to residents, businesses, and park visitors has become increasingly difficult over the past 20 yr. Portions of the Upper Hoh River Road are located within and adjacent to the Hoh River channel migration zone. The location, combined with the growing frequency and severity of winter storm events (most recently in 2004, 2006, 2007, and 2009), has resulted in an increasing number of roadway washouts that either completely prevent access or create unsafe road conditions. In some cases, the damage has resulted in road closures, preventing access to the Hoh Rain Forest and the Hoh Rain Forest Visitor Center for weeks at a time (and for many months in 1996). Response to these storm events and efforts to maintain the road in its current location have resulted in a continuing outlay of limited maintenance funds to ensure safe access and mitigate any adverse effects that road preservation activities may have on threatened and endangered fish species.

In 1998, the Hoh Tribe requested that the U.S. Bureau of Reclamation (USBR) prepare a geomorphic study to better understand the existing and historical channel processes on the Hoh River and how human activities may have altered those processes. The study identified areas of risk for further lateral erosion in the historic channel migration zone and provided general management considerations to address these areas of concern (USBR 2004). The report also recommended collecting and analyzing more detailed data to develop a management approach to address such areas.

The Olympic National Park examined two methods to address roadway locations within the park that are vulnerable to damage from severe storm events: a site-specific approach and a natural systems engineering approach.[2] The report concluded that a natural systems engineering

[1]WFLHD. 2016. *Upper Hoh River Road Bank Stabilization: Hydraulics Report*. Unpublished internal draft report.

[2]National Park Service. 2009. *Olympic National Park Road Hazards and Solutions Report*. Unpublished internal report.

approach would likely provide a more long-term fix while improving ecological conditions. Six sites along the Upper Hoh River Road within the park were included in this evaluation.

In September 2013, WFLHD developed a comprehensive road management strategy to mitigate high-risk sites along the Upper Hoh River Road. The strategy prioritized sites for treatment, suggested a range of treatment options for each site, and presented initial cost estimates for each option.[3] A more recent study involved the selection and refinement of treatment options for two sites: mile post (MP) 3.7 to 4.1 (MP 4.0 site) and MP 7.7 to 7.9 (MP 7.8 site), shown in figure 1. An example of the bank degradation is shown in figure 2.

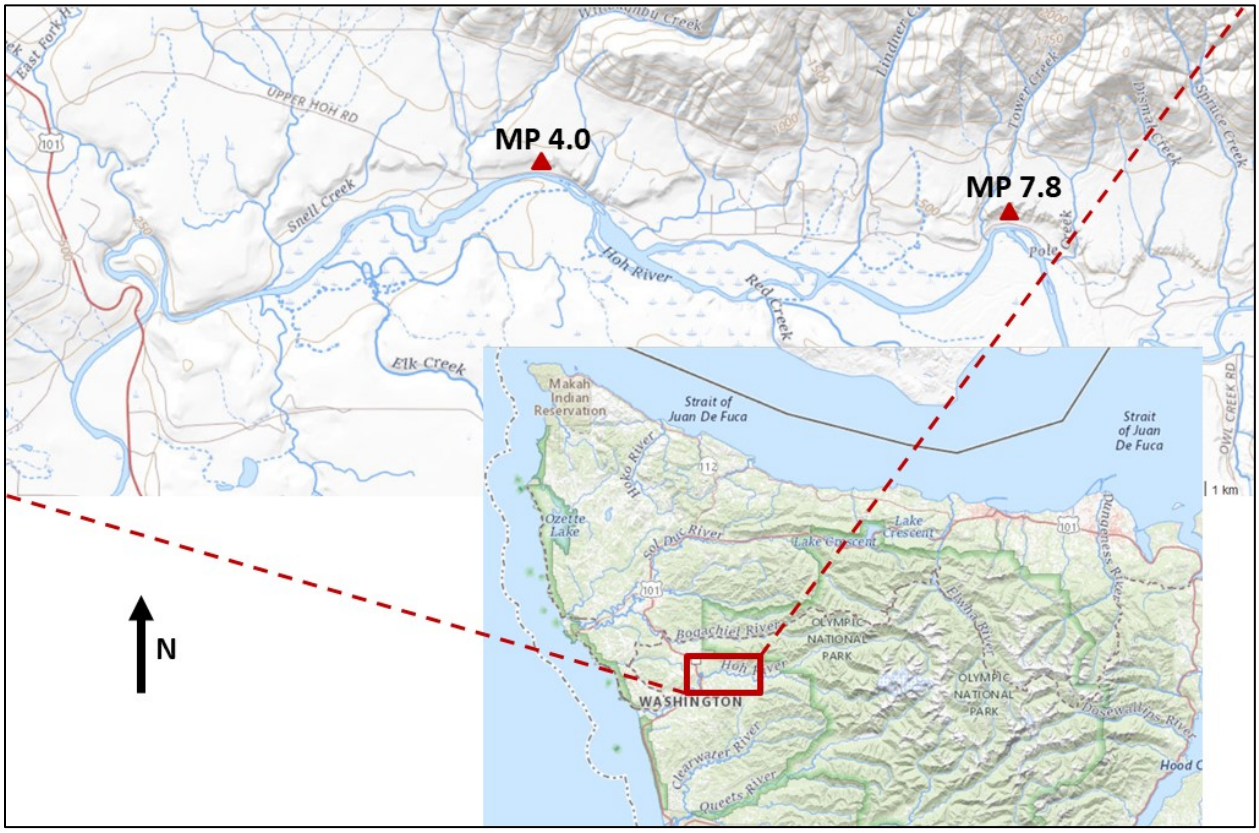


Source: USGS The National Map. Powered by Esri® with data from National Boundaries Dataset, 3DEP Elevation Program, Geographic Names Information System, National Hydrography Dataset, National Land Cover Database, National Structures Dataset, and National Transportation Dataset; USGS Global Ecosystems; U.S. Census Bureau TIGER/Line data; USFS Road Data; Natural Earth Data; U.S. Department of State Humanitarian Information Unit; and NOAA National Centers for Environmental Information, U.S. Coastal Relief Model. Data refreshed May 2020.

**Figure 1. Map. Upper Hoh River Road project location.**

[3]WFLHD. 2013. *Upper Hoh Road Bank Failure Risk Reduction Study*. Unpublished internal technical memorandum.

Source: FHWA.

**Figure 2. Photo. Hoh River and Upper Hoh River Road.**

Channel migration in the study section of the Hoh River has reached the valley limits to the north, as seen in figure 1, with both focus locations on the outside banks of meander bends. Down-valley translation of the river is controlled by large debris cones and fans. Bend locations are high-energy environments that have the potential for recruiting woody debris.

WFLHD's project planning and design team sought to create habitat complexity and a natural wood riparian buffer between the road and the river channel. They wanted to avoid the use of riprap as it did not offer the habitat benefits desired. The team considered an ELJ composed of wood and several concrete dolosse (sometimes referred to as "dolotimber") modeled after one applied at another site, shown in figure 3. This installation is finished by covering the dolotimber elements with a layer of coarse woody debris as shown in the photo. Based on the hydraulic analysis and cost estimates, the team recommended installation of a similar ELJ with dolosse ballast for both sites.

Figure 4 illustrates a detail of a single concrete dolos attached to timber logs with a chain, making a log–dolos bundle. In some applications, concrete dolosse are quite large to meet the desired level of stability, illustrated in figure 5. These units are sized and layered according to the site needs.

© 2017 Casey Kramer.

**Figure 3. Photo. ELJ on the Skagit River in Washington State.**

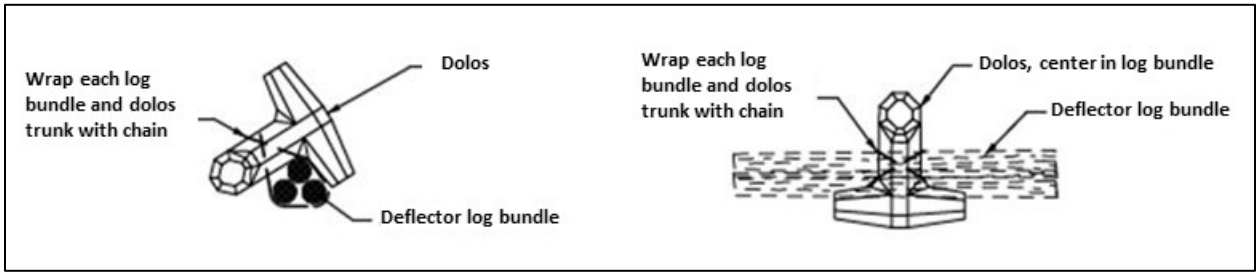


Source: FHWA.

**Figure 4. Drawing. Detail of log–dolos bundle.**



**Figure 5. Photo. Potential size of dolos.**

The reasons for using a log–dolos bundle for the ELJ treatment included the following:[4]

- It is the least expensive for effectively controlling bank erosion.
- It can accommodate a greater range of active flow channel migration and flow impingement angles.
- It minimizes channel bed excavation.
- It can be placed directly into flowing water, thereby minimizing disruption to environment.
- It does not appear to noticeably increase flooding or bank erosion on adjacent private property.
- It does not appear to negatively affect stream processes.
- It provides flow velocity reduction and habitat complexity.
- It is adaptable to changing field conditions.

The MP 4.0 site has 2,570 ft of proposed bank stabilization, while the MP 7.8 site has 500 ft of proposed bank stabilization, as shown in figure 6.[5] At MP 4.0, the bank stabilization consisted of two separate installations (C1 and C2). The MP 7.8 bank stabilization also had two installations

[4]WFLHD. 2016. Upper Hoh River Road Bank Stabilization: Hydraulics Report. Unpublished internal draft report.
[5]WFLHD. 2017. *Final Environmental Assessment: Upper Hoh River Road Project*. Unpublished internal report.

labeled as C4 Downstream and C4 Upstream. The project included additional culvert- and bridge-related work (labeled sites C3 and C5 in figure 6), but this is not discussed in this report.

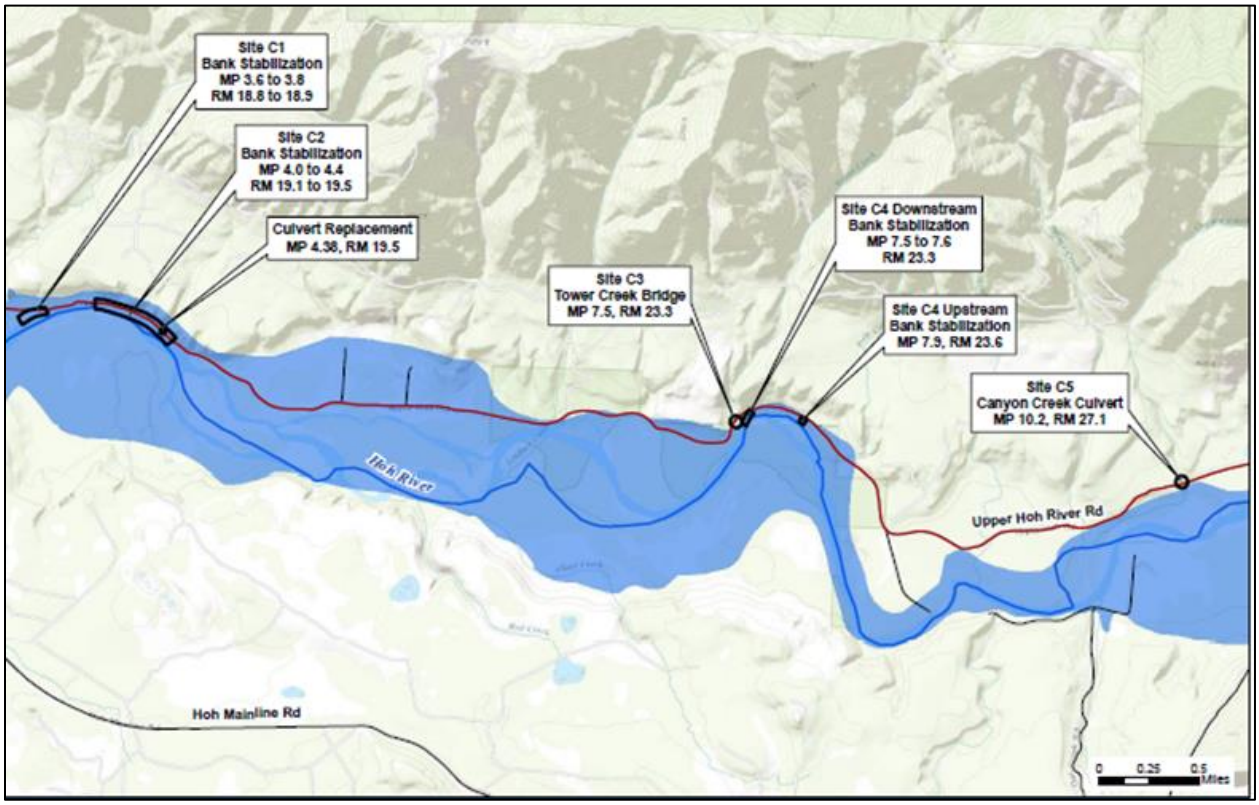


Source: FHWA.

**Figure 6. Graphic. Location of the river, road, and mitigation project components.**

## UNITS OF MEASURE

This research report uses customary (English) units. However, in limited situations, both customary units and SI (metric) units are used or only SI units are used because these are the predominant measures used nationwide and globally for such topics. In these situations, the report provides the rationale for the use of SI units. Information on units and unit conversions is provided in the SI Conversion Factors table in the front matter.

# CHAPTER 2. LITERATURE REVIEW

FHWA researchers conducted a literature review to identify applications of wood for stream stabilization, stability analyses conducted on ELJs, and physical and numerical ELJ modeling to inform the design of this study. Each of these areas is discussed in the following sections.

## USE OF WOOD FOR STREAM STABILIZATION

Widespread use of rock riprap as a tool for stream stabilization has led to a growing understanding of the limits of this approach in creating habitat and the importance of natural wood materials in stream and river ecosystems. Wood in the riverine environment can control river gradient and store sediment (Abbe et al. 2003a). Natural logjams can form stable "hard points" within the channel migration zone that can limit bank erosion. Channel migration at these hard points is retarded, and the radius of curvature of river bends is reduced, forming tighter meanders over time (Abbe et al. 2003a). Bennett et al. (2015) stated that ELJs can function effectively as bank protection because they reduce the energy in near-bank regions, which may facilitate bank stability, sediment deposition, and nutrient sequestration. However, they also observe that ELJs can create scour holes around the perimeter of the structure where accelerated flow, elevated turbulence intensities, and higher bed shear stresses occur.

Natural meander jams are also a principal cause of channel avulsions in Pacific Northwest rivers (Abbe et al. 2003b). Depending on the location of these avulsions, they may be considered undesirable for adjacent property owners or users of existing infrastructure.

Configurations of engineered wood structures vary greatly. Based on examples from nature, several types of engineered structures using wood have been applied in the field. For bank protection, these include continuous natural log revetments (e.g., bankfull bench jams, flow-deflection jams, and log cribs) and interspersed structures (e.g., meander jams, flow-deflection jams, and crib groins) (Abbe et al. 2003a). For grade control applications, engineered jam types include log steps (trees that span the channel with each end being held in place by boulders, bedrock, wood, or sediment) and valley jams (stable full-spanning jams). For flow manipulation, engineered jams may include flow-deflection (partially spanning jams that deflect flow nearly perpendicular to the channel axis), bankfull bench (partially spanning jams that form along the margins of headwater channels), bar-apex (midchannel), and meander jams (form on the outside bank at the downstream end of meander bends) (Abbe et al. 2003b).

For interspersed bank stabilization or protective structures, the gaps (spacing) between ELJs are an important design consideration. The specific spacing of ELJ structures can be based on experimental studies of flow deflection by rock groins and pile dikes (Abbe et al. 2003a). Bennett et al. (2015) performed fixed-bed physical model tests on both single and multiple ELJs to evaluate the hydraulic effects of alternative configurations. Others provide specific structure spacing recommendations in generalized form (USBR and U.S. Army Engineer Research and Development Center [ERDC] 2016).

Other variations in the design and application of ELJs are in the uses of piles, ballast, and other restraint systems. Wood and steel piles are increasingly being used to stabilize ELJs (Abbe et al. 2018). Cabling and chains have also been used to secure individual wood pieces to each other or

to ballast to create larger, more stable ELJ elements. Some have noted that, when cable is used in wood structures, rather than using it for anchoring, cable should only be used to secure logs tightly either to one another or directly to rock ballast so that all the components act as one unified structure (Abbe et al. 2003a). Ballast may be included in ELJs in the form of sand and gravel, rock, or concrete structures. A heavy, jack-like structure made of unreinforced concrete—called a "dolos"—is used in some applications as ballast (Papanicolaou et al. 2018). Dolosse may weigh more than 8 tons each and have arms that extend up to 8 ft.

The literature contains many descriptive examples of ELJ uses, including observations on their performance for limited flood events that occurred following installation. Abbe et al. (2003b) discussed four Washington State demonstration projects where the emphases were on bank stabilization and habitat creation. Abbe et al. (2018) described the use of a pile-stabilized ELJ for bank stabilization on the Hoh River to protect US Highway 101. Locations of other ELJ installations include the Lower Cle Elum River, to recruit more natural wood downstream of Cle Elum Dam (Kittitas Conservations Trust 2015); the South Fork Nooksack, to aid Chinook salmon spawning habitat restoration (Washington State Recreation and Conservation Office [WSRCO] 2009); the Deschutes River, to restore aquatic habitat complexity lost by historic modification (WSRCO 2012); the Lower Elwha River, to restore critical salmon habitat (WSRCO 2000); and the Cowlitz River, to stop bank retreat (Hall and Moler 2006). Gallisdorfer et al. (2014) also describe an ELJ application on the Big Sioux River in South Dakota to mitigate excessive bank erosion.

## DRAG FORCES ACTING ON ELJS

Much of the literature provides general discussion of the forces acting on ELJs, such as drag and buoyancy, but does not provide quantitative engineering guidelines for the design of ELJs. (See Abbe et al. 2003a for an example.) The literature also states generalized engineering goals, such as that key members in a logjam should not move during bankfull flow (Abbe et al. 2003b).

Other literature attempts to provide quantitative drag coefficients for ELJs. Gallisdorfer et al. (2014) and Bennett et al. (2015) used physical scale modeling of ELJs to estimate drag coefficients, including varying the definition of the "characteristic velocity" to compute the drag coefficients. Bennett et al. (2015) concluded that, based on the measurements obtained in their model studies and in light of previous work, drag coefficient values for ELJs of the type tested should be in the range of 1 to 3 when using the spatially averaged flow velocity of the channel as the characteristic velocity. However, the caution with these estimates and most others is that they depend on the specific ELJ configuration and placement used. For the conditions tested, Bennett et al. (2015) also noted that reduced near-bank flow velocities can extend downstream to distances more than 30 times the height of the ELJ.

Shields and Alonso (2012) used cylinders, branched logs, and logs with rootwads in near-prototype scale-model experiments in a grassed, trapezoidal channel. They compared results of drag coefficients computed from their study with those from others. They also distinguished between drag coefficients with and without blockage and considered "wave" drag when the object was near the water's surface. Wave drag increases the drag force on the ELJs. The primary purpose of this study was to support the design of restraint systems for ELJs to avoid the failures of many ELJ installations. The authors also discussed concepts for addressing

uncertainty in estimating drag-force loading, including the use of safety factors and Monte Carlo analyses. USBR and ERDC (2016) discussed safety factors generally in the range of 1.5 to 2.0.

Xu and Liu (2017) used computational fluid dynamics (CFD) to conduct numerical modeling of the physical modeling conditions in Gallisdorfer et al. (2014), evaluating the utility of using CFD for estimating drag coefficients. They found that mean velocity of the whole channel was less representative than the local mean value experienced by an ELJ when computing the drag coefficient. They suggested that the replacement of incoming flow velocity with the local mean is reasonable and necessary because of the effect the side wall has on velocity distribution in physical modeling.

In addition to the fluid forces acting on ELJs, the researchers found limited discussion of geotechnical considerations for the design and placement of ELJs. The USBR and ERDC (2016) lightly cover geotechnical analysis, including use of the Bank Stability and Toe Erosion Model.

A characteristic of many ELJs is that, rather than being solid, they have a porosity that allows flow through the ELJ. This porosity, in turn, alters the drag characteristics of the structure. In the physical modeling of Gallisdorfer et al. (2014), Bennett et al. (2015), Shields and Alonso (2012), and Papanicolaou et al. (2018), researchers attempted to duplicate the porosity of the respective prototype ELJs in their models. They then accounted for the porosity by using the area blocked by the ELJ rather than the total ELJ dimensions to compute drag coefficients.

Xu and Liu (2017) investigated alternatives for representing porosity in three-dimensional (3D) numerical modeling by considering three different modeling cases: a fully resolved case, a porosity model case, and a solid barrier case. These cases ranged from the most complicated to model to the simplest. The alternatives informed the appropriate representation of ELJs and the level of effort needed to represent key phenomenon associated with ELJs. The fully resolved case describes the ELJ in detail by representing each component (logs, etc.) of the ELJ individually. The porosity model is an approach where the outer dimensions of the ELJ are specified and, by assigning a permeability value to the interior, water flow through the structure can be modeled. The third option represents the outer dimensions with the interior being impermeable. Papanicolaou et al. (2018) performed limited 3D numerical modeling representing the ELJ as a solid barrier.

## ELJS AND SCOUR

Erosion and scour may undermine an ELJ, ultimately contributing to its failure. The physical modeling of Gallisdorfer et al. (2014) included mobile bed testing to understand erosion and deposition patterns near and downstream from an ELJ. They observed that the influence of the ELJ extended downstream. Focusing on gravel-bed rivers, Papanicolaou et al. (2018) considered the influences of both ELJ porosity and bed sediment nonuniformity to develop enhanced formulas to predict scour for both clear-water and live-bed conditions. The study evaluated porosity by comparing the results of ELJs with a porosity of approximately 70 percent to gravel barb structures with a lower porosity between 30 and 40 percent. They analyzed four scour equations and proposed adjustments that incorporated both porosity and sediment nonuniformity to improve estimates of scour for the tested cases.

USBR and ERDC (2016) discussed the use of existing pier and abutment scour equations for bar-apex and bank-protection ELJs, respectively. Since the scour associated with such equations assumes a solid pier or solid abutment, the scour estimate is expected to be conservative because the porosity of many ELJs allows flow through the structure rather than around it. In addition, USBR and ERDC (2016) also cited scour estimation examples.

## PHYSICAL AND NUMERICAL MODELING OF ELJS

The variety of ELJ types and configurations creates a challenge for development of generalized procedures for estimating site-specific loads and scour. There is also no broad concurrence regarding the design events that the ELJ should survive. Therefore, physical and numerical modeling has been an important tool for evaluating specific ELJ designs and installations.

Gallisdorfer et al. (2014) provided an overview of the appropriate methods for physical model scaling for both fixed and mobile bed testing. Bennett et al. (2015) provided an expanded discussion on these tests. Shields and Alonso (2012) performed several near-prototype, scale-model tests in a grass-lined trapezoidal channel.

Both two dimensional (2D) and 3D numerical modeling have been applied to the design and evaluation of ELJs. Abbe et al. (2018) described the use of 2D hydraulic modeling of an ELJ project to determine the overall effects on flow depths and velocities near and downstream of the ELJs. In this case, the ELJs were represented as solid objects.

Xu and Liu (2017) modeled the experiments of Gallisdorfer et al. (2014) using CFD to expand the types and configurations of ELJs that could be cost-effectively represented in modeling experiments. Papanicolaou et al. (2018) also performed limited CFD testing of a bar-apex ELJ.

# CHAPTER 3. PHYSICAL MODELING

Researchers performed three phases of physical scale modeling of ELJs as a channel-bank-stabilization strategy at the J. Sterling Jones Hydraulics Research Laboratory, part of TFHRC. Phase I focused on erodible bed flume experiments using fine sediment to study the effectiveness of ELJs in deflecting impinging flow away from an unstable eroding bank into the main channel and the effects and characteristics of scour formation around ELJ installations. Phase II used a combined physical and CFD modeling approach to determine a drag coefficient for an ELJ structure. Finally, phase III included experiments on coarse bed and bank material to analyze the stability of ELJs under hydrodynamic loads and scour.

## EXPERIMENTAL EQUIPMENT

The multifunctional flume system (MFS) shown in figure 7 features a 90-ft-long by 13-ft-wide tiltable working platform for experimental setups. Channel modules of 3- or 6-ft wide can be mounted on the working deck. Both channel section alternatives include a 30-ft-long sediment recess test section.

The water circulation system shown in figure 8 includes a 30-ft flow inlet fiberglass headworks consisting of a distribution plenum followed by a flume inlet contraction zone. Water level measuring stations with ultrasound measuring devices are installed along the flume length. A computer-operated louver gate regulates the flow depth at the outlet. Water is supplied to the flume by a circulation system with a ground sump of 7,400 $ft^3$ and a pump with a maximum discharge capacity of 30 $ft^3/s$. The discharge is measured by a magnetic inductive flowmeter installed before the flow is introduced to the flume system.

The sediment recirculating system shown in figure 9, which is the only one of its kind in the United States, consists of a 7-ft-deep sediment trap located at the flume outlet, a 21.5-ft-long inclined auger, conveyor belt, and sediment infeed hopper. Two diaphragm pumps push sediment from the infeed hopper back into the flume through plastic nozzles located at the bottom of a specially designed channel module. This sediment recirculation capability allows for a much more realistic simulation of natural bed load material (sand) in river models. Thus, the effects of hydraulic structures on the flow, water levels, bed forms, bed load, and scour in rivers can be simulated and analyzed.

For this experiment, the MFS was configured with a 3-ft-wide channel and test section, including a 3-ft-wide by 30-ft-long by 1.3-ft-deep sediment recess section, shown in figure 10. Stations to measure water level with ultrasound measuring devices were installed along the test section length. A fully automated, three-axis measurement carriage was equipped with state-of-the-art sensors to measure changing model geometries, water surface profiles, 3D velocity data, and bathymetric and scour data.

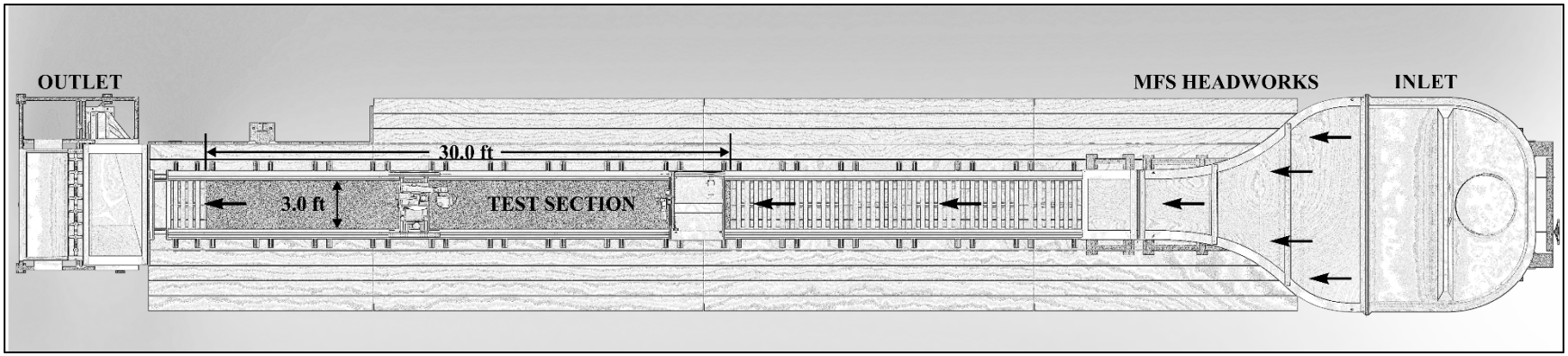


Source: FHWA.

**Figure 7. Schematic. MFS plan view.**

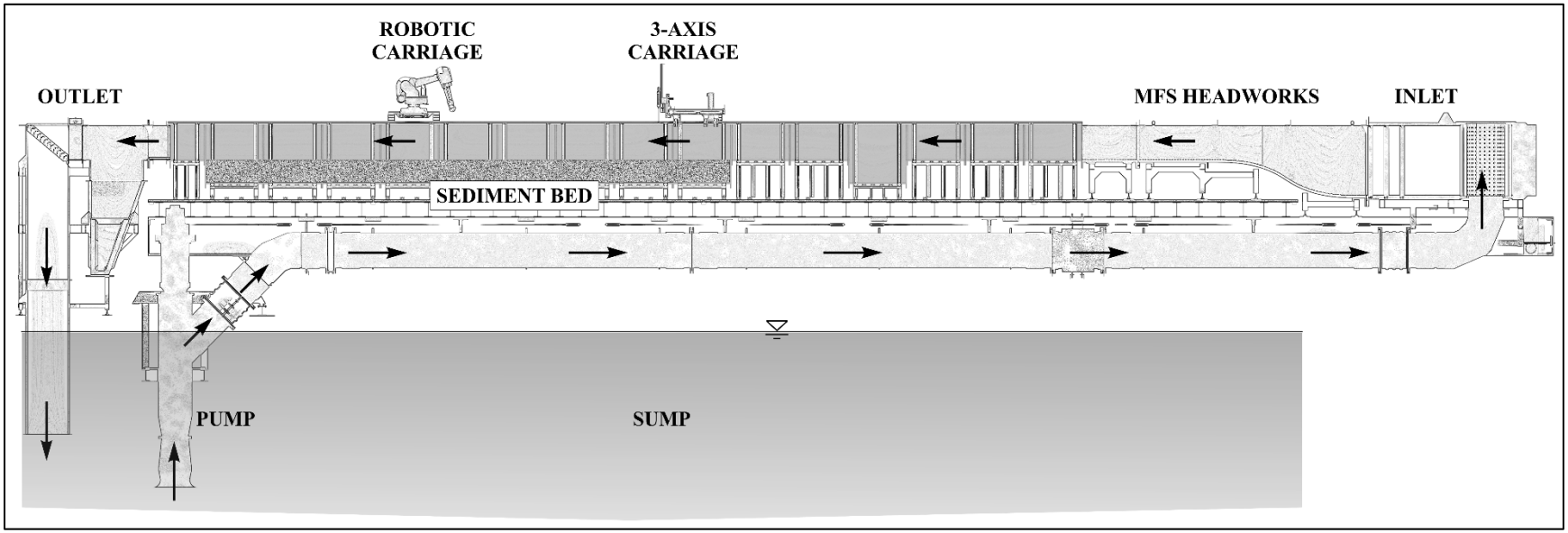


Source: FHWA.

**Figure 8. Schematic. Side view of water recirculating system in the MFS.**

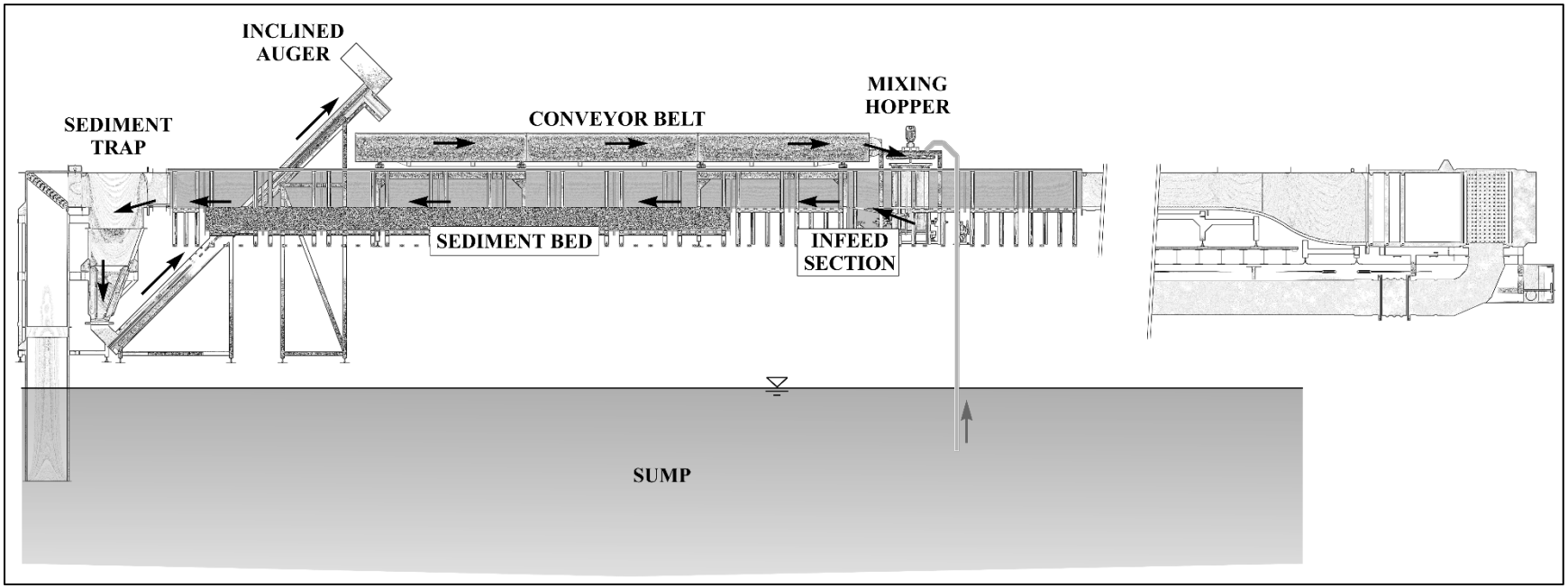


Source: FHWA.

**Figure 9. Schematic. Side view of sediment recirculating system in the MFS.**

Source: FHWA.

**Figure 10. Photo. MFS channel test section.**

In addition, the test section was equipped with an automated carriage supporting a six-axis robotic arm. The robotic arm assisted with time-consuming tasks related to experiment setup including leveling the sand bed, as seen in figure 11, and shaping erodible compound channel geometries.

The lab researchers employed several commercially available measuring devices in the study, including an automated laser scanning system (figure 12) and a velocity profiler probe (figure 13). Other special devices and software solutions developed in the J. Sterling Jones Hydraulic Research Laboratory were also used.

Source: FHWA.

**Figure 11. Photo. Robotic arm leveling the channel bed.**

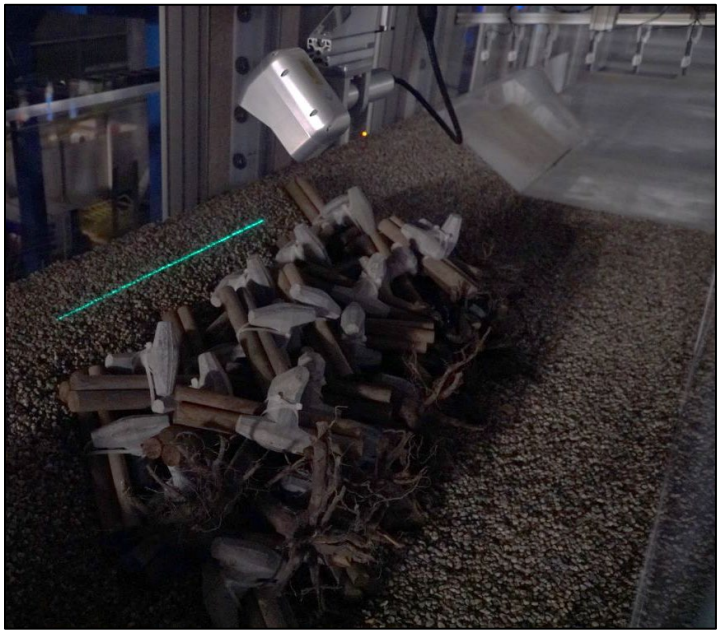

Source: FHWA.

**Figure 12. Photo. Automated laser scanning system.**

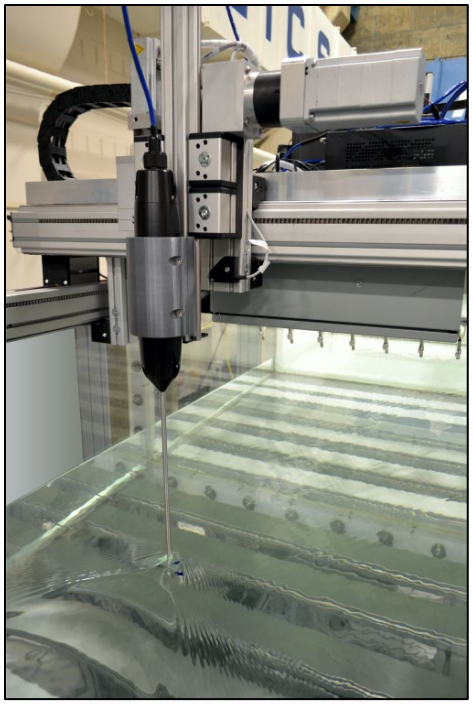

Source: FHWA.

**Figure 13. Photo. Velocity profiler probe.**

## ELJ PHYSICAL MODEL DESIGN AND SCALING RATIOS

Physical ELJ scale models were designed and fabricated to assess ELJ structure stability and effectiveness in reducing high-velocity flows and shear stresses along the erodible bank area upstream and between each ELJ, to quantify the morphodynamic impact on the channel bank and bed, and to measure hydrodynamic forces acting on the ELJ. To achieve these purposes, the model scaling had to be appropriate to capture the important variables to allow application of results to the prototype's scale. Scale models for riverine applications should capture geometric, kinematic, and dynamic similitude within the prototype systems (Julien 2002). Geometric similitude is achieved when the geometric dimensions (e.g., length) of the model are consistently scaled. Kinematic similitude applies to velocity and discharge. Both geometric and kinematic similitude between a prototype and model are generally achieved through scaling on the Froude number (*Fr*), as seen in equation 1 (Gallisdorfer et al. 2014):

$$Fr_r = \frac{Fr_p}{Fr_m} = \frac{v_r}{\sqrt{g_r L_r}} = \frac{v_r}{\sqrt{L_r}} = 1 \quad (1)$$

Where:

$Fr_r$ = Froude number ratio.
$Fr_p$ = Froude number for the prototype.
$Fr_m$ = Froude number for the model.
$v_r$ = velocity ratio.
$g_r$ = gravitational acceleration ratio.
$L_r$ = length ratio.

For this investigation, the lab researchers selected a $L_r$ of 25; that is, $L_m$:$L_p$ is equal to 1:25. Table 1 summarizes the model scaling ratios based on Froude number similarity.

**Table 1. Summary of model scaling ratios based on Froude number similarity.**

| Scaling Parameter | Ratio |
|---|---|
| $L_r = L_p / L_m$ | 25 |
| $V_r = V_P / V_M = (L_r)^{0.5}$ | 5 |
| $Q_r = Q_p / Q_m = (L_r)^{2.5}$ | 3,125 |

Dynamic similitude applies to forces acting on the model and the bed materials. Examples of forces of interest in this study include drag and buoyancy forces acting on the ELJs and tractive forces acting on bed materials. Gallisdorfer et al. (2014) analyzed model similitude for a study of drag on and geomorphological responses to ELJs like the current study. They determined the dimensionless parameters in the relationship shown in equation 2 were important:

$$f\left[C_D, Fr, \left(\frac{k_{elj}}{L}, \beta, \eta\right)\right] = 0 \quad (2)$$

Where:

$C_D$ = drag coefficient.
$k_{elj}$ = surface roughness of the ELJ.
$L$ = characteristic length scale.
$\beta$ = a measure of orientation of the ELJ with respect to flow direction.
$\eta$ = porosity of the ELJ.

Based on this equation, $C_D$ will be the same in the prototype and the model if the other variables are the same in both the prototype and model. As previously described, Froude number similarity is the primary basis of the model scaling. Therefore, if $\beta$ and $\eta$ are similar in the prototype and model, $C_D$ from the model tests is applicable to the prototype. From Gallisdorfer et al. (2004), as shown in equation 3, drag-force ratio $(F_D)_r$ is calculated as follows:

$$(F_D)_r = (C_D)_r \rho_r A_r v_r^2 = (C_D)_r \rho_r {L_r}^3 \quad (3)$$

Where:

$A_r$ = area ratio.
$(C_D)_r$ = drag coefficient ratio.
$\rho_r$ = density of water ratio.

As discussed previously, $(C_D)_r$ is equal to 1, and because water is used in both the prototype and model, $\rho_r$ also equals 1, reducing $(F_D)_r$ to the cube of $L_r$.

Consideration of scour and erosion introduces further complexity to model scaling. Einstein and Chien (1954) noted the requirement for the scale ratios for both the dimensionless shear stress and particle Reynolds number to equal 1. The calculation to determine dimensionless shear stress ratio ($\theta_r$), shown in equation 4, is as follows:

$$\theta_r = \frac{\gamma_r R_r S_r}{\gamma_r (SG-1)_r D_r} = \frac{R_r S_r}{(SG-1)_r D_r} = 1 \quad (4)$$

Where:

$R_r$ = hydraulic radius ratio.
$S_r$ = slope ratio.
$\gamma_r$ = unit weight of water ratio.
$D_r$ = particle diameter ratio.
$(SG-1)_r$ = specific gravity minus 1 ratio.

For an undistorted geometric model, $S_r$ =1 and $R_r = D_r$, which simplifies the equation. The dimensionless particle (grain) Reynold's number ($(Re_g)_r$), shown in equation 5, is calculated as follows:

$$\left(Re_g\right)_r = \frac{R_r S_r D_r^2}{\nu_r^2} = 1 \quad (5)$$

In equation 5, $N_r$ is the kinematic viscosity ratio.

Again, for an undistorted geometric model, $S_r = 1$ and $R_r = D_r = L_r$, simplifying the equation. Selecting an appropriate specific gravity and kinematic viscosity for the model such that both $\theta_r$ (equation 4) and $(Re_g)_r$ (equation 5) equal 1 is not possible when using quartz-density sand and fresh water (Julien 2002). Therefore, conditions for modeling a movable bed will be based on identifying threshold movement conditions for both the prototype and model. Because this approach does not represent true scaling, the model results will not simulate the exact scour dimensions and timing but can be used as an indicator of threshold conditions (Gallisdorfer 2014).

**Channel Geometry and Discharge Conditions**

Prototype conditions for geometry and discharge were represented in the model by scaling depth and velocity. Prototype conditions were based on the estimated 50-yr design discharge of 58,000 $ft^3/s$ in the Hoh River at the locations of interest. Prototype width and discharge were not represented explicitly in the model because the active channel at the sites of interest ranged from 250- to more than 400-ft wide; therefore, the model representation in the horizontal direction was distorted from the prototype.

Figure 14 illustrates the model representation of the Hoh River as half of a trapezoid, with one of the flume walls representing the center of the river (or at least a portion of the river sufficiently far from the bank and ELJs that their performance is unaffected). The model channel ($B$) is placed within the 3-ft wide and 30-ft long test section of the flume. The width of the bed ($W_{BED}$) is 1.83 ft. The bank slope is approximated as 1 vertical (V):1.5 horizontal (H) (33.7 degrees) with a bank height ($H_{BANK}$) of 0.69 ft. The figure also displays characteristic model velocity ($V_M$), upstream velocity ($V_U$), and characteristic flow depth ($y_0$). Phases I and III of the experiments were conducted on erodible bed and bank materials. Phase II experiments were conducted on a bed and bank constructed of clear acrylic sheeting.

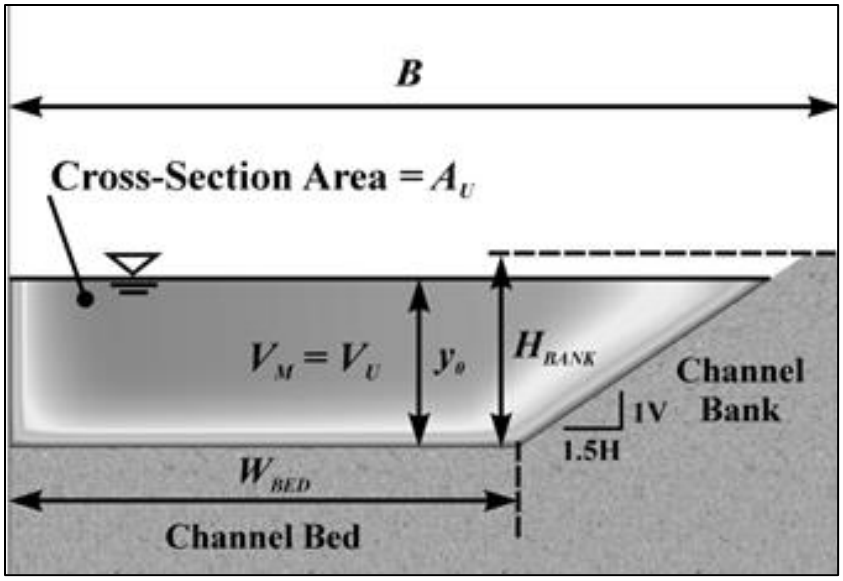


Source: FHWA.

**Figure 14. Sketch. Channel cross section represented in the flume.**

Table 2 summarizes the selected values for the prototype and model. The $V_0$ and $y_0$ for the prototype were based on the estimated 50-yr discharge in the Hoh River at the project sites. In the prototype, the presence of ELJs on the banks made a negligible difference in water velocity and depth. However, with the physical scale model in the flume being much narrower than the length-scaling ratio would suggest, defining $V_M$ was not straightforward because $V_U$ differed from the velocity in the channel adjacent to the ELJs ($V_{ADJ}$), which is not the case in the prototype. Therefore, the experiments were defined to use both $V_U$ and $V_{ADJ}$ as characteristic velocities to evaluate which may be more appropriate in a design method. In figure 14, the characteristic parameters—$V_U$, $A_U$, and $y_0$—are defined based on the cross section of the upstream approach. In figure 15, characteristic parameters—$V_{ADJ}$, cross-sectional area ($A_{ADJ}$), and $y_0$—are defined using the area adjacent to the ELJs.

**Table 2. Prototype and model depth and velocity.**

| Parameter | Prototype | Model | Ratio |
|---|---|---|---|
| Depth, $y_0$ (ft) | 15 | 0.6 | 25 |
| Velocity, $V_0$ (ft/s) | 12.1 | 2.4 | 5 |
| Froude number, *Fr* | 0.55 | 0.55 | 1 |

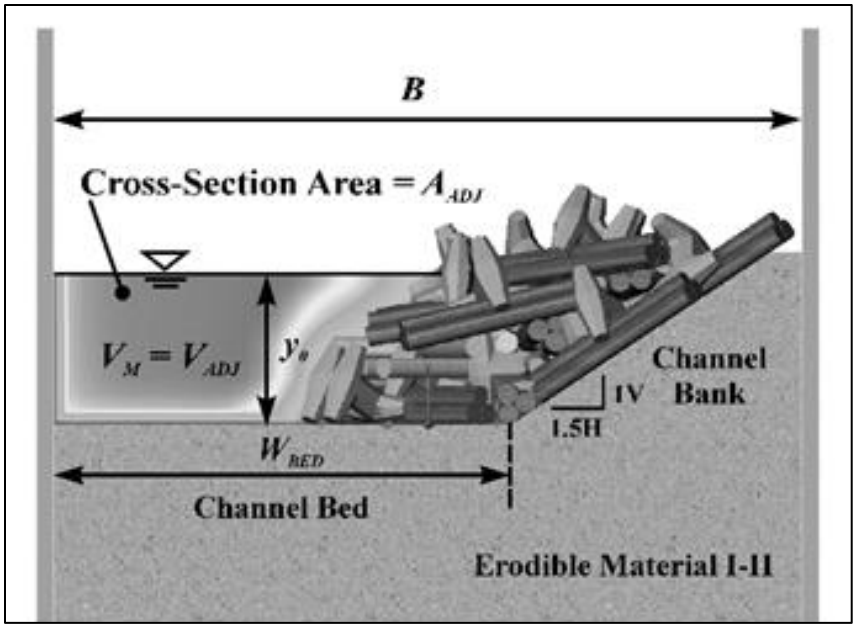


Source: FHWA.

**Figure 15. Sketch. Channel cross section showing adjacent velocity and area.**

### Channel Bank and Bed Material

The design and implementation of the channel model also accounted for the interaction of the ELJ models with a movable channel. Since the hydraulic boundary conditions (water depths, flow velocities, channel bed slope, etc.) are specified by the Froude law, the similarity of incipient motion of bed-load transport was achieved by choosing suitable bed materials that reproduced conditions similar to the Hoh River during a 50-yr discharge.

Nine bed and bank gradation samples were taken from the Hoh River (sites C1 and C2) and analyzed for their gradation distribution, as summarized in figure 16. From these distributions, four critical velocities were computed using Laursen's equation to determine whether the prototype conditions are live-bed or clear-water and are summarized in table 3. Given the prototype velocity of 12.1 ft/s shown in table 2, sample set one is live-bed, while the other three are clear-water conditions.

Two different bed materials were used in the flume model as shown in figure 17. Material I was uniform fine sand with a median grain size of $D_{50}$ = 0.014 inches. Material I was used in the phase I experiments to provide an overall understanding of the erosion characteristics around the ELJs. These experiments were conducted using clear-water conditions near the threshold with live-bed conditions. At $y_0$ = 0.6 ft in the flume, material I had a critical velocity of 1.08 ft/s.

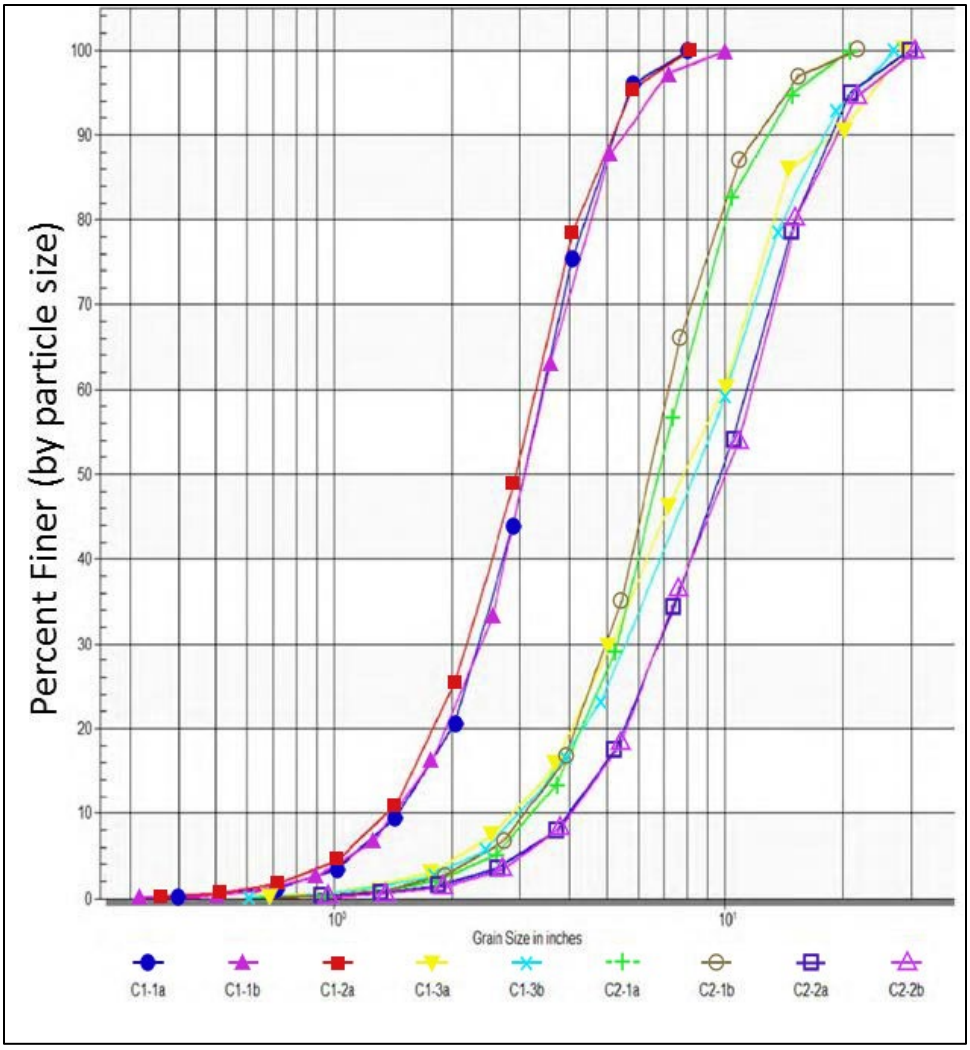


Source: FHWA.

**Figure 16. Graph. Hoh River gradation analyses.**

Material II was used in the phase III experiments and was selected for its similarity to the prototype so that it represented clear-water conditions near the threshold of live-bed conditions. For the model velocity of 2.4 ft/s, as shown in table 2, a uniform coarse sediment with a grain size median diameter of $D_{50}$ = 0.18 inches was selected. This material had a critical velocity of 2.53 ft/s when $y_0$ = 0.6 ft.

**Table 3. Prototype sediment transport conditions.**

| Sample Set | Number of Gradations | $D_{50}$ (Inches) | Laursen's Critical Velocity (ft/s) | Scour Condition |
|---|---|---|---|---|
| 1 | 3 | 3.0 | 11.1 | Live-bed |
| 2 | 2 | 6.5 | 14.4 | Clear-water |
| 3 | 2 | 8.0 | 15.4 | Clear-water |
| 4 | 2 | 10.0 | 16.6 | Clear-water |

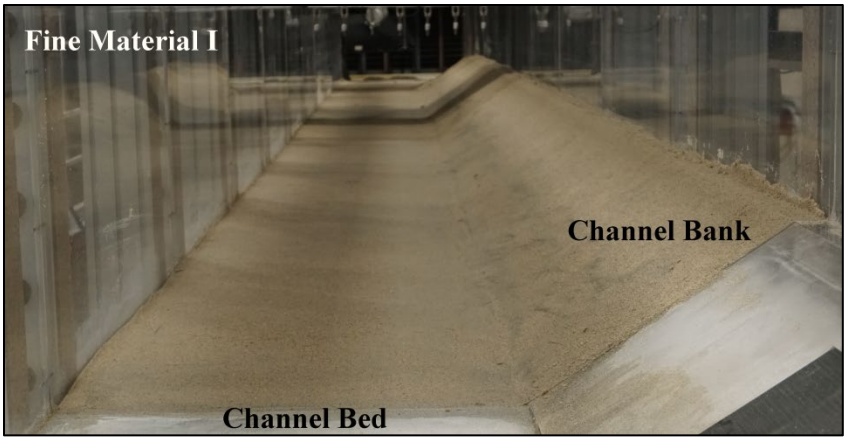

Source: FHWA.

A. Fine material I.

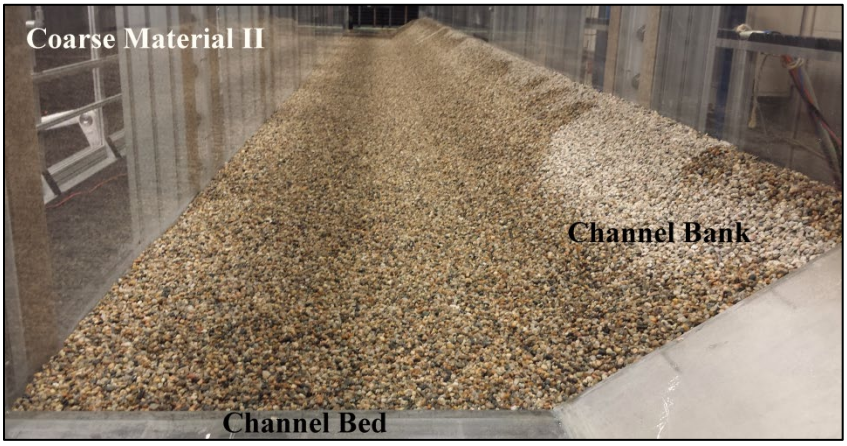

Source: FHWA.

B. Coarse material II.

**Figure 17. Photos. Erodible channel model.**

### Log–Dolos Bundles

The ELJ design created by WFLHD is composed of numerous log–dolos bundles with rootwad logs interspersed. The main goal for the fabrication of model log–dolos bundles, as depicted in figure 18, was to achieve similar material densities to those for the prototype application. As figure 18 illustrates, the log–dolos bundle was made from a single concrete dolos and three wooden dowels representing tree trunks.

A prototype dolos was made of precast concrete with a geometry like jacks. The cylindrically shaped tips of the dolos were designed to emulate natural wood debris found in rivers. The dolos provided ballast for the logs when they were chained together. Figure 19 details the dimensions of the 1:25 scale model log–dolos bundle.

Source: FHWA.

**Figure 18. Photo. Fabricated log–dolos bundle (model scale 1:25).**

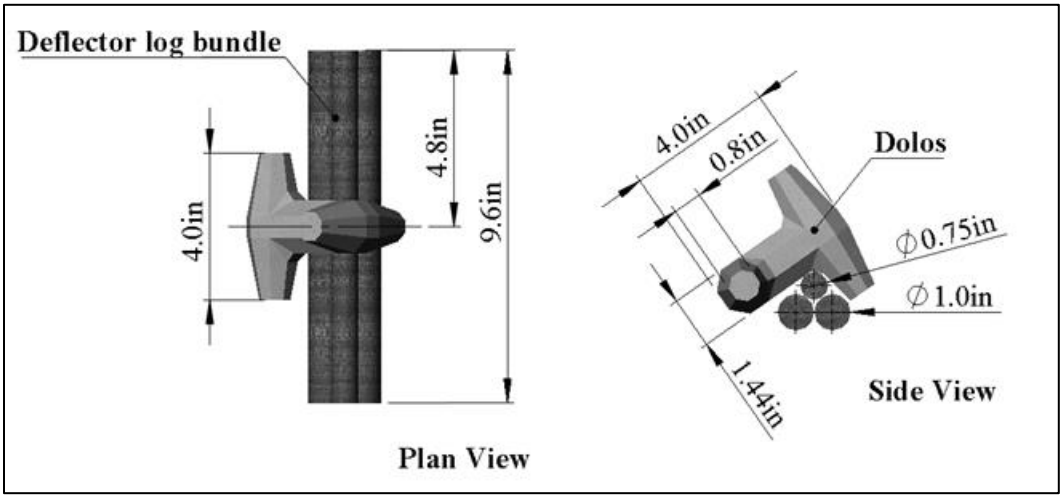


Source: FHWA.

**Figure 19. Drawing. Fabricated log–dolos bundle dimensions (model scale 1:25).**

The geometry and weight of the prototype log–dolos bundle provided by WFLHD are summarized in table 4. The prototype unit weights were 30 lb/ft$^3$ for the logs and 150 lb/ft$^3$ for the concrete dolos. To properly model stability, similar densities were targeted for the wood and dolos based on the 1:25 scale length. In the ideal case, the unit weights of the prototype and model would be the same, and the prototype-to-model ratio for weight would be identical to the ratio for volume. As seen in table 4, the unit weights for the prototype and model dolos differ by less than 10 percent, while the unit weights for the prototype and model wood differ by less than 14 percent.

**Table 4. Prototype and model log–dolos bundle characteristics.**

| Parameter | Prototype | Model | Ratio |
|---|---|---|---|
| Dolos length (inches) | 100 | 4 | 25 |
| Dolos volume (inches$^3$) | 182,030 | 11.65 | 15,625 |
| Dolos weight (lb) | 15,801 | 0.9215 | 17,150 |
| Dolos unit weight (lb/ft$^3$) | 150 | 137 | 1.09 |
| Small log diameter (inches) | 18.75 | 0.75 | 25 |
| Small log length (inches) | 240 | 9.6 | 25 |
| Small log volume (inches$^3$) | 66,270 | 4.24 | 15,625 |
| Small log weight (lb) | 1,150 | 0.0838 | 13,720 |
| Small log unit weight (lb/ft$^3$) | 30 | 34 | 0.88 |
| Large log diameter (inches) | 25 | 1.0 | 25 |
| Large log length (inches) | 240 | 9.6 | 25 |
| Large log volume (inches$^3$) | 117,820 | 7.54 | 15,625 |
| Large log weight (lb) | 2,045 | 0.1543 | 13,250 |
| Large log unit weight (lb/ft$^3$) | 30 | 35 | 0.86 |

**ELJ Model**

The ELJ layout was patterned after the design by WFLHD (appendix A). Each ELJ unit was composed of collections of log–dolos bundles, rootwads, and individual (unbundled) key dolosse that were placed on the streambed. Figure 20 and figure 21 provide the plan and cross-sectional views, respectively, of a single ELJ unit, including all relevant geometry parameters for construction and installation in series along the channel bank. The unit was constructed with successive layers of the components. The first (bottom) layer, referred to as layer A, was placed on the unexcavated channel bed. Following the plans in appendix A, this layer had a defined layout. Layer B, and other layers if needed, was placed on top of layer A in a random manner to achieve the design height ($H_{elj}$) throughout the unit. The prototype and model dimensions are summarized in table 5.

Each ELJ unit was created according to the WFLHD design (appendix A), with 25 log–dolos bundles, 14 rootwads, and 7 key dolosse. Layer A included 10 log–dolos bundles, 7 rootwads, and the 7 key dolosse. Although sensitive to the details for the log–dolos bundles and rootwads, characteristics of an ELJ unit included log–dolos and rootwad density, which equaled 0.00076 log–dolos bundles/ft$^3$ and 0.00042 rootwads/ft$^3$. On a mass basis, the dolosse and wood combined for a density of 72.3 and 70.9 lb/ft$^3$ within the ELJ unit for the prototype and model, respectively. For both the prototype and model, the void ratio of the ELJ unit was 0.77. With this configuration, the submerged density of the ELJ unit was 64.6 and 64.3 lb/ft$^3$ for the prototype and model, respectively. Both the density and void ratio estimates excluded the key dolosse because they did not interlock with the remaining components. These density values may be useful to compare alternative packing designs for ELJs.

As described previously, similarity between the prototype and model also depends on $\beta$ and $\eta$ of the ELJ units. The orientation of both prototype and model were the same, with the unit installed parallel to the bank. The porosity of the prototype and model were assumed to be equivalent because the unit design and composition were the same.

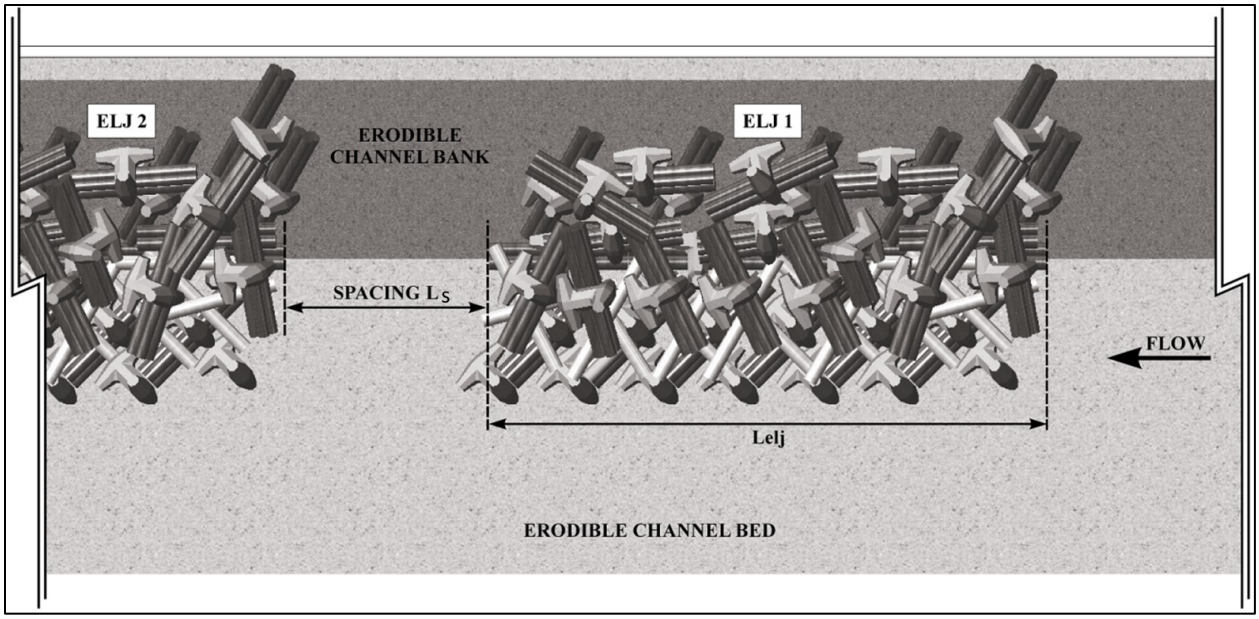


Source: FHWA.

**Figure 20. Drawing. Plan view of the model ELJs installed in the MFS test section.**

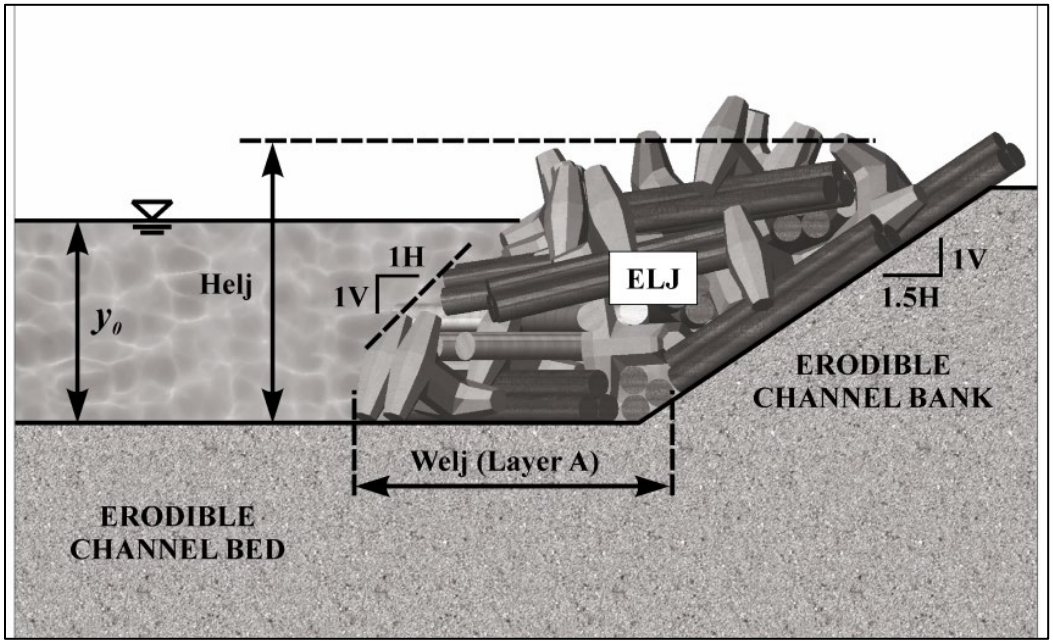


Source: FHWA.

**Figure 21. Drawing. Cross-sectional view of the model ELJs installed in the MFS test section.**

**Table 5. Prototype and model ELJ characteristics.**

| Parameter | Prototype | Model | Ratio |
|---|---|---|---|
| Height, $H_{elj}$ (ft) | 18 | 0.72 | 25 |
| Base width, $W_{elj}$ (ft) | 20 | 0.8 | 25 |
| Bank Slope, H:V | 1.0:1.0 | 1.0:1.0 | 1 |
| Length, $L_{elj}$ (ft) | 75 | 3.0 | 25 |
| Spacing, $L_s$ (ft) | 30 | 1.2 | 25 |
| Volume, $\forall_{elj}$ ($ft^3$) | 33,000 | 2.12 | 15,625 |

## EXPERIMENTAL PROTOCOLS AND RESULTS

The primary goals of the physical modeling experiments were to evaluate the effectiveness of ELJs in deflecting impinging flow away from the unstable eroding banks into the main channel, assess the hydrodynamic stability of the ELJs, and quantify the morphodynamic response of the channel to ELJs. The testing was conducted in three phases:

1. Phase I: experiments with an erodible bed (material I) to assess general performance of the ELJs in redirecting flow and identify erosion patterns around the ELJs.
2. Phase II: experiments using a fixed bed to assess hydraulic loading on the ELJs.
3. Phase III: experiments using an erodible bed (material II) to perform a detailed assessment of hydraulic loading and scour at a model scale compatible with the prototype site.

For the erodible bed experiments in phases I and III, the bed was prepared and the ELJ units were installed. The flume was slowly filled with water by gradually increasing the flow rate until the desired flow conditions were achieved. During each experiment, the researchers measured flow depths and velocities and recorded videos of the experiment. Equilibrium scour experiments ran for a 24-hr period. ELJ stability experiments also ran for a 24-hr period unless total structure failure of the ELJ was observed. The researchers then scanned pretest (as-built) and post-test (equilibrium) geometries and bathymetries to compare the two.

### Phase I: ELJs and Erosion Patterns

#### *General Approach*

The approach for evaluating ELJ performance and erosion patterns in phase I was to generate flow conditions that would cause some damage to the bank model prior to ELJ installation; that is, to create combinations of velocity and depth that were at the threshold of clear-water and live-bed conditions in the erodible bed channel in the absence of ELJs. Figure 22 and figure 23 show a before and after condition, respectively, for run I-1 using scanned point-cloud bathymetries (resolution 0.063 inches by 0.063 inches) of the half trapezoidal erodible channel. Selecting these threshold conditions provided an opportunity to assess the role of ELJs in protecting the bed and banks from erosion.

Phase I experiments tested the performance of the initial ELJ design provided by WFLHD (appendix A) for resisting flow and scour. As part of preparing the initial model ELJs, it became apparent that different packing densities for the model ELJ components, that is, the number of

log–dolos bundles and rootwads, could vary significantly and might affect ELJ stability and performance. Therefore, the phase I experiments also explored variations in well-packed and stable ELJ units with the necessary height to accommodate the design water depth. In addition, the experiments were designed to test the assumption that the log mass would settle into scour holes as scour occurred without destabilizing the overall structure and functionality of the ELJ.

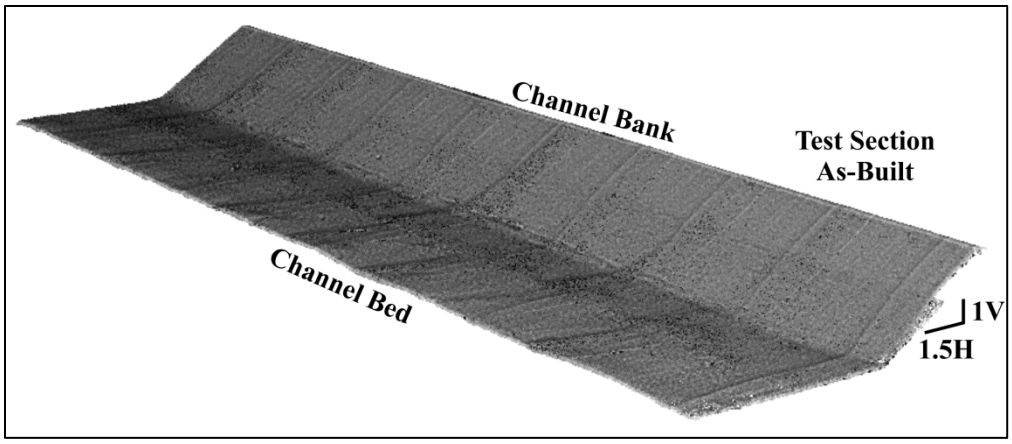


Source: FHWA.

**Figure 22. Graphic. Laser-scanned bathymetry of the erodible half trapezoidal channel before testing (as-built) for run I-1.**

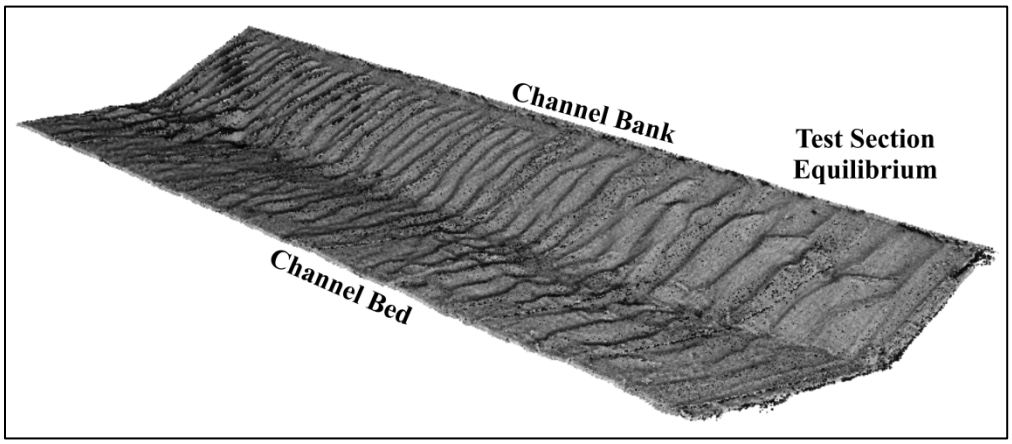


Source: FHWA.

**Figure 23. Graphic. Laser-scanned bathymetry of the erodible half trapezoidal channel after testing (equilibrium) for run I-1.**

Because the geometry of the model scale in the horizontal direction was distorted from the prototype, $V_M$ was defined in two ways in the experiments to see if one was more relevant for evaluating and designing ELJs. The first way defined $V_M$ as $V_U$, that is, $V_M = V_U$, as was depicted in figure 14. The second defined $V_M$ as $V_{ADJ}$ so that $V_M = V_{ADJ}$. $A_U$ and $A_{ADJ}$ represented the cross-sectional area in the upstream and adjacent cross sections, respectively, as was depicted in figure 15. Given a value of $V_M$, the case where $V_M = V_U$ was more severe in terms of scour and channel-bank erosion than was the case where $V_M = V_{ADJ}$.

Figure 24 shows cross-sectional locations, defined as CS-1 through CS-5, where velocity measurements were taken. $V_U$ and the corresponding depth and area were measured at CS-1. $V_{ADJ}$ and its corresponding parameters were measured at CS-2. Measurements at the other cross sections were also recorded. All velocity measurements were taken at 40 percent of the flow depth (60 percent below the water surface) as a representative depth-averaged velocity.

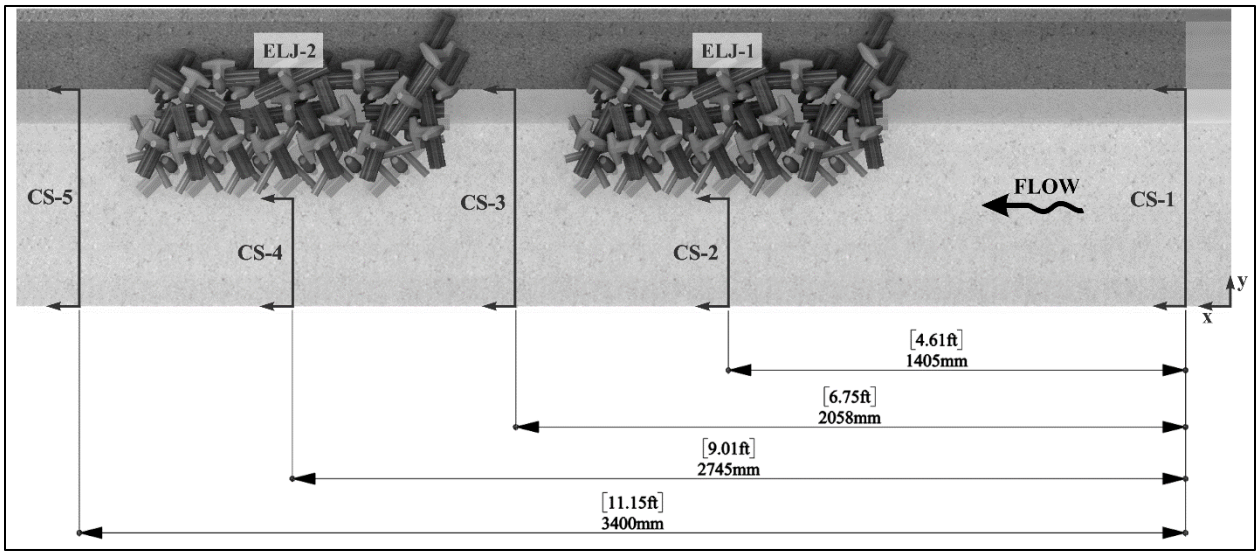


Source: FHWA.

**Figure 24. Graphic. Plan view of cross sections CS-1 to CS-5 (ELJ3 not shown).**

The experimental parameters for phase I are summarized in table 6. The model channel in phase I was prepared using material I with three ELJ units installed along the channel bank in series with a spacing (i.e., $L_s$) in between each unit as specified by the WFLHD design drawings. The ELJ installation process involved first placing the ELJ components on the channel bed (figure 25) and then on the channel bank (figure 26). The completed installation shown in figure 27 is for run I-3. The researchers conducted two variations on run I-3 (a and b) using different log–dolos packing densities, as described in the section on ELJ packing density that follows.

**Table 6. Experimental cases and hydraulic parameters for phase I.**

| Run | Case | $D_{50}$ (Inches) | $y_0$ (ft) | $V_M$ (ft/s) | Fr |
|---|---|---|---|---|---|
| I-1 | Baseline case $V_M = V_U$ | 0.014 | 0.59 | 0.82 | 0.2 |
| I-2 | ELJs with key dolosse $V_M = V_U$ | 0.014 | 0.59 | 0.83 | 0.2 |
| I-3a | ELJs with key dolosse $V_M = V_{ADJ}$ | 0.014 | 0.59 | 0.83 | 0.2 |
| I-3b | ELJs with key dolosse $V_M = V_{ADJ}$ | 0.014 | 0.59 | 0.83 | 0.2 |
| I-4 | ELJs without key dolosse $V_M = V_U$ | 0.014 | 0.59 | 0.82 | 0.2 |

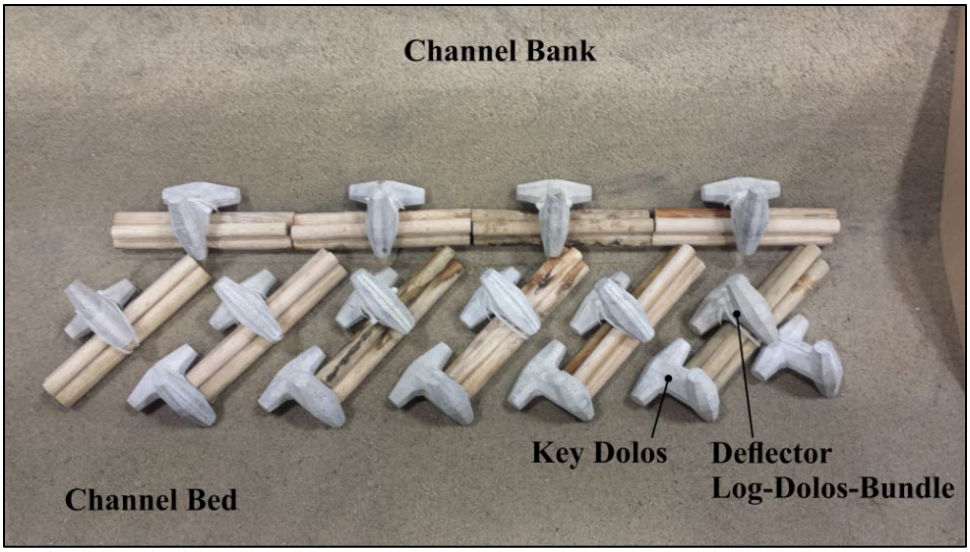


Source: FHWA.

**Figure 25. Photo. Installation of the initial layer of log–dolos bundles and key dolosse on the channel bed for run I-3.**


Source: FHWA.

**Figure 26. Photo. Installation of log–dolos bundles on the channel bank for run I-3.**

Source: FHWA.

**Figure 27. Photo. As-built ELJ installation for run I-3 with log–dolos bundles, rootwads, and key dolosse.**

### *Observations and Findings*

Findings from the phase I experiments are grouped into three categories: the density of log–dolos units required to promote stability, scour patterns at the edge of the ELJ units, and the role of key dolosse in stabilizing the ELJ units. Each of these observations is discussed in the following sections.

#### *ELJ Packing Density*

The initial installation plan for each ELJ unit from the WFLHD design drawing (appendix A) called for 25 log–dolos bundles, 14 rootwads, and 7 key dolosse. The WFLHD design also specified that the height of the ELJ unit should exceed the expected flow depth under the design conditions, that is, $H_{elj} > y_0$. To build the ELJ unit height to satisfy this criterion, 8 additional log–dolos bundles were required for Runs I-2, I-3, and I-4 in layer B, bringing the total number of log–dolos bundles to 33. The log–dolos bundles were packed as densely as possible.

Figure 28 shows the bank failure associated with run I-3a when using the original ELJ unit design with 25 log–dolos bundles. The failure resulted because of the insufficient number of log–dolos bundles and inadequate protection of the channel bank at the upstream face of the ELJ unit, allowing significant flow to enter between the ELJ and the eroding channel bank. Figure 29 shows run I-3b hydraulic conditions but with an ELJ unit with 33 more densely packed

log–dolos bundles. No failure was observed after 24 hr in this case. This change increased the density of log–dolos bundles from 0.00076 to 0.0010 bundles/ft$^3$. On a mass basis, the dolosse and wood combined within the ELJ unit for a density of 72.9 and 71.4 lb/ft$^3$ for the prototype and model, respectively. For both the prototype and model, the void ratio of the ELJ unit was 0.71. With this revised configuration, the submerged density of the ELJ unit was 65.5 and 65.1 lb/ft$^3$ for the prototype and model, respectively.

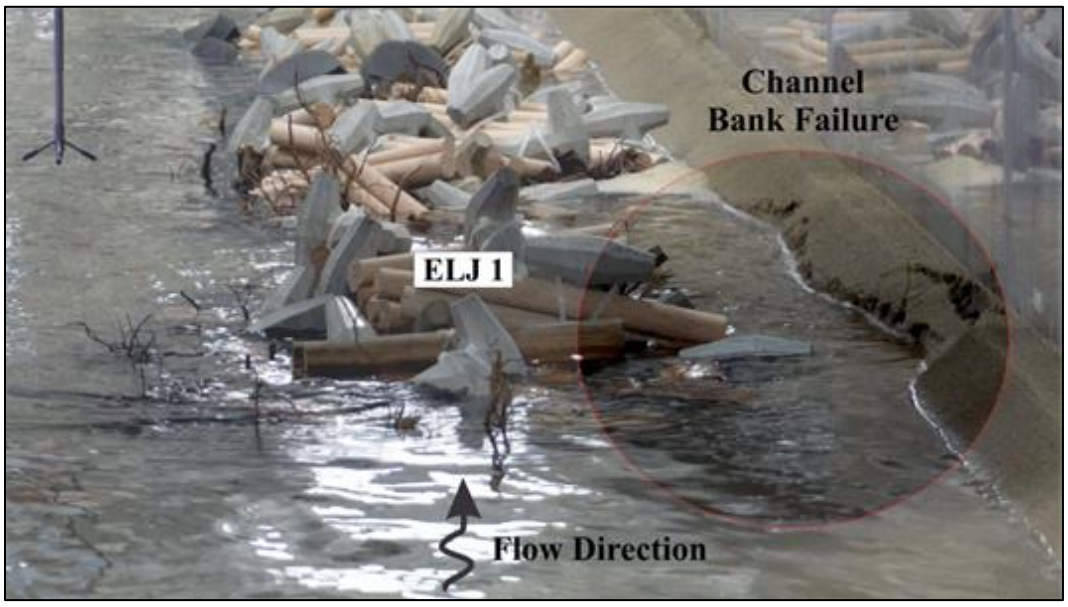


Source: FHWA.

**Figure 28. Photo. Run I-3a with 25 log–dolos bundles showing channel-bank failure.**

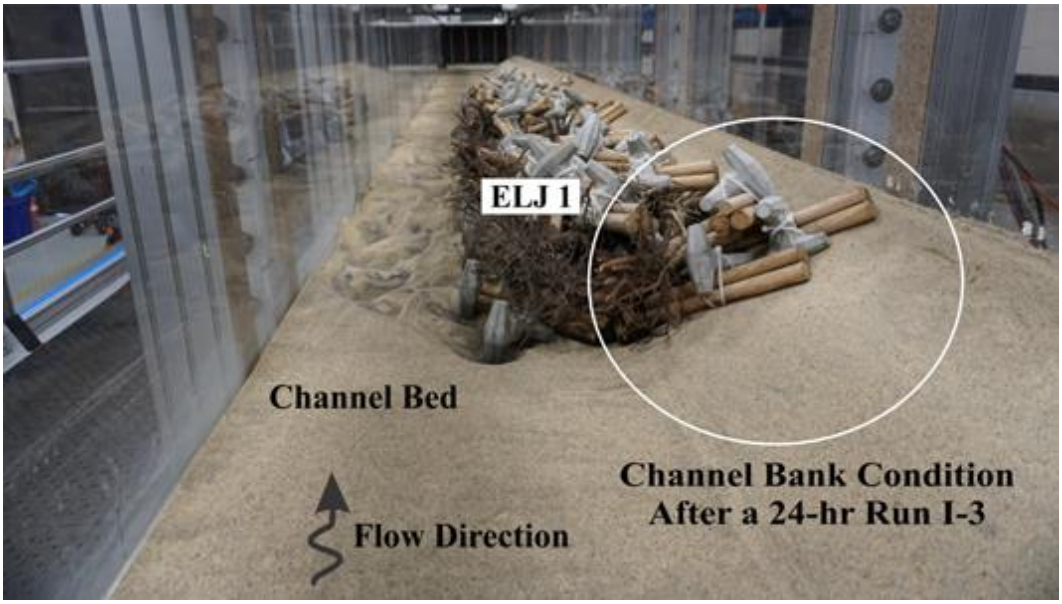


Source: FHWA.

**Figure 29. Photo. Run I-3b with 33 log–dolos bundles showing no bank failure.**

A flatter bank slope requires a larger number of log–dolos bundles than a steeper bank slope to maintain the same density of bundles for a well-packed ELJ unit. It is possible that a bank slope steeper than 1.5:1 (H:V) was assumed for the WFLHD design and resulted in an underestimate of bundles needed for this model implementation.

*ELJ Bank Protection and Bed Scour*

After increasing the number of log–dolos bundles and their density, the researchers repeated run I-2 and completed runs I-3 and I-4. Figure 30 depicts scanned bathymetries of the equilibrium bed scour formations around the ELJ units for the flow condition in run I-2. In this extreme (higher discharge) case, a large bed scour hole formed at the upstream edge of the first ELJ unit with a maximum scour depth of 0.54 ft. The scour hole formed because of a combination of local and contraction scour.

The scour hole induced some settlement of the ELJ unit, but this settlement was not significant and did not cause any measurable effect on the unit's stability or as-built geometry. Significant settlement of the ELJ could have caused the ELJ structure to tilt forward into the main channel, leaving the bank surface unprotected, but this did not occur because of the flexible log–dolos bundles and logs with rootwads.

Figure 31 depicts scanned bathymetries of equilibrium bed scour formations around the ELJ units for the flow condition in run I-3. For this case, the deepest bed scour formed adjacent to the first ELJ unit with a maximum scour depth of 0.15 ft. Scour depth for run I-4 was approximately equivalent to that for run I-2. Maximum scour depths are summarized in table 7.

**Table 7. Maximum scour depths at the ELJ units.**

| Run | Case | $y_s$ (ft) | $y_s / y_0$ |
|---|---|---|---|
| I-2 | ELJs with key dolosse $V_M = V_U$ | 0.54 | 0.92 |
| I-3 | ELJs with key dolosse $V_M = V_{ADJ}$ | 0.15 | 0.25 |
| I-4 | ELJs without key dolosse $V_M = V_U$ | <0.54 | 0.92 |

Importantly, the scour maps (figure 30 and figure 31) do not show net erosion or deposition along the bank where the ELJs were placed. The three ELJ units placed along the channel bank effectively created low-flow zones in the unprotected spaces between them, demonstrating their efficacy in bank protection.

*Key Dolosse*

Another observation derived from the phase I experiments relates to the role of key dolosse in promoting stability of the ELJ unit. The key dolosse were placed as single elements on the channel bed, as depicted in figure 25, and are the only elements that are not well interlocked in the ELJ system. Figure 32 shows a failed key dolosse moved out of position and separated from the ELJ unit. Figure 33 depicts the local scour around a failed key dolosse. The researchers observed that, as the scour developed around ELJs, the single key dolos was undermined and, in run I-2, launched into the scour hole. The observed edge failure of the key dolosse did not have a negative effect on the overall stability of the ELJ units, but also did not have a positive effect, either. The key dolosse appeared to be the only components of the ELJ unit vulnerable to scour.

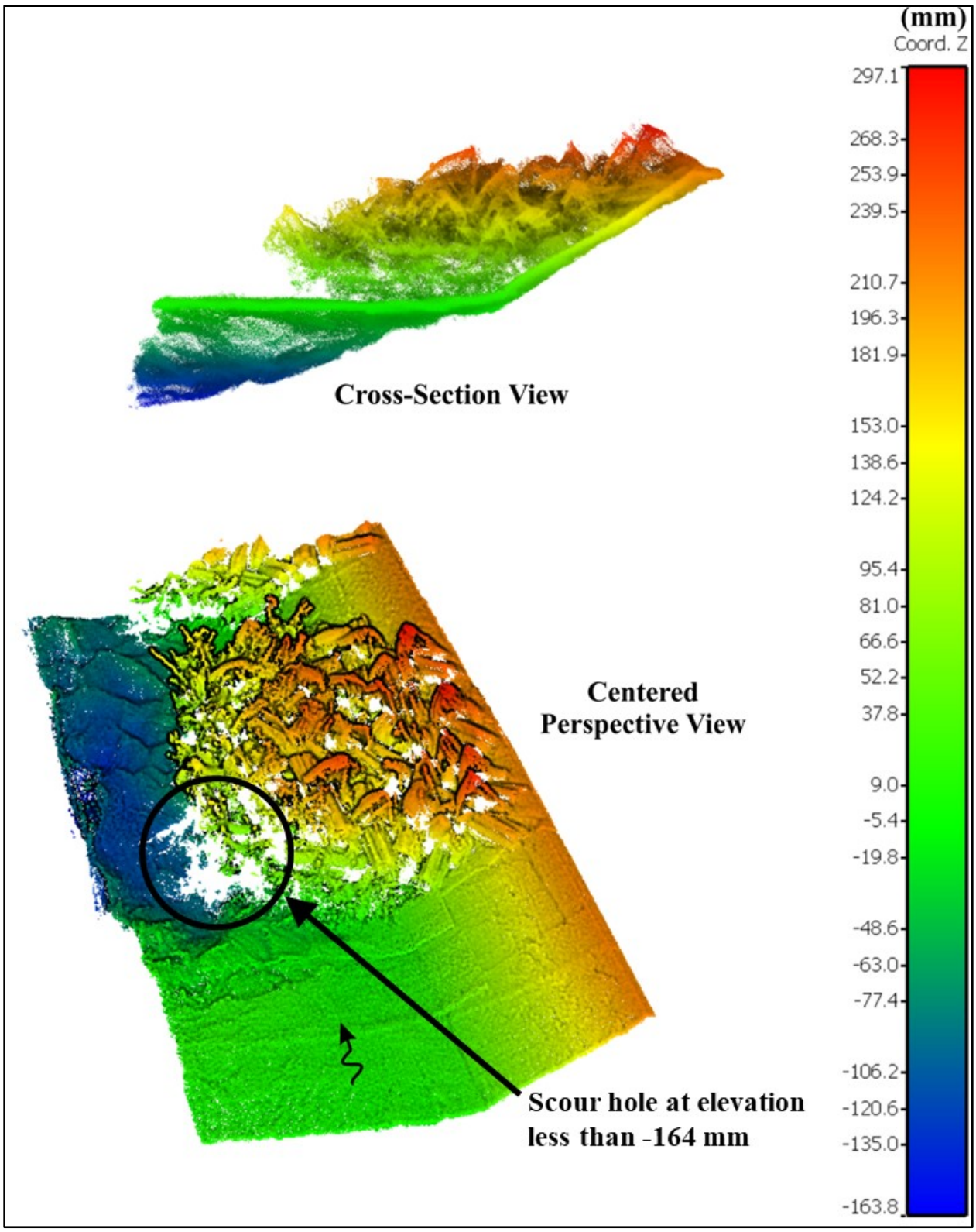


Source: FHWA.

**Figure 30. Graphic. Bathymetric map showing ELJ unit and scour for run I-2.**

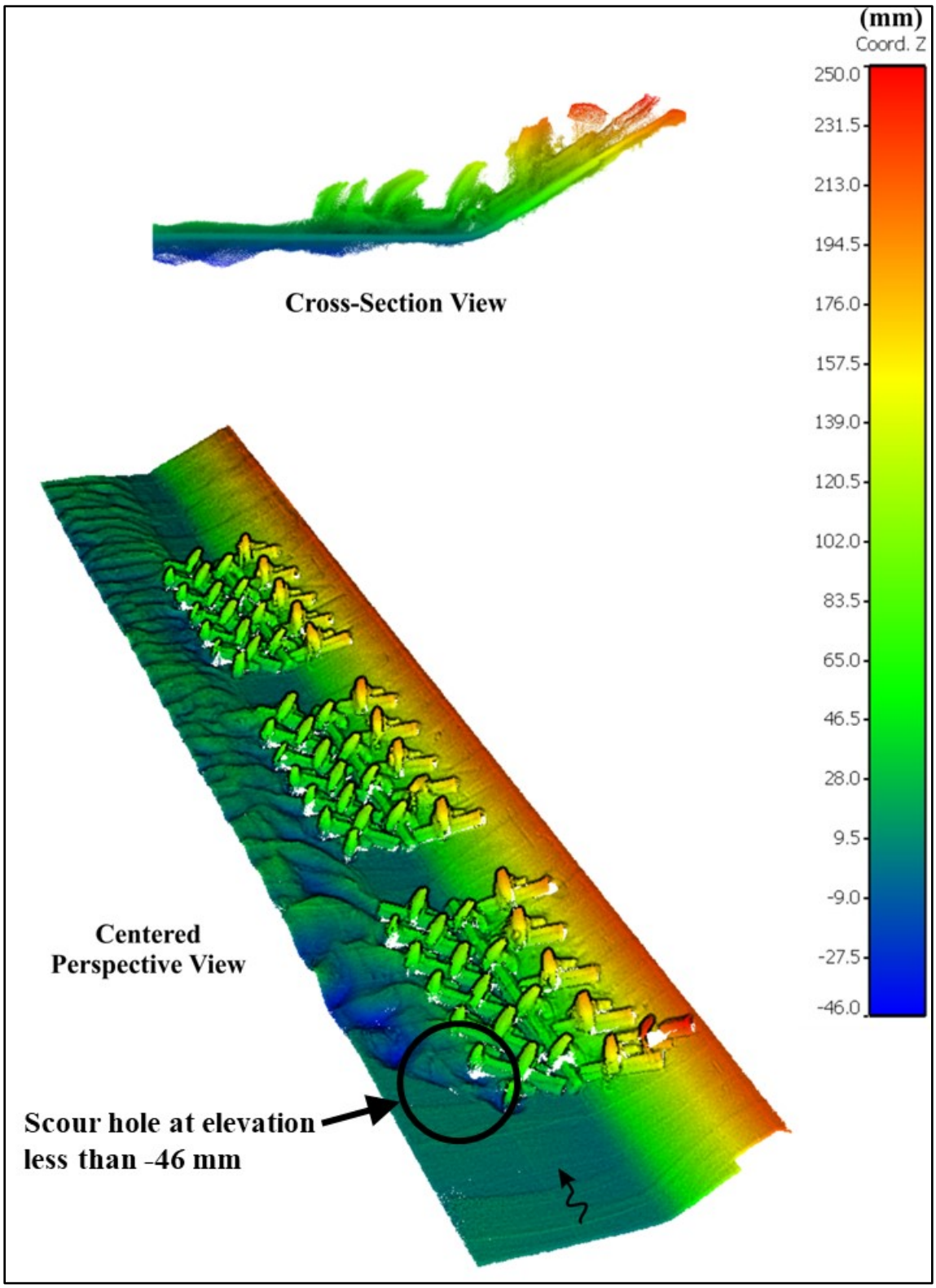


Source: FHWA.

**Figure 31. Graphic. Bathymetric map showing ELJ unit (with layer B removed) and scour for run I-3.**

Source: FHWA.

**Figure 32. Photo. Total edge failure of key dolosse in run I-2.**

Source: FHWA.

**Figure 33. Photo. Local scour hole developed around the key dolosse in run I-2.**

## Phase II: Hydrodynamic Loads on ELJs

### *General Approach*

The goals of the phase II experiments were to measure drag force ($F_D$) and transverse force ($F_T$) acting on an ELJ unit and estimate a drag coefficient ($C_D$). Moreover, the hydrodynamic force measurements were used to calibrate the ELJ model for CFD simulations described in chapter 4.

For this phase, the researchers conducted experiments in a half-trapezoidal channel with a nonerodible (acrylic sheeting) bed and bank having the same cross-sectional geometry as in phase I (figure 14). Based on the experimental observations from phase I regarding the preferred number of log–dolos bundles, an ELJ unit was fabricated using 33 bundles with all the components glued together to form a rigid unit. The ELJ unit was mounted to a force-torque sensor, which was attached to a robotic arm as shown in figure 34. The instrumented ELJ was suspended parallel to bed and bank with 0.39-inch and 0.20-inch gaps to the bed and bank, respectively, as shown in figure 35. The ELJ upstream face was positioned perpendicular to the main flow direction.


Source: FHWA.

**Figure 34. Photo. ELJ model connected to the force-torque sensor mounted on the robotic arm.**

Because of the maximum load limitations of the force-torque sensor and the robotic arm, a lighter version of the ELJ unit was required. To meet this need, new log–dolos bundles were fabricated substituting plastic dolosse for the concrete dolosse. The plastic dolosse were created using a 3D printer and acrylonitrile butadiene styrene plastic.

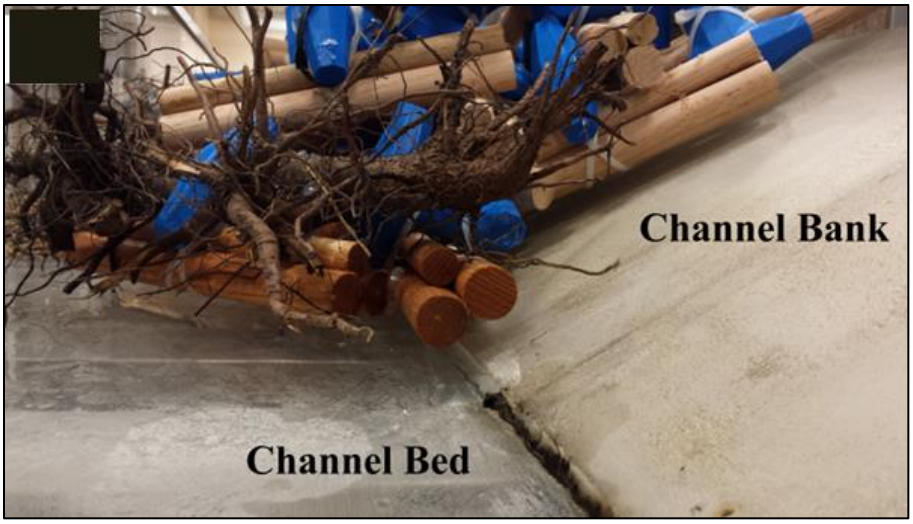


Source: FHWA.

**Figure 35. Photo. Close-up view of the suspended ELJ model showing the respective clearances to the channel bed and bank.**

Researchers used a force-torque sensor to measure forces ($F_x$, $F_y$, $F_z$) and torque ($T_x$, $T_y$, $T_z$) in three dimensions. Specifications for the maximum dynamic range and resolution of the sensor in each direction are in table 8. Flow velocities were collected using an acoustic velocimeter (figure 13) for a range of flow velocities.

Table 9 summarizes the experimental parameters, including $A_{elj}$, which is defined as the area of the ELJ unit orthogonal to the flow. The researchers completed each run four times to validate repeatability of the results.

**Table 8. Force-torque sensor maximum dynamic ranges and resolutions.**

| F-T Sensor | $F_x$, $F_y$ (N) | $F_z$ (N) | $T_x$, $T_y$ (N·m) | $T_z$ (N·m) |
|---|---|---|---|---|
| Range | 65 | 200 | 5 | 5 |
| Resolution | 0.025 | 0.05 | 0.0015 | 0.0015 |

1 N·m = 0.737 pound-feet.

**Table 9. Experimental parameters used in phase II.**

| Run | $y_0$ (ft) | $V_U$ (ft/s) | Fr | $A_{elj}$ (ft$^2$) | $F_D$ (N) | $F_T$ (N) | $C_D$* |
|---|---|---|---|---|---|---|---|
| II-1 | 0.62 | 1.03 | 0.23 | 0.667 | 13.24 | 0.42 | 4.3 |
| II-2 | 0.66 | 1.31 | 0.29 | 0.710 | 25.44 | −0.91 | 4.8 |
| II-3 | 0.69 | 1.51 | 0.32 | 0.743 | 37.97 | −1.32 | 5.2 |
| II-4 | 0.72 | 1.66 | 0.34 | 0.775 | 48.52 | −1.82 | 5.1 |

*Drag coefficient computed using the net area blocked, not the full frontal area of the ELJ unit. These values are not comparable to later estimates using the full frontal area.

With the flow running in the test section and the ELJ model above the water surface, the force-torque sensor was biased to zero. The robotic arm then slowly lowered the ELJ model into position where the hydrodynamic forces acting on the ELJ were collected at 1,000 HZ. The

collected raw data were post-processed by applying a fast Fourier transform filter and mean values were obtained.

### *Observations and Findings*

Figure 36 displays the longitudinal force ($F_x$), which is predominantly the drag force ($F_D$), measured for the runs summarized in table 9. Figure 37 displays the transverse force ($F_T$), which is the force in the *y*-direction, from the same runs. The averaged forces and computed $C_D$ are summarized in table 9. The cases varied from a partially inundated ELJ unit (run II-1) to an almost fully inundated unit with higher approach flow (run II-4). The force-torque sensor started to collect data with the ELJ unit elevated above the water surface. As the robot arm lowered the ELJ, $F_D$ increased with an increasing Froude number, while transverse force generally stayed near zero.

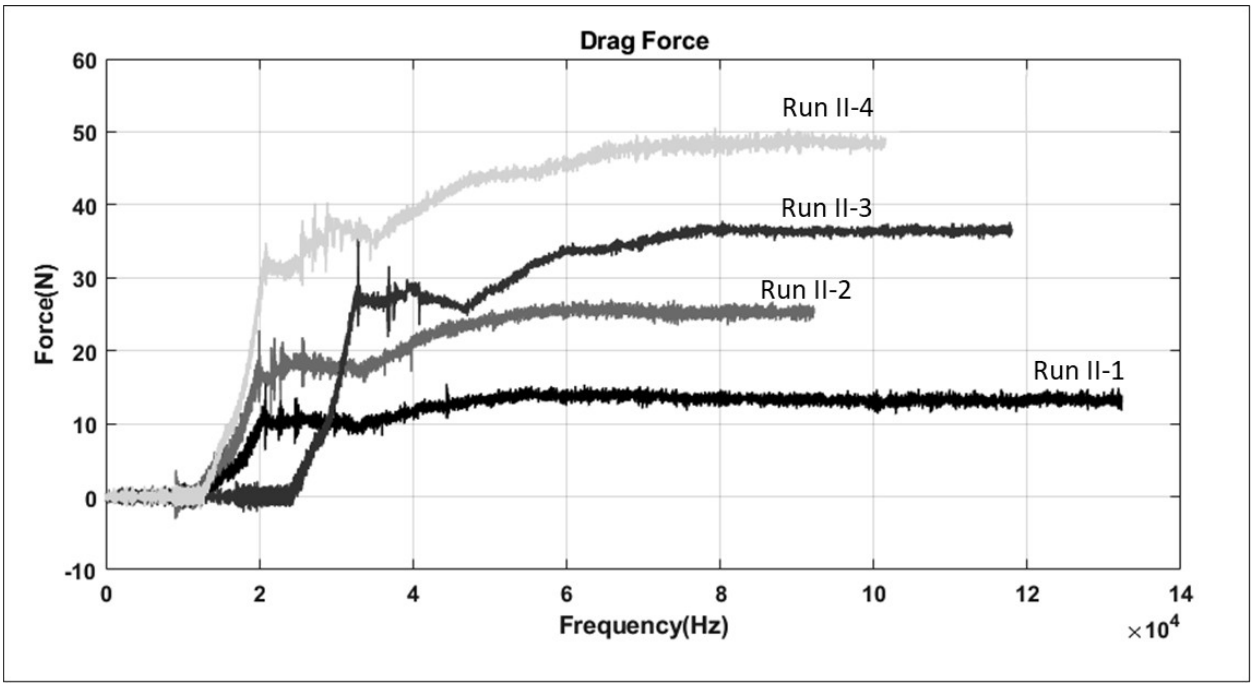


Source: FHWA.

**Figure 36. Graph. Longitudinal (drag) forces from phase II experiments.**

Computation of $C_D$ requires an estimate of $A_{elj}$. The upstream face of the ELJ unit is shown in figure 38. Laser scan measurements of the cross-sectional upstream face are shown in figure 39. This measurement changed slightly with the increasing flow depths. The researchers combined the experimental results with the CFD simulations to obtain a characteristic $C_D$, which can be used in prototype design.

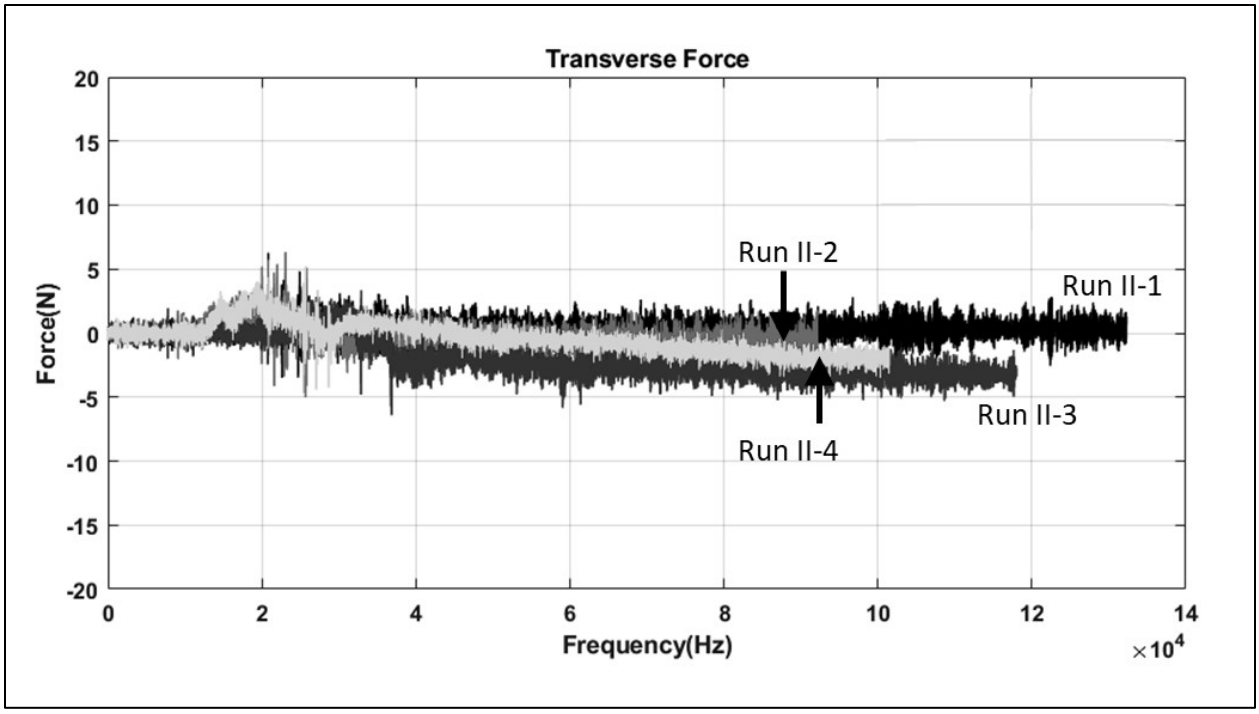


Source: FHWA.

**Figure 37. Graph. Transverse forces from phase II experiments.**

Source: FHWA.

**Figure 38. Photo. Upstream face of the ELJ unit.**

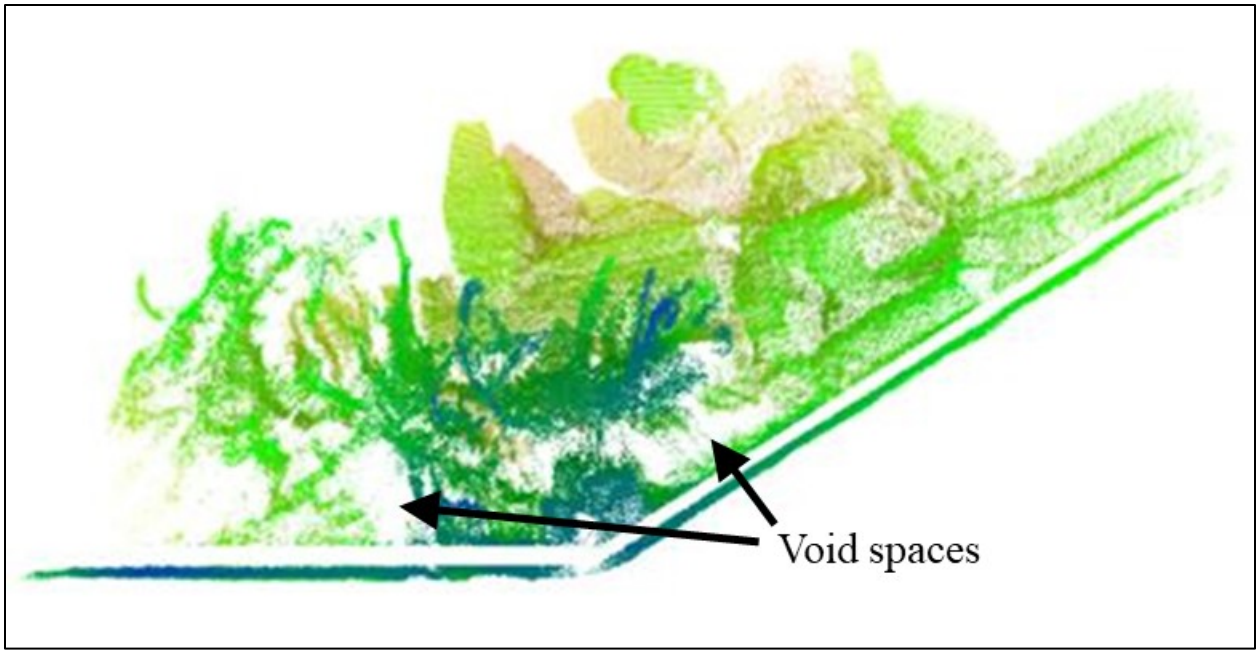


Source: FHWA.

**Figure 39. Graphic. Laser scan of the ELJ upstream face used to compute the cross-sectional area perpendicular to the flow.**

## Phase III: ELJ Stability Experiments

### *General Approach*

Experiments in phase III were conducted on the erodible half-trapezoidal channel with the coarser bed and bank material (material II). The scale of this material is more representative of the channel bed of the Hoh River and offers a better basis for evaluating ELJ stability under design and extreme flow conditions for the Hoh River prototype. Overall ELJ stability relies on both a good interlock between the ELJ elements to resist flow and stability of the eroding channel. One of the main objectives in these series of experiments was to investigate the potential failure modes of the ELJs in response to hydrodynamic forces and an unstable eroding channel.

For this phase, two ELJ units were installed in the test section for each run except run III-2, which included three ELJ units. The ELJ units were designed and constructed in the same manner described in phase I with 33 log–dolos bundles for each ELJ unit. Table 10 summarizes the tests included in this phase.

Run III-1 was the baseline case to confirm that the bed and bank material was near threshold movement conditions at the given depth and velocity. Runs III-2 and III-3 tested the ELJ during unsubmerged conditions (i.e., the top of the ELJ is higher than the water surface), while runs III-4 through III-9 explored the ELJ during fully submerged conditions. As in phase I, two definitions of the characteristic model velocity were used: $V_M$ taken as the approach velocity $V_U$ and $V_M$ taken as the adjacent velocity $V_{ADJ}$.

The researchers conducted each run in this series for a 24-hr duration to ensure equilibrium scour was reached unless total structure failure of the ELJ was observed. They scanned the geometries of installed ELJs and channel equilibrium bathymetries in both before and after conditions to compare as built and final states. They also made video recordings of each run to capture potential failure modes and failure zones when ELJ structures failed.

**Table 10. Experimental cases and hydraulic parameters for phase III.**

| Run | Case | $D_{50}$ (Inches) | $y_0$ (ft) | $V_M$ (ft/s) | Fr |
|---|---|---|---|---|---|
| III-1 | Baseline Case: $V_M = V_U$ | 0.18 | 0.59 | 2.40 | 0.55 |
| III-2 | $V_M = V_{ADJ}$ | 0.18 | 0.59 | 2.40 | 0.55 |
| III-3 | $V_M = V_U$ | 0.18 | 0.59 | 2.40 | 0.55 |
| III-4 | $V_M = V_{ADJ}$ | 0.18 | 0.75 | 2.40 | 0.49 |
| III-5 | $V_M \rightarrow V_U$ | 0.18 | 0.75 | 2.04 | 0.41 |
| III-6 | $V_M \rightarrow V_U$ | 0.18 | 0.75 | 2.16 | 0.44 |
| III-7 | Layer A with riprap: $V_M \rightarrow V_U$ | 0.18 | 0.75 | 2.16 | 0.44 |
| III-8 | Layer A partially buried: $V_M \rightarrow V_U$ | 0.18 | 0.75 | 2.64 | 0.54 |
| III-9 | Dolosse at upstream ELJ face: $V_M \rightarrow V_U$ | 0.18 | 0.75 | 2.64 | 0.54 |

***Observations and Findings***

Experimental results in phases I and II showed that overall ELJ stability relies on both good interlock between the ELJ unit elements and stability of the eroding channel. Therefore, one of the main objectives in this phase was to investigate potential failure modes when both hydrodynamic forces and unstable channel erosion occur simultaneously at ELJ installations.

*ELJ Stability for Partially Submerged Conditions (Prototype Design Conditions)*

Figure 40 shows the installation of two ELJ units for run III-3. Runs III-2 and III-3 represented prototype (50-yr flood event) design conditions where the ELJs had sufficient height to extend above the water surface elevation ($y_0 < H_{elj}$), as shown in figure 41. Run III-2 tested the condition where the flow depth and velocity were set based on conditions adjacent to the ELJ ($V_M = V_{ADJ}$), which was 2.4 ft/s. Figure 42 shows the measurements from which the velocity was determined (CS-4). Run III-3 tested the more severe condition where the flow depth and velocity were set based on the approach (upstream) condition ($V_M = V_U$), which was also 2.4 ft/s. Similarly, figure 43 shows the sources of this estimate (CS-1). Figure 24 defined cross-sectional locations.

In both runs, the ELJs were hydrodynamically stable. The total weight of the log–dolos bundles and rootwads exceeded buoyant and drag forces, resulting in no movement of the ELJ units. As seen in figure 41, the presence of some components above the water surface, which were not subject to either buoyant or drag forces, aided stability. The dense packing arrangement between the log–dolos bundles contributed to transferring their dry weight downward onto the elements of layer A.

Source: FHWA.

**Figure 40. Photo. As-built ELJ installations on the erodible channel for run III-3.**

Source: FHWA.

**Figure 41. Photo. ELJs under partially submerged conditions in run III-3 (looking downstream).**

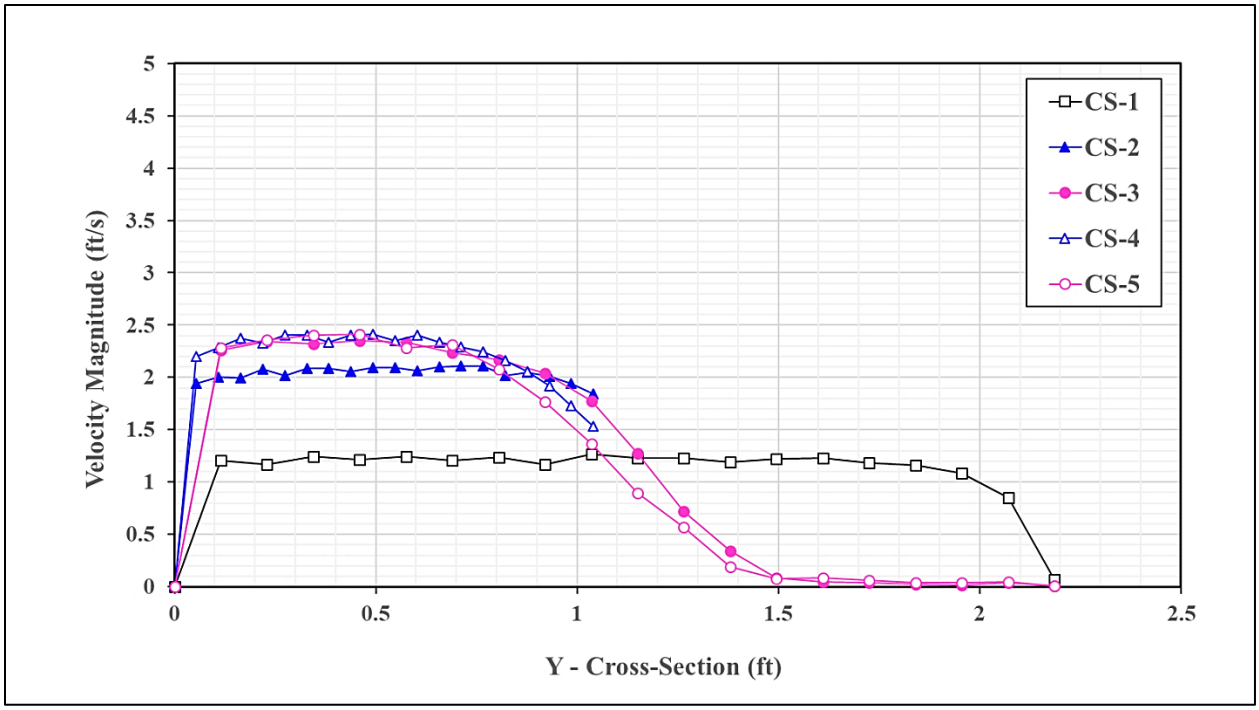


Source: FHWA.

**Figure 42. Graph. Cross-sectional velocity profiles measured at 40 percent of flow depth for run III-2.**

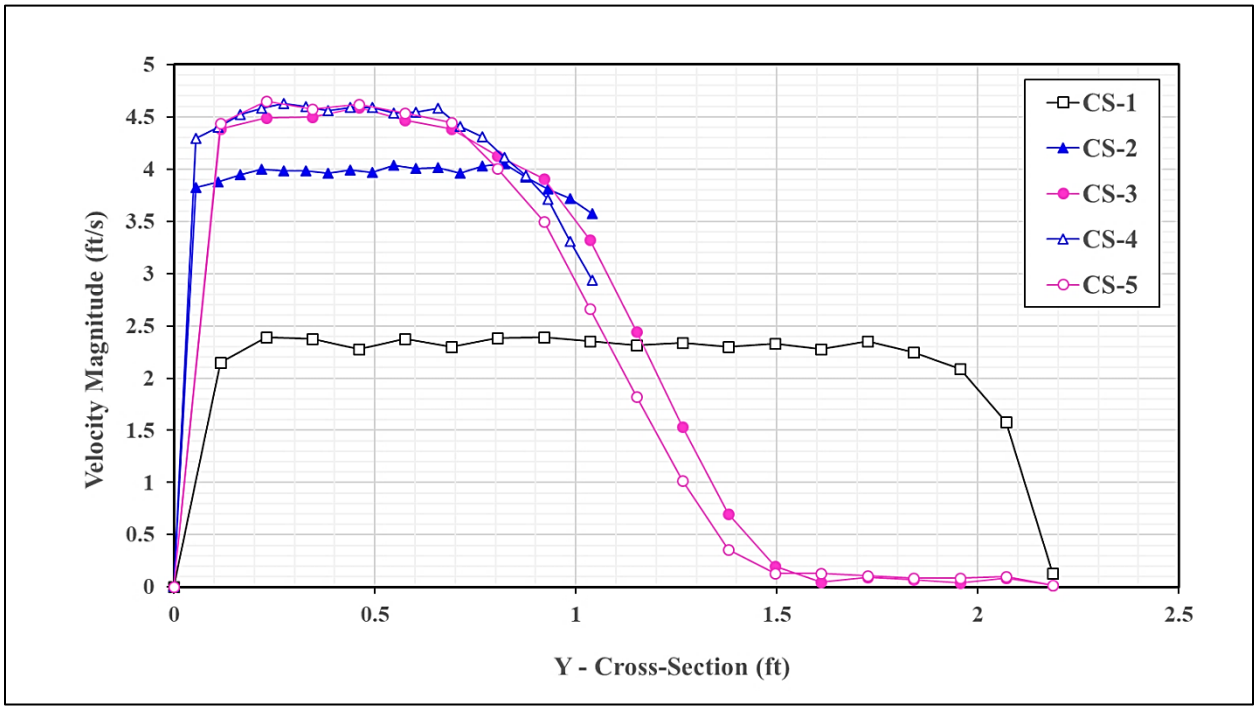


Source: FHWA.

**Figure 43. Graph. Cross-sectional velocity profiles measured at 40 percent of flow depth for run III-3.**

A small equilibrium scour hole appeared in the channel bed between ELJ2 and ELJ3 in run III-2, as shown in figure 44, and between ELJ1 and ELJ2 in run III-3, as shown in figure 45. The bed scour depths are summarized in table 11. As observed in phase I and expected in this phase, the more severe condition of run III-3 resulted in more severe scour. Key dolosse were installed along ELJ2 in run III-3. They launched into the scour hole for that run, confirming the conclusion from phase I that key dolosse do not provide support for ELJ stability. Significant channel-bank erosion behind the ELJs was not observed in either run.

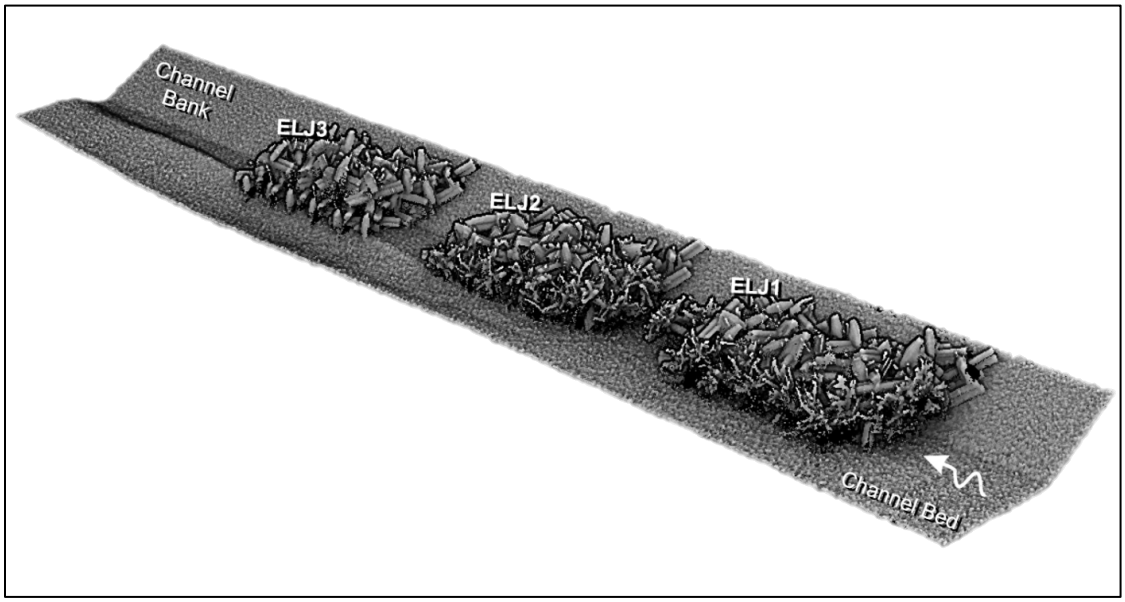


Source: FHWA.

**Figure 44. Graphic. Bathymetric scan of run III-2 at equilibrium conditions.**

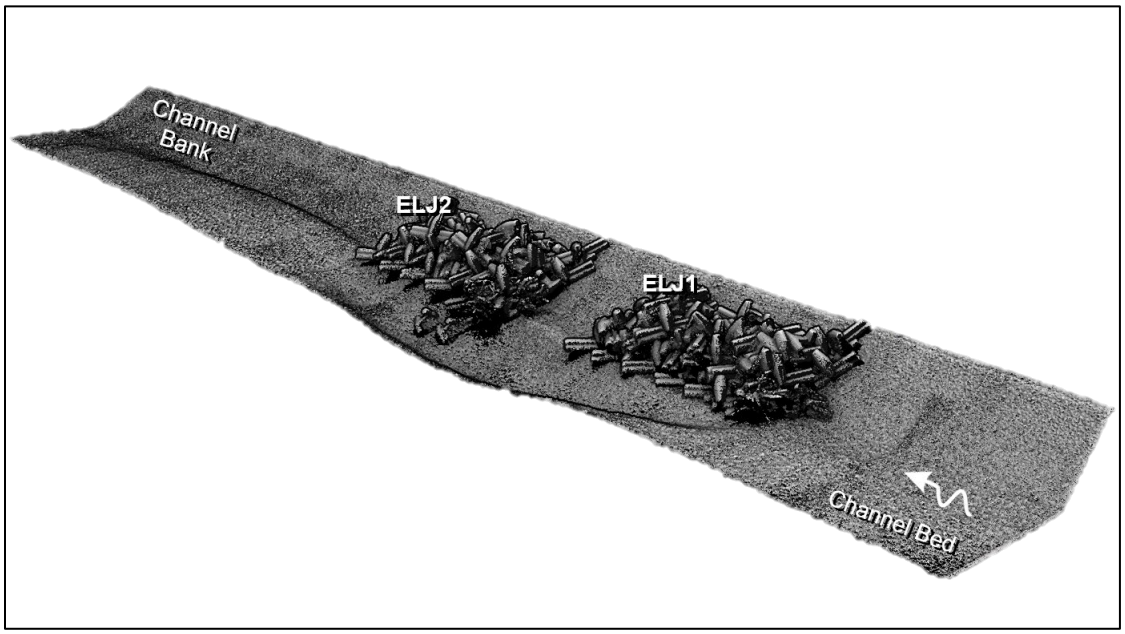


Source: FHWA.

**Figure 45. Graphic. Bathymetric scan of run III-3 at equilibrium conditions.**

**Table 11. Maximum scour depths at the ELJ units.**

| Run | Case | $y_s$ (ft) | $y_s / y_0$ |
|---|---|---|---|
| III-2 | $V_M = V_{ADJ}$ | 0.29 | 0.49 |
| III-3 | $V_M = V_U$ | 0.52 | 0.88 |
| III-4 | $V_M = V_{ADJ}$ | 0.28 | 0.37 |
| III-5 | $V_M \rightarrow V_U$ | * | * |
| III-6 | $V_M \rightarrow V_U$ | * | * |

*Maximum scour depth not measured because of ELJ failure.

*ELJ Stability for Fully Submerged Conditions (Extreme Conditions)*

The researchers conducted three test runs where the ELJs were in fully submerged conditions ($y_0 \geq H_{elj}$), which were more extreme than the design conditions. In each of these test runs, depth was increased to 0.75 ft with a target velocity of 2.4 ft/s. Catastrophic failure of the ELJs occurred prior to reaching this condition for some of these tests. For those cases, velocities were recorded at the moment of failure and the failure mode noted.

Run III-4 included two fully submerged test units, as shown in figure 46. This run represented velocity as the adjacent velocity ($V_M = V_{ADJ}$). Although fully inundated, no hydrodynamic failure of the ELJs was observed. Small displacements or rotations of some elements in top layer B were observed, such as the movement of a rootwad log, shown in figure 47, and the rotation and displacement of single log–dolos bundles installed on the top layer, shown in figure 48. These results demonstrate that log–dolos bundles could turn and displace without compromising the overall stability of ELJ structures. However, special care in the placement of the logs with rootwads during installation is important because they are vulnerable to buoyancy forces. In addition, small displacements and rotations of the log–dolos bundles can cause total dislodgment of the logs with rootwads from the ELJ unit.

The researchers did not observe significant channel-bank erosion in run III-4. The maximum equilibrium scour hole in the channel bed measured 0.28 ft deep and developed around the ELJ2, as shown in figure 49. This scour depth was slightly less than was measured for run III-2, although the flow depth was greater (table 11). A possible explanation for lower scour is that run III-4 did not include key dolosse while run III-2 did; the key dolosse may have increased the scour depth.

Source: FHWA.

**Figure 46. Photo. Fully submerged ELJ units in run III-4.**

Source: FHWA.

**Figure 47. Photo. Model log (representing a rootwad) from ELJ1 caught at the upstream face of ELJ2 (downstream unit).**

Source: FHWA.

**Figure 48. Photo. Log–dolos bundle from ELJ1 (upstream unit) turned upside down.**

Source: FHWA.

**Figure 49. Photo. Bed scour around ELJ2 (downstream unit) at equilibrium conditions for run III-4.**

Runs III-5 and III-6 were tested with two ELJ units and with intended flow velocities defined as the upstream velocity ($V_M \rightarrow V_U$). However, before the intended velocity was reached in the

flume, one of the ELJ units experienced a complete failure. The velocity at failure was noted and defined as $V_M = V_{Failure}$. Run III-6 was a repeat of run III-5 to validate the ELJ failure threshold.

The researchers observed and video recorded the failure of the log–dolos bundles and logs with rootwads at the upstream face of ELJ1 (upstream unit). The approach velocities for runs III-5 and III-6 at the moment of failure were 2.04 ft/s and 2.16 ft/s, respectively, and are recorded in table 10. In both cases, these velocities were less than the target velocity of 2.4 ft/s.

The failure mode and location were consistent for the two runs. Figure 50 shows the initiation of failure at the upstream face of ELJ1, and figure 51 shows the advancing failure during run III-6. Once the upstream face of the ELJ unit failed, a domino failure effect on the entire ELJ1 unit occurred. In addition, many of the elements from ELJ1 struck the second unit (ELJ2), located downstream, causing failure of ELJ2. For these extreme, fully submerged conditions, buoyancy forces reduced ELJ resistance to hydrodynamic loads, which was mostly achieved through good connection of their elements and by their total weight. Moreover, more cross-sectional areas of the ELJ units were exposed to the high-velocity approach flows.

In both run III-5 and run III-6, channel-bank erosion was visible and began to develop rapidly as velocity gradually increased to meet the target approach velocity $V_U$. Figure 52 shows a scan of the eroded channel bank behind the failed ELJ2. One of the causes of the erosive forces on the channel bank was the highly turbulent flow structure that developed on the water surface right above the inundated ELJs. This contributed to the total failure of the upstream ELJ unit (ELJ1).

These experiments were terminated after the researchers observed total failure of the ELJ units. No equilibrium bed scour conditions were achieved. Figure 53 shows laser scan results for the as-built structures compared with the final conditions after failure for run III-6.


Source: FHWA.

**Figure 50. Photo. Initial failure of ELJ1 during run III-6.**


Source: FHWA.

**Figure 51. Photo. Advancing failure of ELJ1 during run III-6.**

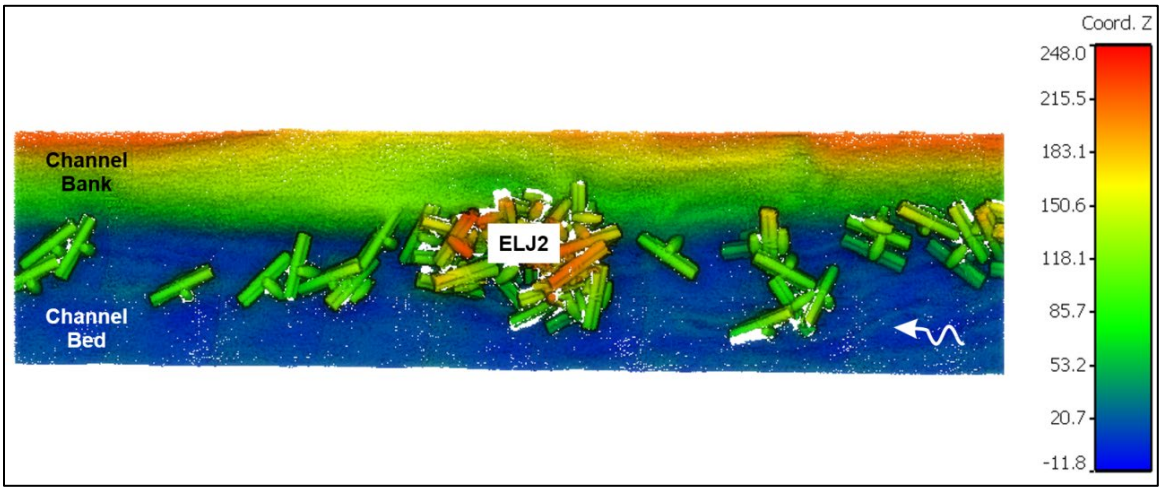


Source: FHWA.
Note: The scale represents the elevation in millimeters (the units intrinsic to the processing tool) in local coordinates where the as-built channel bed elevation is at 0 mm.

**Figure 52. Graphic. Bathymetric scan results of run III-6 after failure (plan view).**

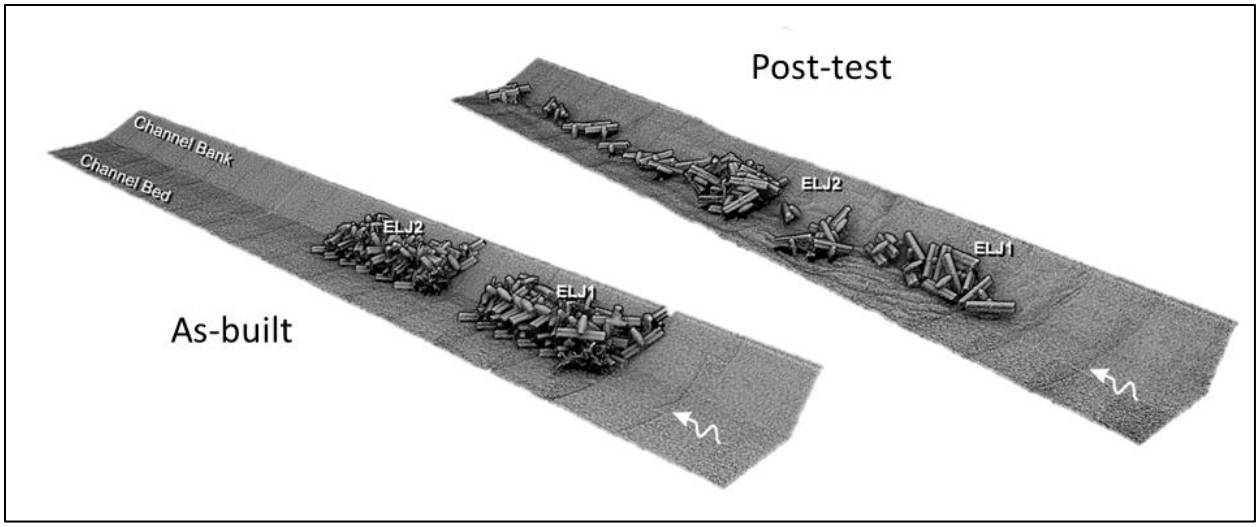


Source: FHWA.

**Figure 53. Graphic. Bathymetric scan results for run III-6.**

*Potential Improvement Strategies*

After identifying the failure modes of the ELJ units under fully submerged flow conditions, the researchers conducted three additional runs to investigate potential approaches for improving the hydraulic stability of the ELJ. Using two ELJ units in series for each run, they tested the following three strategies:

- Run III-7: Add a layer of riprap with layer A of the log–dolos bundles.
- Run III-8: Partially bury layer A of the log–dolos bundles.
- Run III-9: Place key dolosse at the upstream face of the ELJ unit.

For run III-7, the researchers filled gaps between the log–dolos bundles in the bottom layer (layer A) with riprap, as shown in figure 54, to investigate whether this would increase the resistance of the ELJ units. Figure 55 shows a close-up of the run III-7 ELJ installation. The median size of the uniform riprap used was $D_{50}$ = 0.6 inches (scaled to $D_{50}$ = 16 inches in the prototype). Failure was observed at the upstream face for ELJ1 (upstream unit), where the log–dolos bundles and logs with rootwads were dislodged, causing a domino failure effect on the entire ELJ1 structure. Failure resulted at a velocity of 2.16 ft/s, short of the target velocity of 2.4 ft/s. Because this was the same failure point in run III-6 (without riprap), providing the riprap did not improve ELJ stability. Figure 56 presents the bathymetric scan results for run III-7 in both as-built and final conditions after failure.

For run III-8, the researchers attempted to increase stability of the ELJ by partially burying the log–dolos bundles in the channel bed, as shown in figure 57. The ELJ units maintained their stability for the target approach velocity of 2.4 ft/s ($V_M = V_U$), with some displacements and rotations of the elements located on the top layers. This flow condition was maintained for approximately 2 hr with the ELJ units maintaining a stable position. The flowrate was then slowly increased to the point when elements began to dislodge from the upstream face of ELJ1 at $V_{Failure}$ = 2.64 ft/s, or 10 percent greater than the target velocity. Figure 58 displays the scan

results of both as-built and final bathymetric conditions for run III-8. Because failure did not occur until conditions went beyond the target, the strategy of partially burying the log–dolos bundles provided additional anchoring on the ELJs, preventing total collapse at the target velocity.


Source: FHWA.
Note: The dashed line marks the channel bank–bed intersection.

**Figure 54. Photo. Plan view of one ELJ units showing installation of layer A filled with riprap for run III-7.**

Source: FHWA.

**Figure 55. Photo. Close-up of the final installation with layer B on top of layer A for run III-7.**

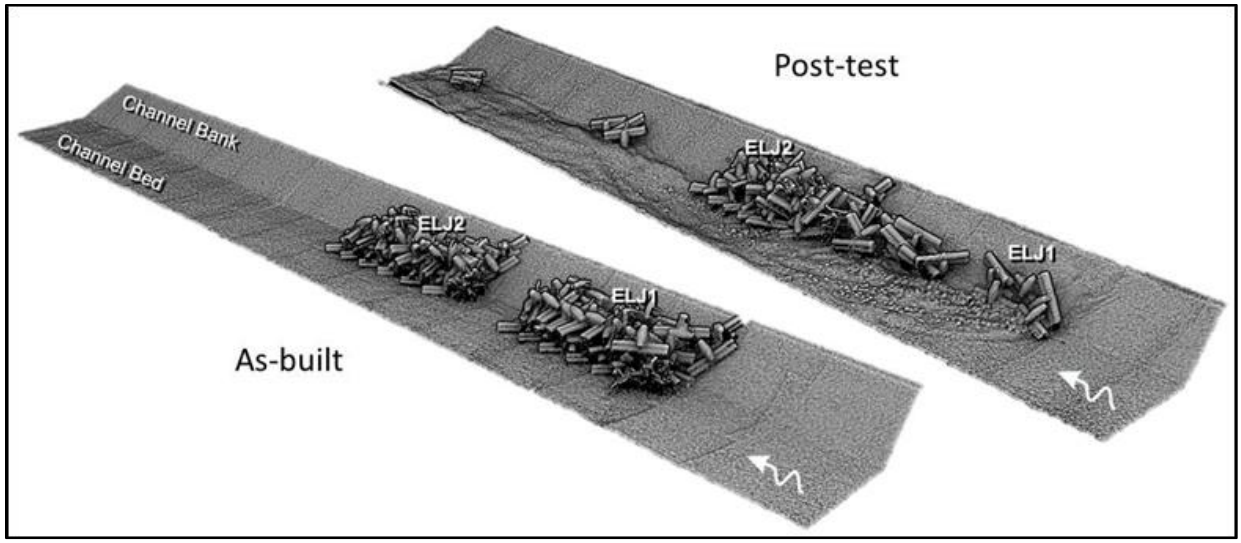


Source: FHWA.

**Figure 56. Graphic. Bathymetric scan results for run III-7.**


Source: FHWA.
Note: The dashed line marks the channel bank–bed intersection.

**Figure 57. Photo. Log–dolos bundles of layer A half buried in the channel bed with additional elements of layer B overlaid for run III-8.**

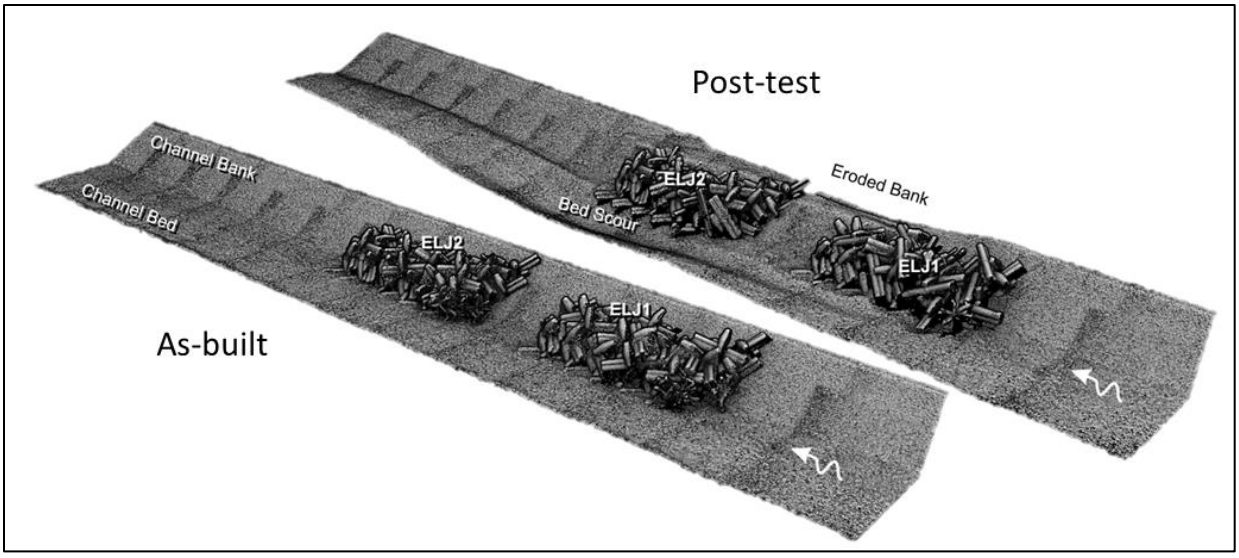


Source: FHWA.

**Figure 58. Graphic. Bathymetric scan results for run III-8.**

The strategy for enhancing stability tested in run III-9 was to reinforce the upstream face of the ELJs with six individual key dolosse. Figure 59 shows a close-up of this ELJ installation with five of the six individual key dolosse visible. This strategy performed well and increased the hydraulic stability of the ELJ units compared with the ELJ installation tested in runs III-5 and III-6. No failure of the ELJ units was observed for the target approach velocity of 2.4 ft/s ($V_M = V_U$), with some displacements and rotations of the elements located on the top layers. This flow condition was maintained for approximately 2 hr with the ELJ units maintaining a stable position. The flowrate was then slowly increased to the point when a few key dolosse began to dislodge from the upstream face of ELJ1 at $V_{Failure}$ = 2.64 ft/s, or 10 percent greater than the target velocity. Total failure of the ELJ units was not observed. Figure 60 displays scan results of the as-built and final bathymetric conditions for run III-9.

While the ELJ units in runs III-8 and III-9 were physically stable they were not entirely successful in preventing bank erosion. As observed in other runs with fully submerged ELJ conditions (i.e., runs III-4, III-5, and III-6), channel-bank erosion developed rapidly as velocity $V_M$ was gradually increased to the target approach velocity $V_U$. Highly turbulent structures developed on the water surface right above the inundated ELJs, causing erosion of the channel bank. The effects of bank erosion on ELJ stability were clearly observed in runs III-8 and III-9, as depicted in figure 58 and figure 60, respectively. As channel-bank erosion increased, more log–dolos bundles and logs with rootwads located adjacent to the bank began to settle, with the eroding bank affecting the compact interlocking of the ELJ elements at the upstream face. From these runs, the researchers confirmed that, in general, the ELJ units failed to protect the channel bank from erosion under fully submerged flow conditions.


Source: FHWA.

**Figure 59. Photo. Close-up view of some single key dolosse (numbered) used to reinforce the upstream face of the ELJ units for run III-9.**

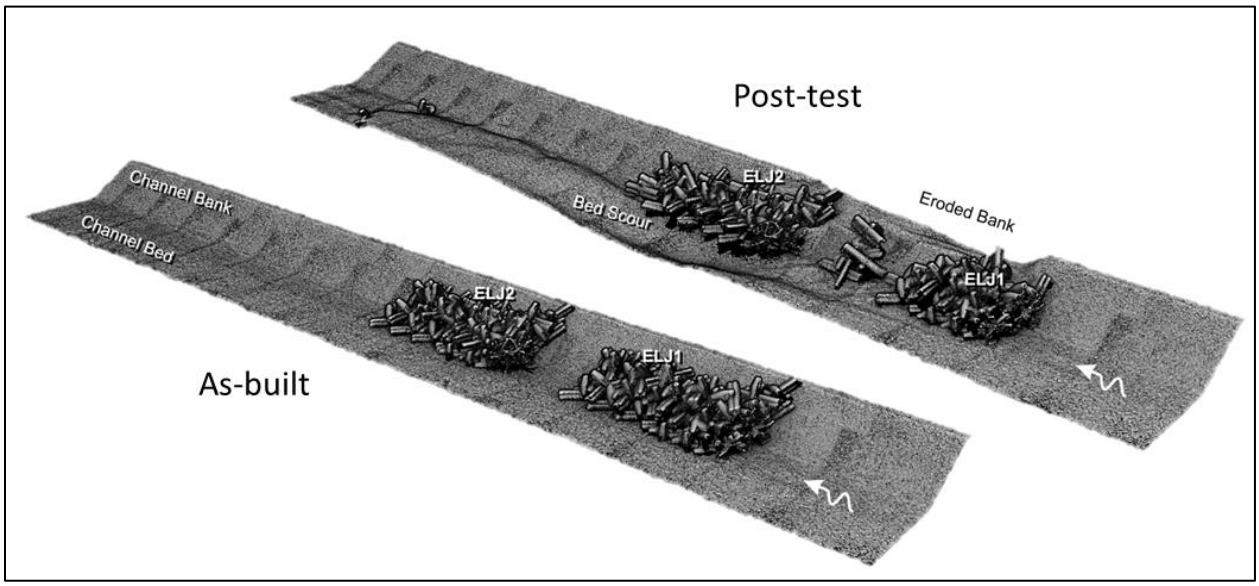


Source: FHWA.

**Figure 60. Graphic. Bathymetric scan results for run III-9 after failure.**

# CHAPTER 4. CFD MODELING

The researchers used CFD modeling to extend the physical flume experiments, enabling a broader analysis of ELJ configurations and performance. CFD modeling was first validated against the flume experiments (phase II) and then extended to the prototype scale of the upper Hoh River. The development of the CFD models followed the general procedure for CFD modeling using STAR-CCM+ and is described in this chapter (CD-adapco 2013).

## VALIDATION OF THE SMALL-SCALE CFD MODEL

The modeling approach consisted of validating the small-scale CFD modeling results with the experimental flume data obtained in phase II, as described in chapter 3. This approach formed the basis for quantifying drag coefficients and hydrodynamic forces acting on ELJ structures.

### Model Geometry

Figure 61 shows a perspective view of the CFD model geometry for a single ELJ unit installed on a half-trapezoidal channel with the same cross-sectional geometry as the one used in the flume experiments (phase II). This geometry was at the same 1:25 model scale as was used in the flume experiments, included the same total number of elements, and had installation layouts similar to the physical ELJ model. Figure 62 shows the same ELJ unit in a cross-sectional view looking downstream.

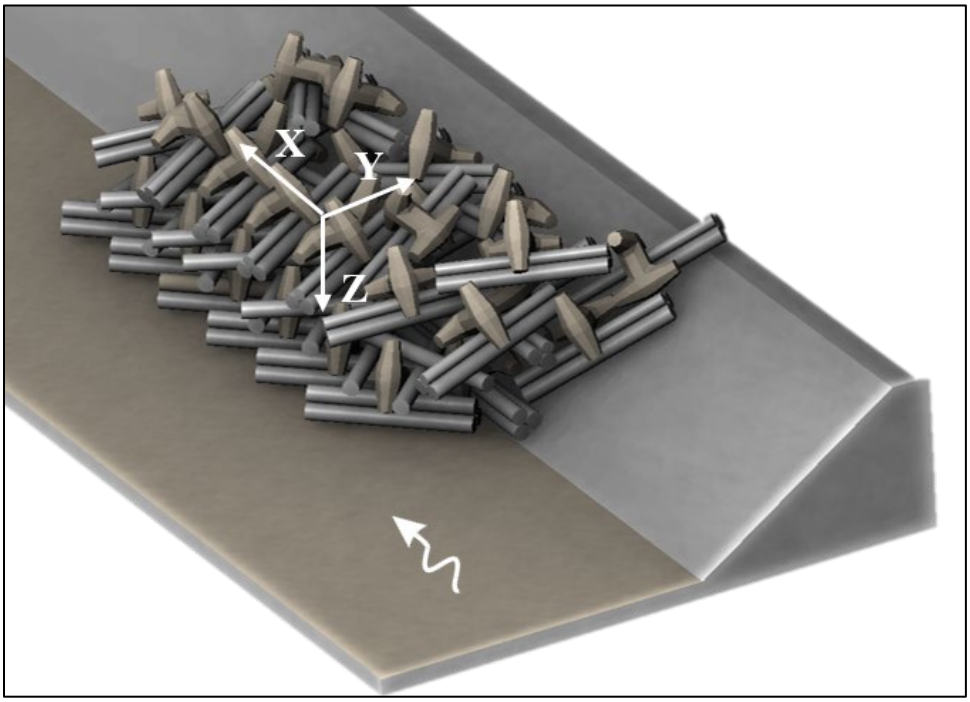


Source: FHWA.

**Figure 61. Graphic. Perspective view of the CFD geometry of an ELJ unit.**

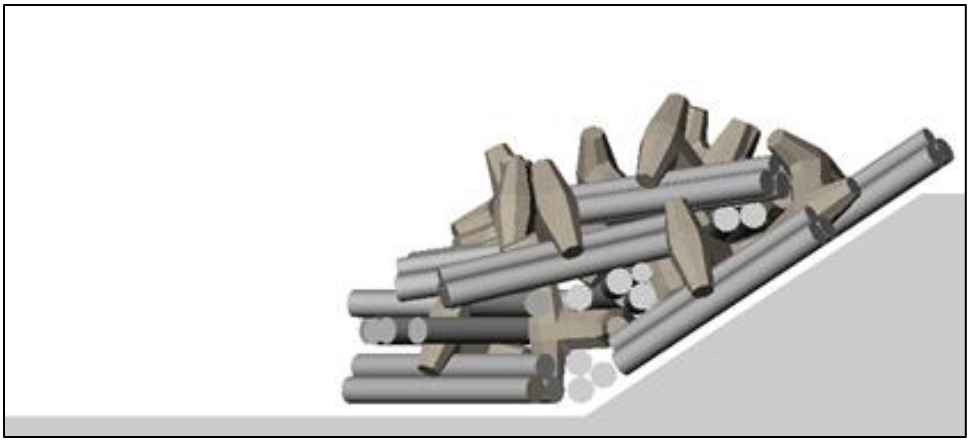

Source: FHWA.

**Figure 62. Graphic. Cross-sectional view of the CFD geometry of an ELJ unit.**

Figure 63 displays the perspective view of a computational mesh derived from the computational trimmer cell mesher, while figure 64 provides a cross-sectional view of the mesh. The mesh had sufficient detail to represent the shapes of the complex elements and random connections within the ELJ structure. The mesh cell sizes varied, with the smallest cell size of 0.5 mm used for the complex ELJ geometry. (Metric units are used in the CFD modeling.)

Using a range of mesh cell sizes allowed for a smooth transition between areas with different mesh cell densities. The mesh cell sizes satisfied the requirements for model geometry and met the need to represent the flow field adequately. The model flow domain for this study used a total of 4.1 million mesh cells.

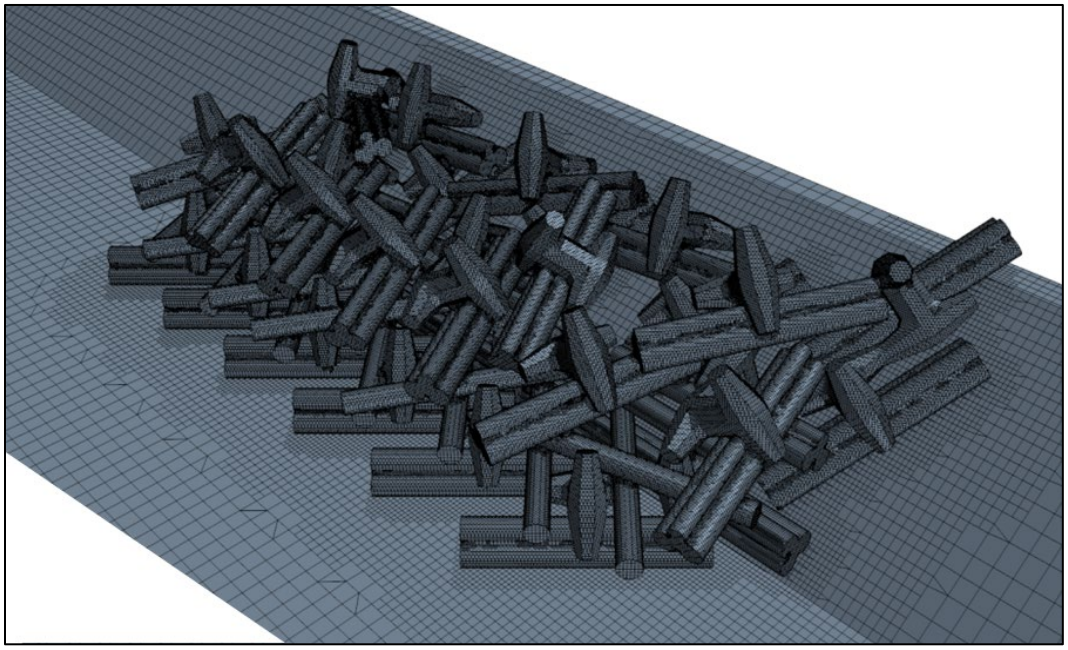

Source: FHWA.

**Figure 63. Graphic. Perspective view of an example mesh used for the CFD model.**

Source: FHWA.

**Figure 64. Graphic. Cross-sectional view of an example mesh used for the CFD model.**

### Physical Continua Models and Boundary Conditions

The volume of fluid (VOF) model was activated to simulate the free surface. Since the focus of the CFD model was to obtain wall shear stress and pressure distributions on the ELJ structure and the water depth was sufficient to eliminate the influence of the motion of the free surface on the bed, the most significant purpose of the VOF model was to simulate open-channel flow accurately. Therefore, a large eddy simulation (LES) approach was used to perform the simulations. The main advantage of this numerical approach is the capability of an LES to capture the dynamics of unsteady, coherent structures in the flow past in-stream obstacles.

In addition to the LES models, the researchers used an unsteady Reynolds-averaged Navier–Stokes (RANS) model in combination with the VOF model and the K-Epsilon turbulence model to simulate the same cases. The two modeling approaches were compared with the experimental data. The wall functions are a set of semiempirical functions used to satisfy the physics of water flow in near-wall regions. They have a close relation with the distribution of wall shear stress. In STAR-CCM+, there are three wall functions: high y+ wall treatment for a coarse mesh, low y+ wall treatment for a fine mesh, and all y+ wall treatment (CD-adapco 2013). The researchers applied the two-layer, all y+ wall treatment to simulate water flow in near-wall regions.

The team validated the CFD simulations of the ELJ model against the physical modeling (phase II). The CFD model boundary conditions were defined based on the flow conditions used for the flume experiments and summarized in table 9. The inlet boundary conditions were defined for the same range of approach flow velocities while the outlet boundary conditions were defined based on the measured flow depths given in that table.

### Modeling Results

Figure 65 displays the CFD modeling results for the velocity field around the single ELJ unit. The two-phase VOF approach provided a realistic simulation of the effect of the ELJ on the flow depths around the structure.

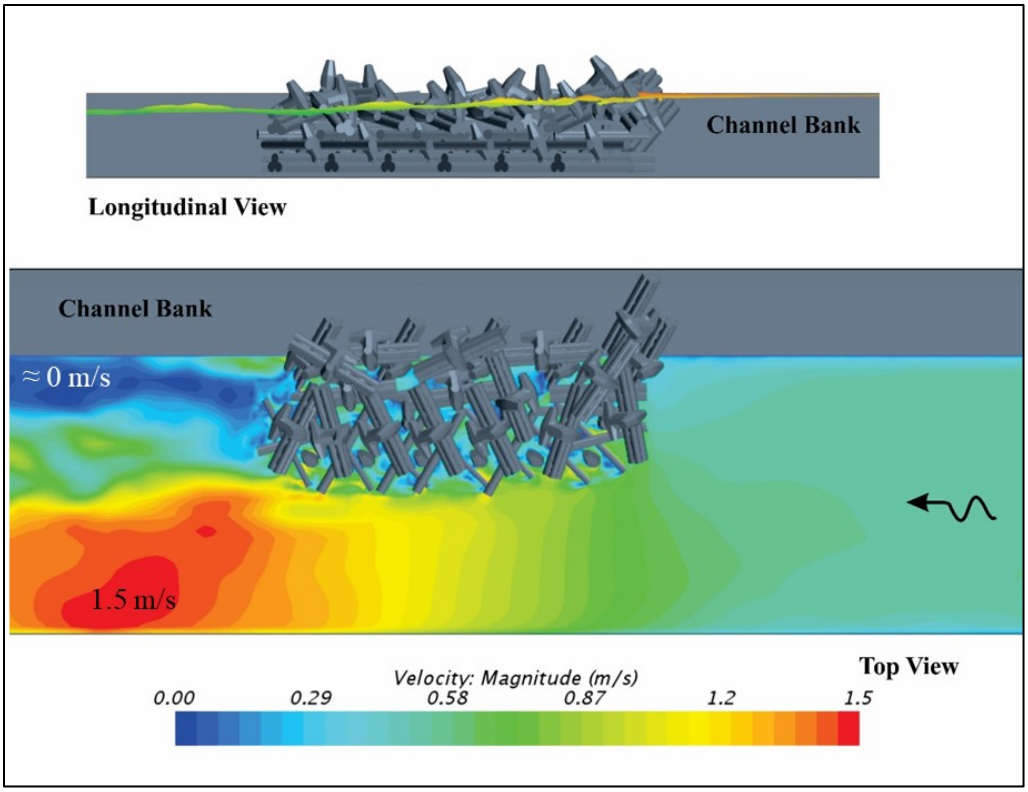


Source: FHWA.

**Figure 65. Graphic. CFD modeling results showing a longitudinal view of the water surface-elevation change (top), and an overhead view of the velocity contour plot (bottom).**

The goals for the CFD models included investigating the complex flow through the ELJs and assessing the effectiveness of ELJs in decelerating the approach flow through ELJ structures. Figure 66 displays CFD simulation results for the four runs (II-1, II-2, II-3, and II-4) showing velocity contour plots of the approach flow for a cross section 2 ft (0.6 m) upstream of the model ELJ unit. The plots confirm increasing velocity with each subsequent run.

Figure 67 displays an example of CFD simulation results for run II-CFD2. It shows velocity contour plots at different cross sections of the model ELJ unit transforming the flow field from the approach conditions. The velocity contour plot at cross section 4 (CS-4) demonstrates the effectiveness of ELJ installations in creating low-flow zones downstream of the ELJ unit near the bank, thereby mitigating the erosive forces acting on the unprotected channel bank. The researchers measured similar results in the flume experiments with erodible bank and bed material, but the CFD modeling provided high-resolution velocity fields adjacent to and through the ELJ units.

The hydrodynamic drag and transverse forces acting on the single model ELJ unit from the CFD modeling are summarized in table 12. The measurements obtained from the physical experiments are included for comparison. Figure 61 displays the directionality of the force components obtained where the drag force is positive in the *x* direction (main flow) and the transverse force is positive in the *y* direction, toward the channel bank.

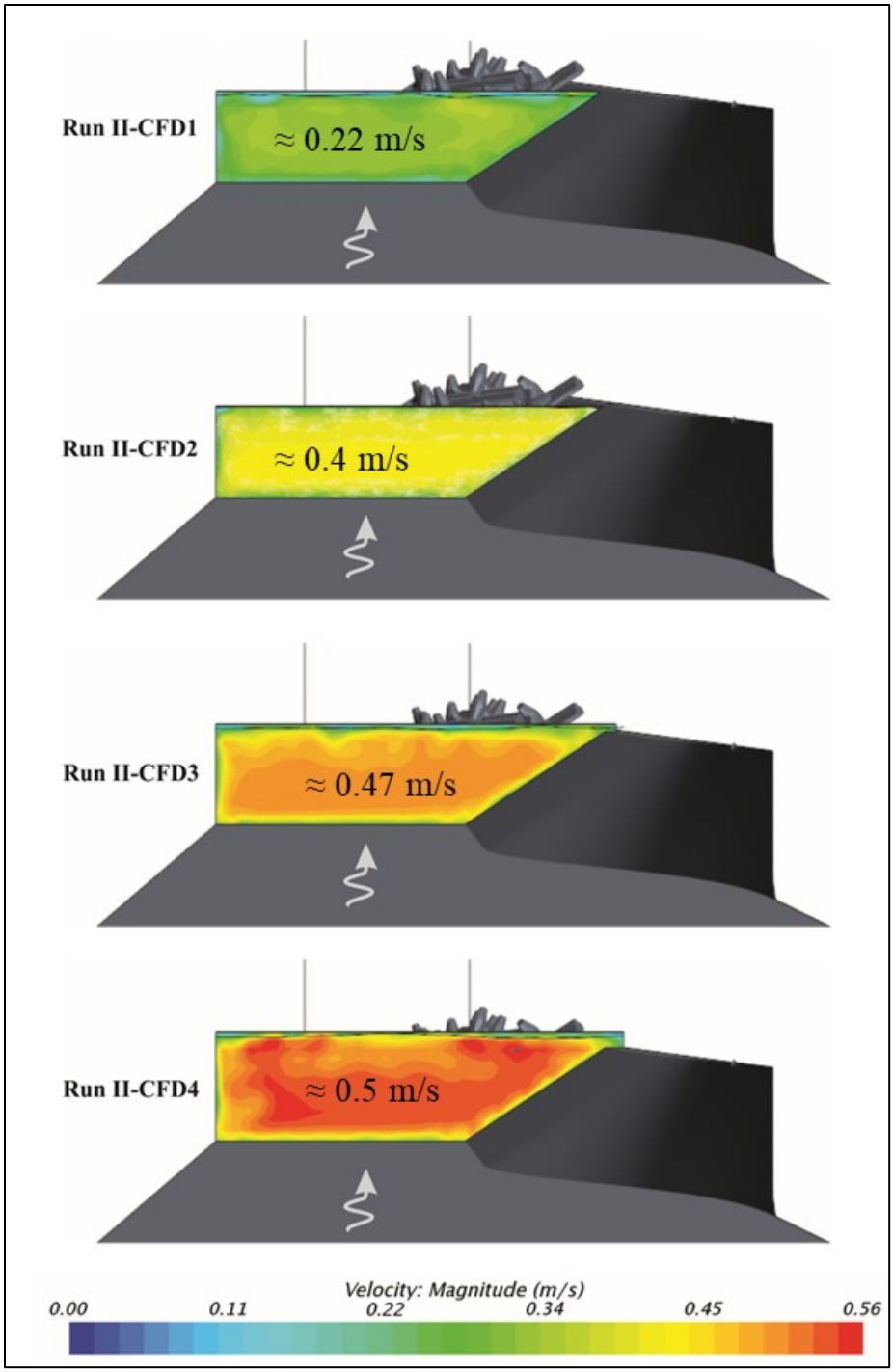


Source: FHWA.

**Figure 66. Graphic. CFD modeling results showing cross-sectional contour plots of the approach velocities (looking downstream) for four runs.**

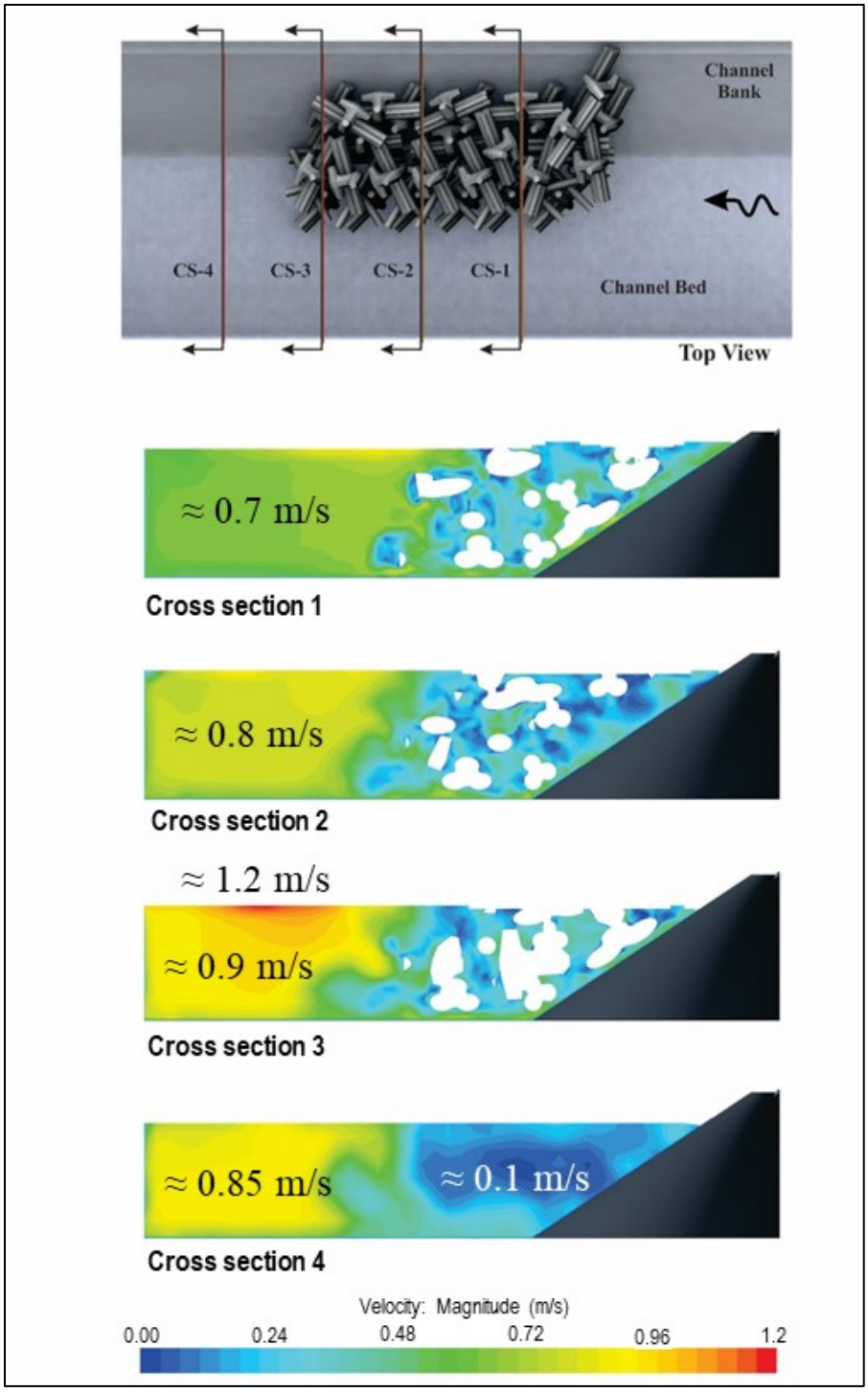


Source: FHWA.

**Figure 67. Graphic. CFD modeling velocity contour plots for run II-CFD2 through the model ELJ unit at several cross sections.**

The $F_D$ results obtained from CFD modeling showed good agreement with the measurements from the flume experiments. The differences ranged from a high of 10 percent for run II-4 to a low of 4 percent for run II-3. Both the physical and CFD modeling confirm that the transverse

forces were very small in comparison to the drag forces when the ELJ was aligned with the flow. On average, $F_T$ was 3.6 percent and 1.9 percent of the drag force for the physical and CFD modeling, respectively. The similarity of the results from both approaches demonstrates that CFD modeling can be applied to estimate hydrodynamic forces acting on complex ELJ structures.

**Table 12. Physical and CFD modeling estimates of the hydrodynamic forces acting on a single ELJ unit (model scale 1:25).**

| | Run Characteristics | | | Physical Modeling | | CFD Modeling | |
|---|---|---|---|---|---|---|---|
| Run | Approach Velocity, $V_U$ (ft/s) | Approach Velocity, $V_U$ (m/s) | Reynolds Number, *Re* | Drag Force, $F_D$ (N) | Transverse Force, $F_T$ (N) | Drag Force, $F_{D\text{-}CFD}$ (N) | Transverse Force, $F_{T\text{-}CFD}$ (N) |
| II-1 | 1.03 | 0.315 | 77175 | 13.24 | 0.42 | 12.56 | 0.07 |
| II-2 | 1.31 | 0.400 | 98000 | 25.44 | −0.91 | 23.69 | −0.12 |
| II-3 | 1.51 | 0.460 | 112700 | 37.97 | −1.32 | 36.63 | −0.16 |
| II-4 | 1.66 | 0.515 | 126175 | 48.52 | −1.82 | 53.47 | −3.33 |

$F_{D\text{-}CFD}$ = computational fluid dynamics modeling drag force; $F_{T\text{-}CFD}$ = computational fluid dynamics modeling transverse force; *Re* = Reynolds number.

## Drag Coefficients for ELJs

The CFD model was calibrated to the physical model runs with the ELJ slightly off the bed and bank, as shown in figure 35. To obtain estimates of $C_D$ over a wider range of conditions, the CFD model was extended to a broader set of hydrodynamic conditions using alternative numerical methods. The extended hydrodynamic conditions and ELJ configurations included simulations with a wider channel to avoid wall effects, higher approach flows, fully submerged ELJ units, and cases with the model ELJ unit seated on the channel bank and bed.

The alternative numerical methods were LES and unsteady RANS models. Figure 68 presents $C_D$ results for an ELJ that is partially submerged with gaps (slightly off the bed and bank), partially submerged without gaps, and fully submerged with gaps. For a given numerical method, the coefficient of drag was consistent over a range of Froude numbers, submergence levels, and with or without gaps. However, the LES method resulted in a higher drag coefficient (approximately 1.75) while the unsteady RANS method resulted in a lower value (approximately 1.4).

The CFD analyses were also extended to determine if ELJ length contributed to the drag force and would, therefore, be a factor in estimating the drag coefficient. Three ELJ unit lengths were modeled: the standard $L_{elj}$, 1.5 times $L_{elj}$, and 2.0 times $L_{elj}$.

All three cases used partially submerged conditions with the same approach velocity ($V_U$ = 2.4 ft/s) and a 7-ft-wide, half-trapezoidal channel to avoid lateral wall effects. The contour plot in figure 69 shows a depth-averaged velocity magnitude for the three cases. Note that, for this range of lengths, the flow separation zone is similar for all three cases.

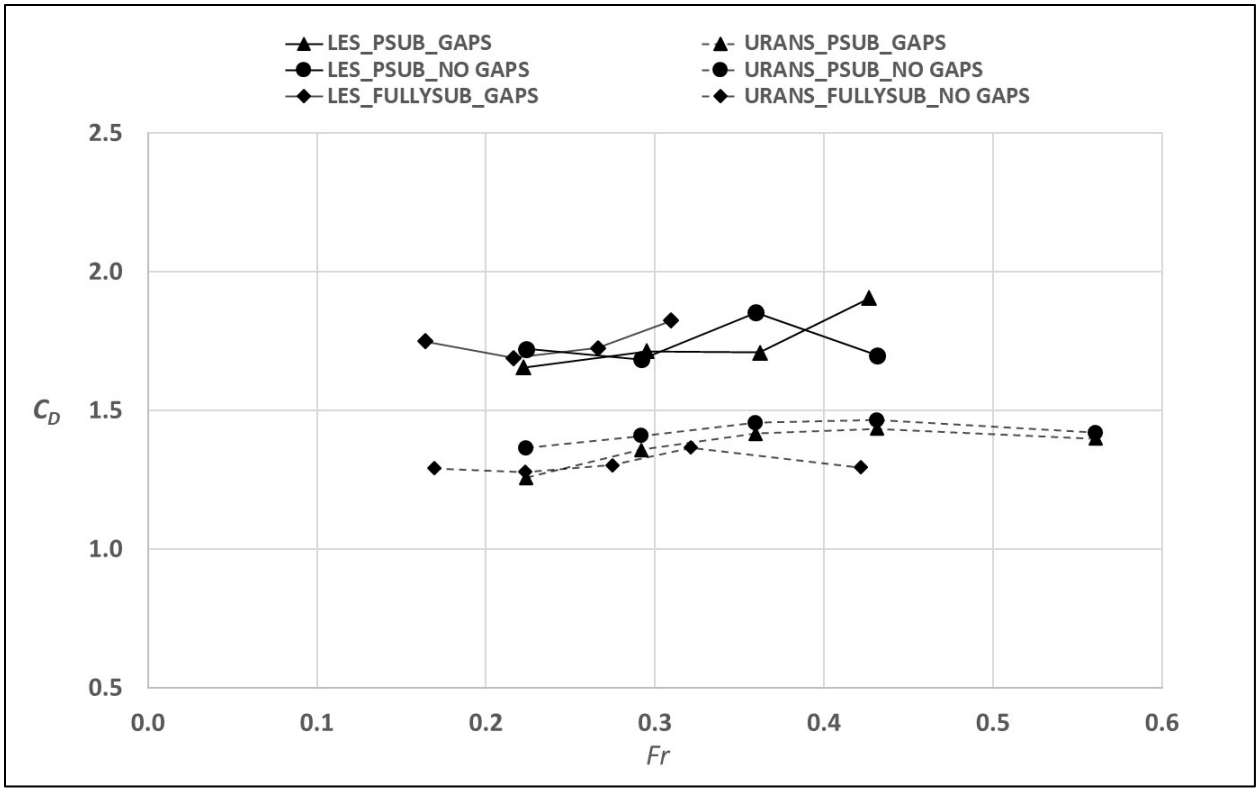


Source: FHWA.

**Figure 68. Graphic. Drag coefficient for a single ELJ unit.**

Figure 70 compares the simulated drag force in dimensionless form for the three cases under the same approach flow velocity and for partially submerged conditions. For the cases of the ELJ units with 1.5 and 2.0 times the standard length, the obtained $F_D$ were 2.5 and 3.1 percent higher, respectively. In addition, figure 69 shows that the velocity of the flow passing through the voids in the ELJ unit rapidly slows after entering. This result suggests that there is an effective length, which is about two-thirds of the standard $L_{elj,}$ that actively slows the flow. Based on these observations, ELJ length is not a significant factor in determining the drag coefficient for ELJ units with lengths greater than the standard $L_{elj}$ of 3.0 ft at the 1:25 model scale or of 75–80 ft at the prototype scale.

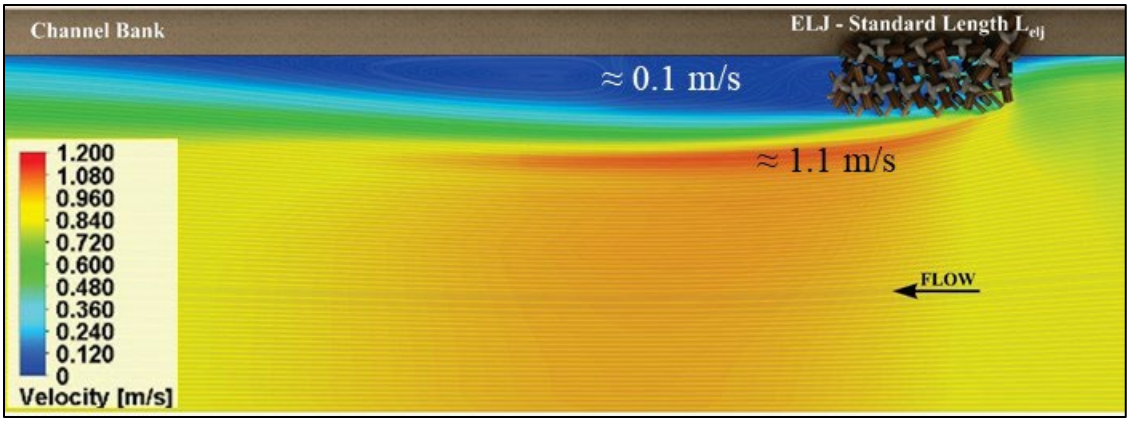


Source: FHWA.

A. ELJ at standard $L_{elj}$.

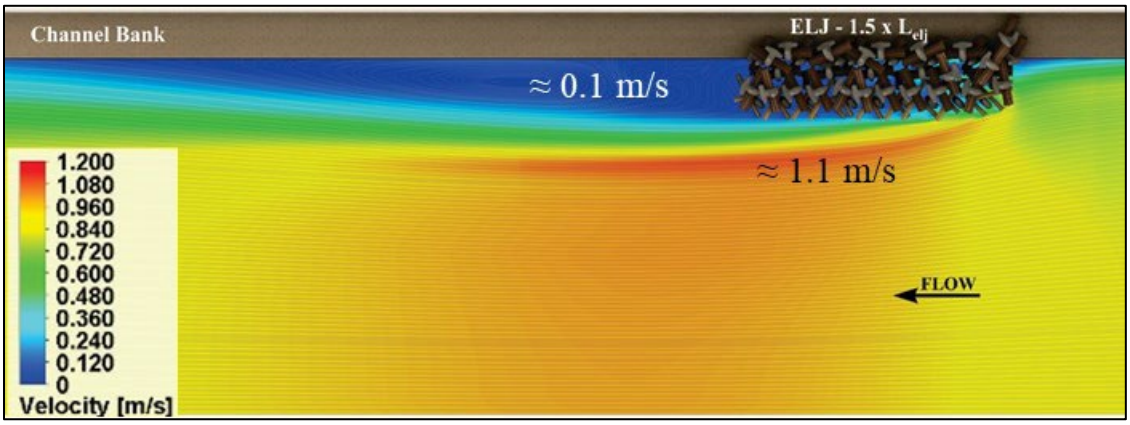


Source: FHWA.

B. ELJ at 1.5 × $L_{elj}$.

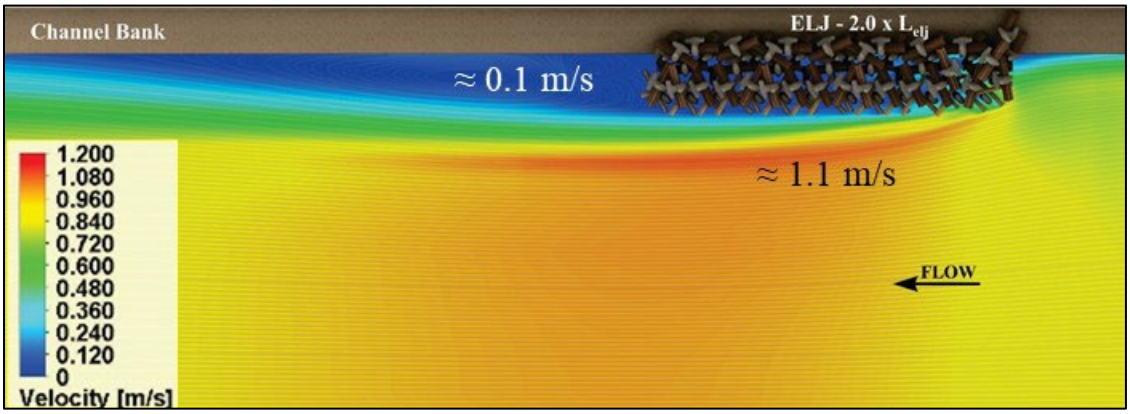


Source: FHWA.

C. ELJ at 2.0 × $L_{elj}$.

**Figure 69. Graphics. CFD modeling results showing depth-averaged velocity for a single ELJ unit with three different lengths.**

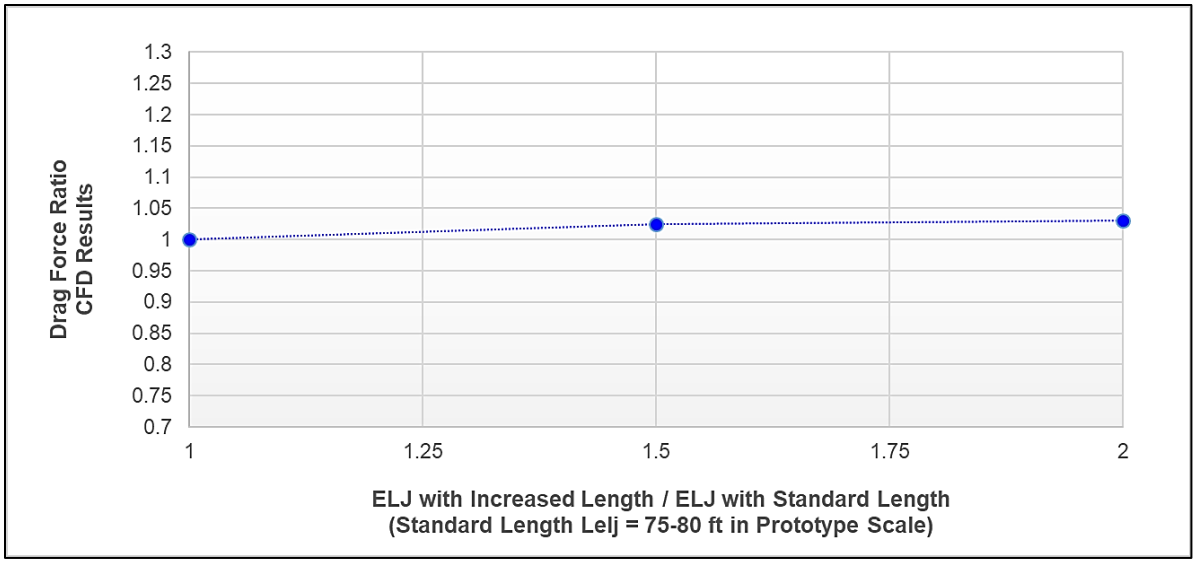


Source: FHWA.

**Figure 70. Graph. Dimensionless drag force with ELJ length.**

## MODELING THE UPPER HOH RIVER PROJECT SITE

The Upper Hoh River project site at MP 4.0 was modeled using CFD to evaluate the performance of ELJs in reducing flow velocities and shear stress along an unstable, eroding bank. The case study illustrates the potential for using CFD modeling to understand complex flows through large ELJ structures and to assess the effectiveness of such structures in controlling bank erosion.

### Domain and Mesh for the MP 4.0 Project Site

The researchers constructed the riverbed geometry model from bathymetric surveys and LIDAR terrain data of the Upper Hoh River project site at MP 4.0 (sites C1 and C2) provided by the WFLHD. The terrain for the existing condition was developed by merging the LIDAR terrain data with the surveyed river cross sections and bathymetric data. The terrain data provided by the WFLHD as .XYZ point-cloud data were numerically enhanced using the Surface-water Modeling System (SMS) (Aquaveo 2020) and CloudCompare software (CloudCompare n.d.) for 3D point-cloud and mesh processing.

Figure 71 shows the terrain data used to generate the CFD domain. The lower elevations indicate the main channel as well as the floodplain at the downstream end of the model. The arrows show the flow direction. Upstream of the site, the active channel width was 400 to 1,200 ft, while downstream the active channel width was 400 to 1,600 ft. At the site, the active channel width was narrower, ranging from 250 to 400 ft.

Sand, gravel, and small boulders comprise the streambed material. The gradation analyses summarized in figure 16 indicates the bed material ranges from sands to 20-inch cobbles with a $D_{50}$ ranging from 3 to 10 inches at MP 4.0 (sites C1 and C2).

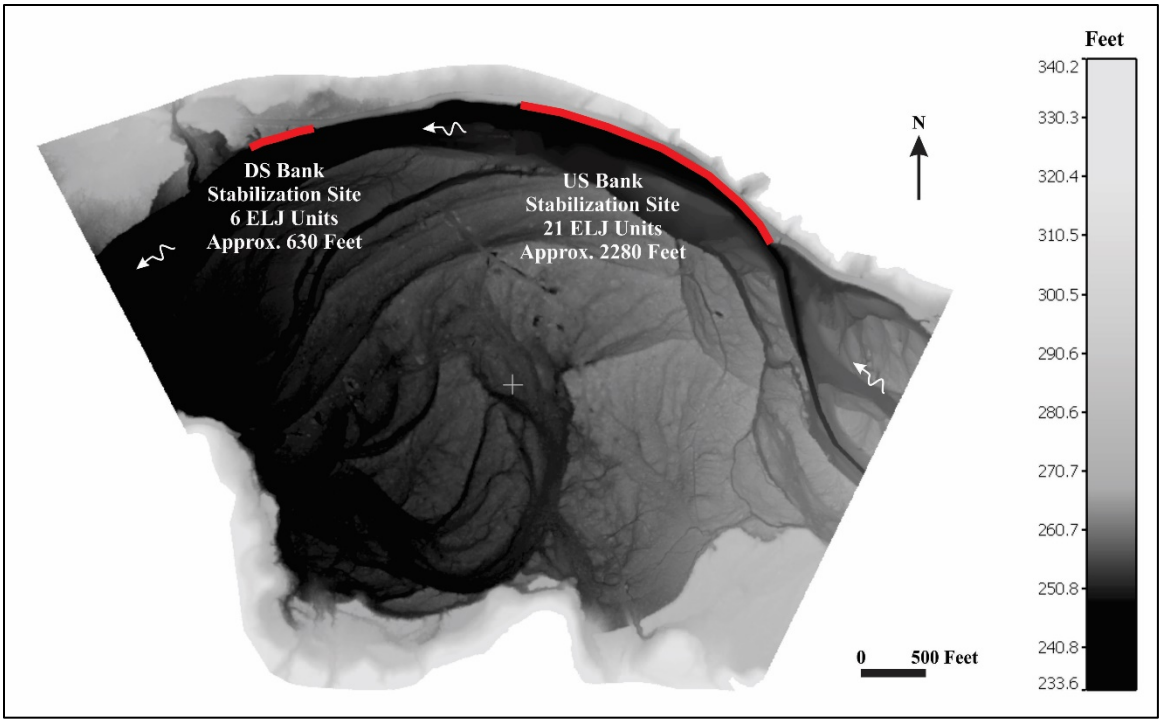


Source: FHWA.
DS = downstream; US = upstream.

**Figure 71. Graphic. Terrain for site MP 4.0 annotated with the location and extent of the ELJs placed for bank stabilization.**

Two model domains were generated for the existing site condition at MP 4.0. The "baseline case" represented the site before installation of ELJs. The second model domain represented the site with 27 ELJ units installed along the right bank. Figure 71 shows the model terrain in grayscale to highlight the location and extent of the ELJ placements along approximately 2,900 ft of unstable, eroding streambank.

Each ELJ unit was 80-ft long, 20-ft wide, and aligned along the bank toe. Within each of the two stabilization sites (downstream and upstream), spacing between the ELJs was approximately 30 ft. Figure 72 provides an example of the flow domain for the upstream bank-stabilization site.

In the CFD model, the bed surface was subdivided into a main channel and a flood plain with roughness coefficients appropriate for these boundaries. The main channel bank and bed, with the floodplain and the ELJ units, were transformed in STAR-CCM+ into a surface mesh by applying the trimmer cell mesher (CD-adapco 2013). A volume mesh was generated with the same type of mesher. In addition, a denser mesh with an average cell size of 6 inches was used for the ELJ units and for the areas surrounding the ELJs and streambank to resolve more accurately the flow field and shear stress distribution on these areas. Figure 73 shows the site geometry transformed into a surface mesh for the main channel bank and bed, including the ELJ units along the bank toe. Figure 74 depicts the generated surface mesh for one of the ELJs. The model used approximately 50 million mesh cells to cover the entire flow domain of the project stabilization site at MP 4.0 in prototype scale.

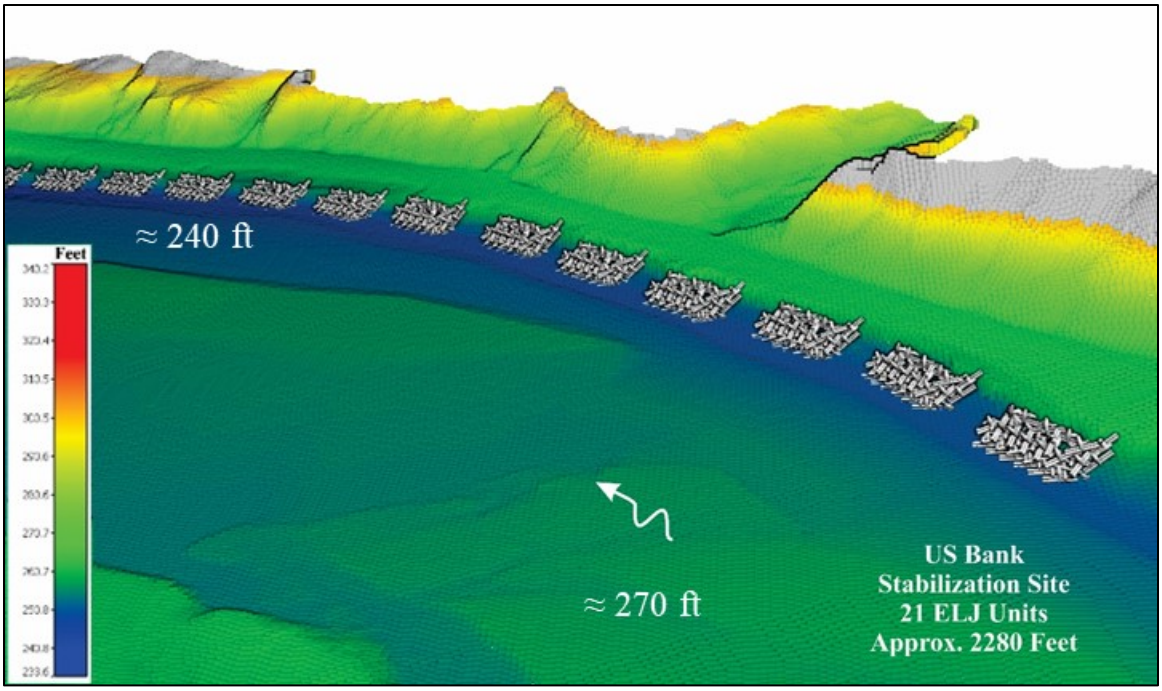


Source: FHWA.
US = upstream.

**Figure 72. Graphic. Detail of the generated flow domain with ELJs along the toe of the streambank at the upstream bank-stabilization site (MP 4.0, site C2).**

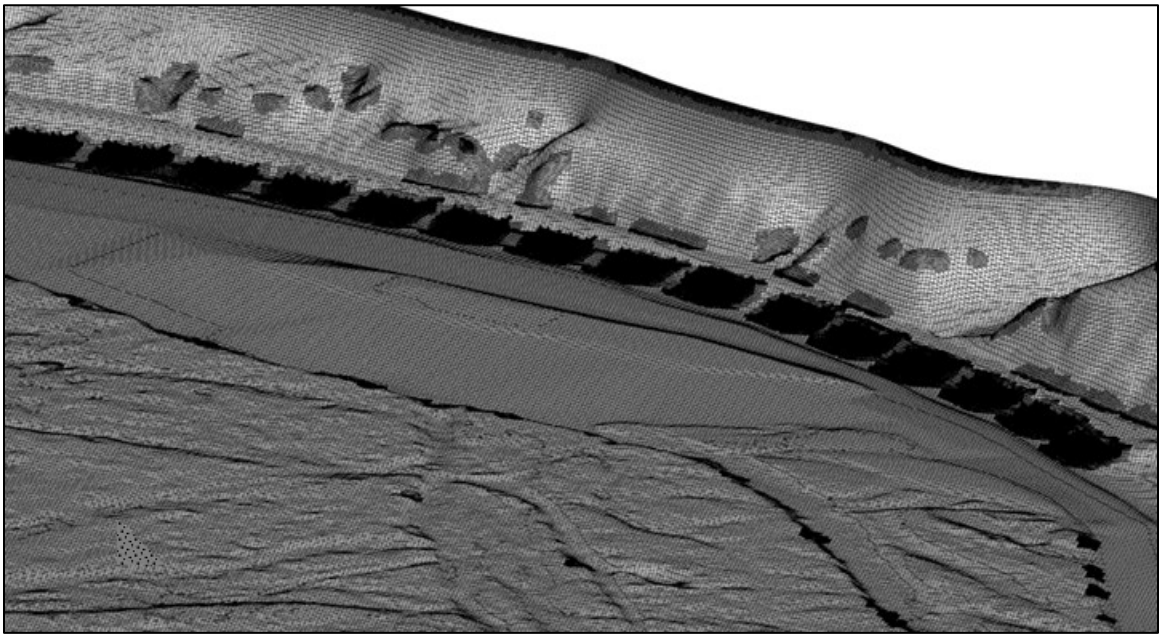

Source: FHWA.

**Figure 73. Graphic. Site geometry transformed into a surface mesh for the main channel bank and bed with ELJs installed along the bank toe.**

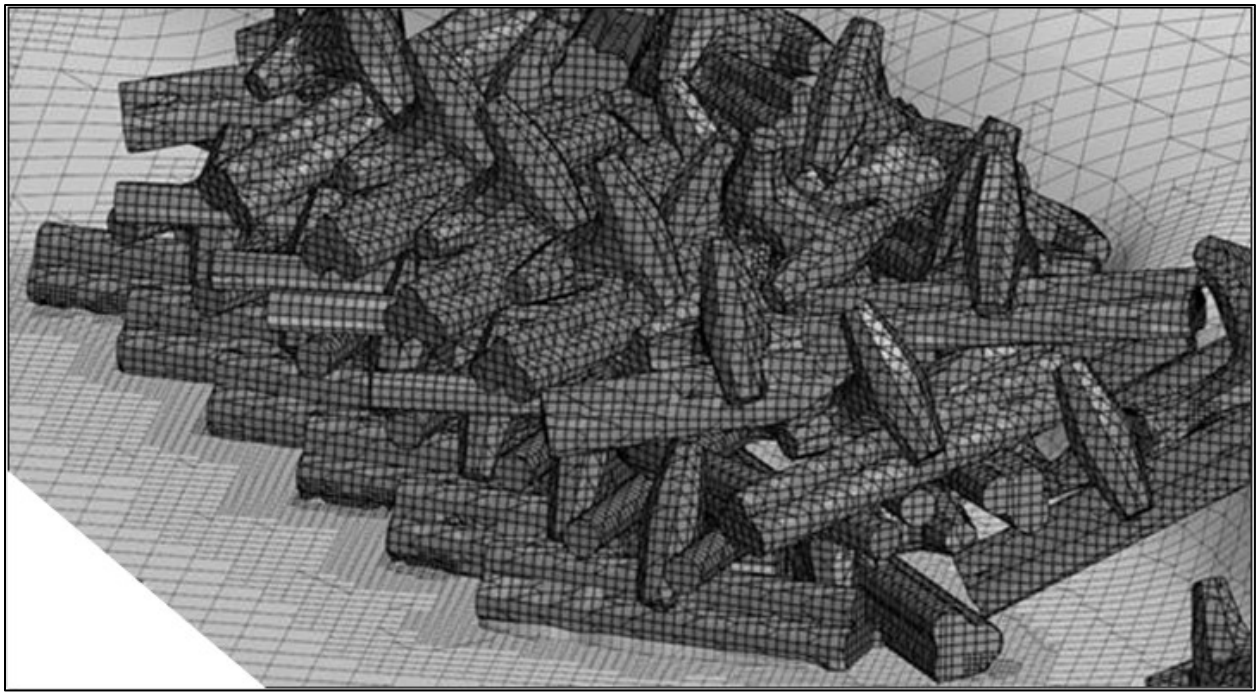

Source: FHWA.

**Figure 74. Graphic. Surface mesh representation of an ELJ unit.**

**Modeling Results at the MP 4.0 Project Site**

The 3D CFD analysis of the existing site conditions without the ELJs (baseline case) was compared with the results of the 2D hydraulic modeling performed by the WFLHD using the U.S. Army Corps of Engineers HEC-RAS 5.0 system. The comparison was based on the 50-yr flood flow conditions with a design discharge (50-yr) of 58,497 $ft^3/s$ and a corresponding flow depth of 15 ft.

For the 2D model, a Manning's roughness coefficient of 0.045 was selected for the main channel and a value of 0.09 was selected for the floodplain areas. Normal flow depth with a 0.01 ft/ft friction slope was set for the downstream boundary condition.

The CFD model required a few attempts to select appropriate roughness coefficients for the bed surface of the main channel and floodplain to correct low-flow velocities obtained in the preliminary models. Adjusting the roughness coefficients of the floodplain surface, which was covered by grass and bushes, required particular attention. The 3D CFD calculations were performed with a time step of 0.1 s. Quasi-steady-state conditions were achieved in about 1,000 s of simulated time.

The water surface elevation results from the 2D and 3D models are compared in figure 75. Estimated water surface elevations are similar for both models. Extracting depth-averaged velocities from the 3D model to compare with depth-averaged 2D model results is not trivial. The results shown in figure 76 show depth-averaged velocities computed in the 2D hydraulic model are slightly higher along the channel bank than the results obtained in 3D CFD.

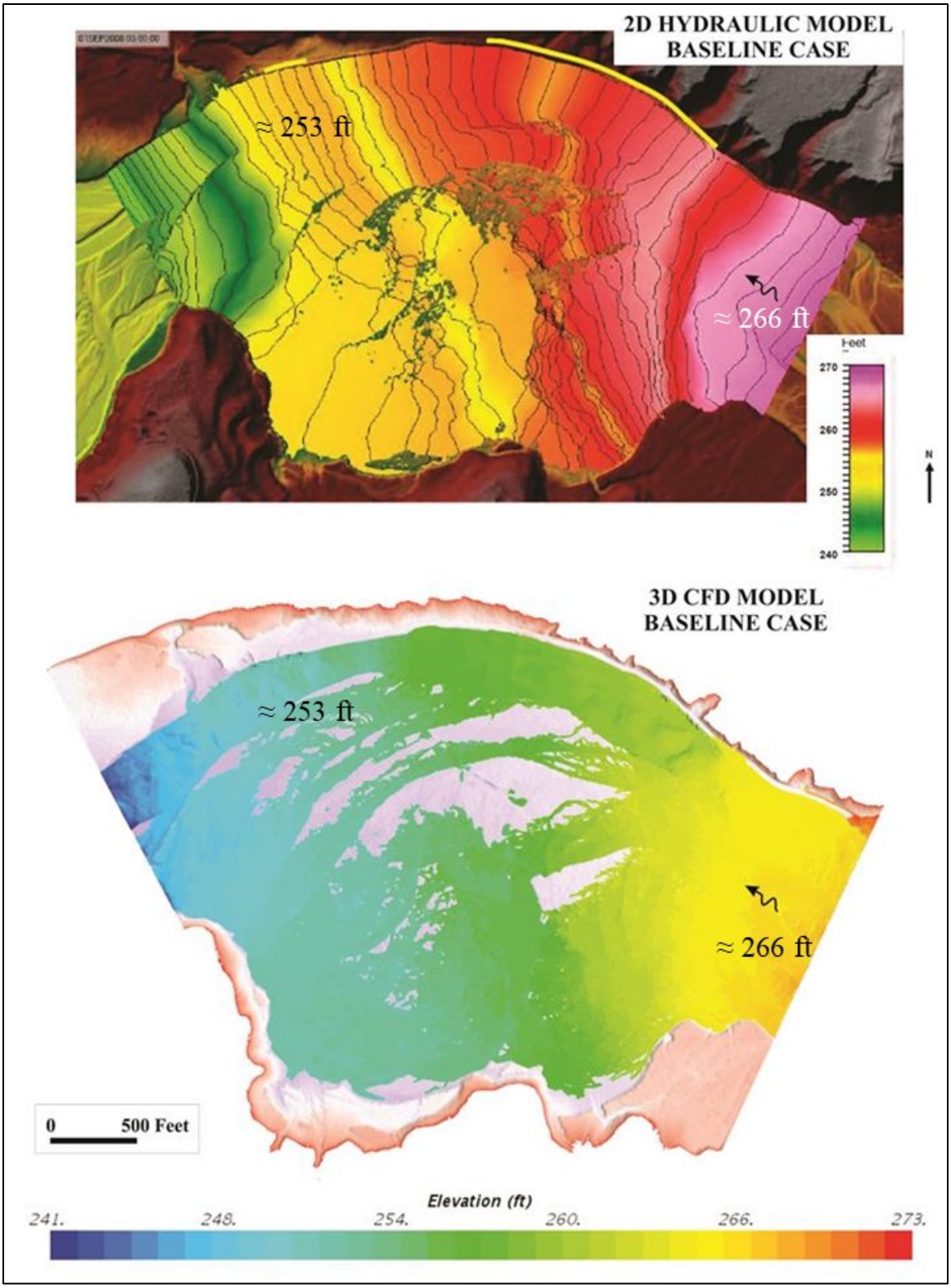


Source: FHWA.

**Figure 75. Graphic. Estimated water surface elevations for the 50-yr flood conditions for 2D and 3D CFD modeling.**

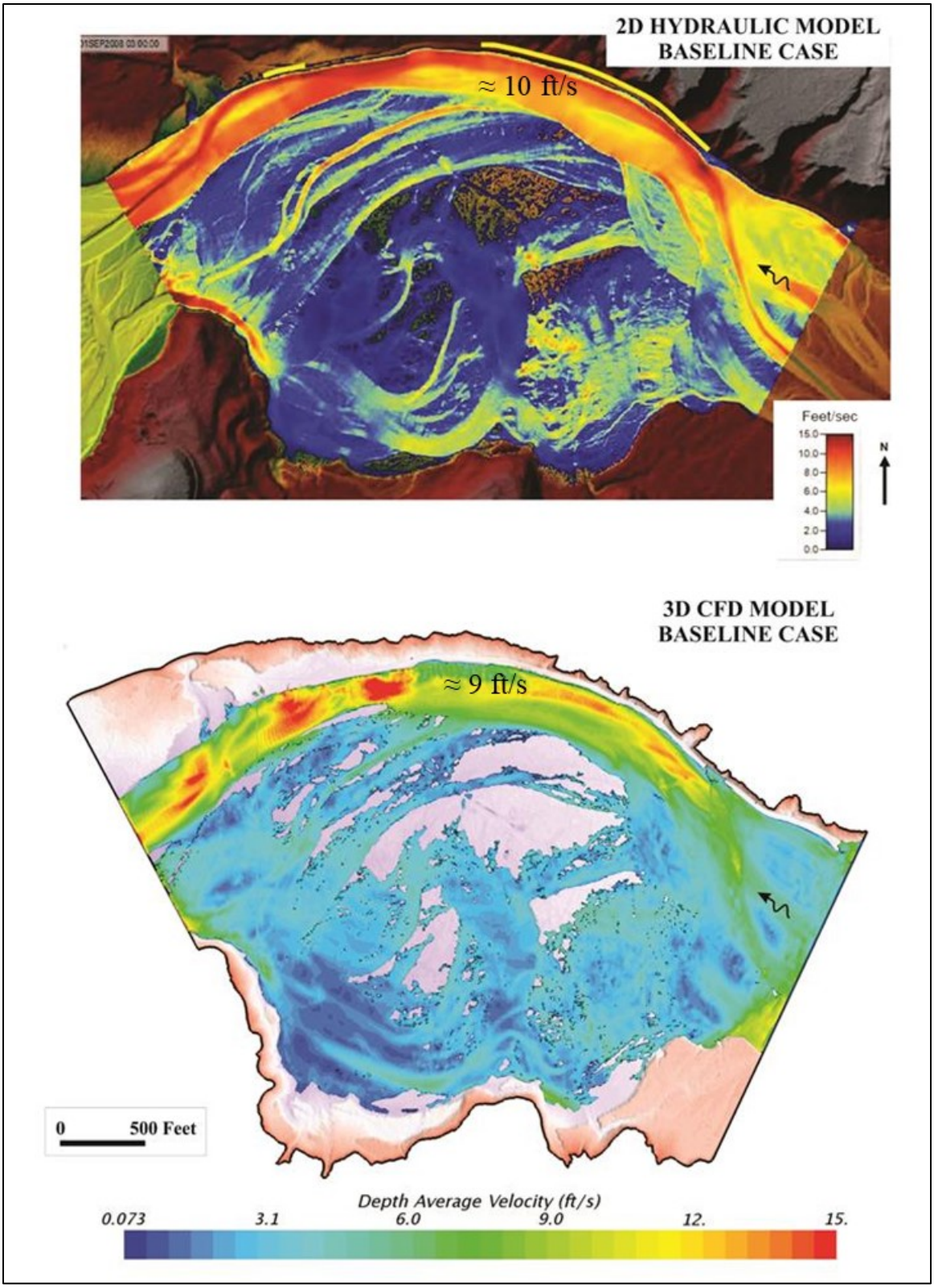


Source: FHWA.

**Figure 76. Graphic. Predicted depth-averaged velocities for the 50-yr flood for 2D and 3D CFD modeling.**

After completing the CFD simulation of the baseline case without ELJs, the next model used the 27 ELJ units along the toe of the channel bank to analyze the performance of these structures by computing the shear-stress distributions on the unstable, eroding stream-bank areas. Figure 77 compares the depth-averaged velocity for 50-yr flood conditions both with and without 27 ELJ units. In the area of units 1 through 21, velocities near the bank were reduced from baseline conditions. However, around ELJ units 22 to 27 both increases and decreases in depth-averaged velocities were observed.

Figure 78 compares CFD-estimated velocity contour plots at two different sections along the upstream bank portion of the Hoh River near ELJ units 3, 4, and 5. The cross section located between ELJ units 3 and 4 demonstrates the effectiveness of the ELJ installation in creating low flow zones in the 30-ft gaps between ELJ units. The cross section located at the longitudinal centerline of ELJ unit 4 shows how high velocities shown in the baseline case are shifted into the main channel with the ELJ installation.

Similarly, figure 79 compares CFD-estimated velocity contour plots orthogonal to the downstream bank portion of the Hoh River at the location of ELJ units 22 through 25. The cross section located between ELJ units 22 and 23 demonstrates the effectiveness of the ELJ installation in creating low-flow zones in the 30-ft gaps between the units.

The researchers also examined shear stresses between the baseline condition without ELJ and with ELJ units in place. Figure 80 shows a portion of the Hoh River where installation of ELJ units 15, 16, and 17 were anticipated to protect the unstable bank. Figure 81 and figure 82 show the CFD-estimated shear stress distribution for the baseline case and the ELJ case, respectively. In the baseline case, higher flow velocities and secondary flow near the bank resulted in shear stresses of up to 3 $lb/ft^2$. With the installation of the ELJ units, however, the CFD modeling showed reduced shear stress on the bank, with magnitudes near 0 to 0.6 $lb/ft^2$.

The 3D CFD modeling of the with ELJ scenario showed that Upper Hoh River Road would be overtopped by approximately 1.5 to 2 ft under 50-yr flood conditions, as shown in figure 83. The inundation would occur near road station 53+50, at the upstream end of the bank stabilization site. However, the ELJ units would not cause the overtopping; overtopping would also occur in this area under baseline conditions. The 2D modeling confirms overtopping of the roadway at this location.

As was shown in figure 82, the ELJ units were typically effective at reducing shear stresses at the bank for the 50-yr flood conditions. However, at the upstream extent of the installation near road station 53+50, the effectiveness is not as clear. Figure 84 shows relatively high stresses at the bank adjacent to road station 53+50. In figure 85, the high stresses at that location remained in the with ELJ scenario. In chapter 3, the flume experiments for similar flow conditions (fully submerged ELJ units) also indicated that channel-bank erosion would be observed because of the highly turbulent flow above and between the bank and ELJ units. Therefore, additional treatment or countermeasures, such as riprap revetment or ballast on this section of the road, are recommended to prevent bank erosion resulting from road overtopping and full submergence of the ELJ units.

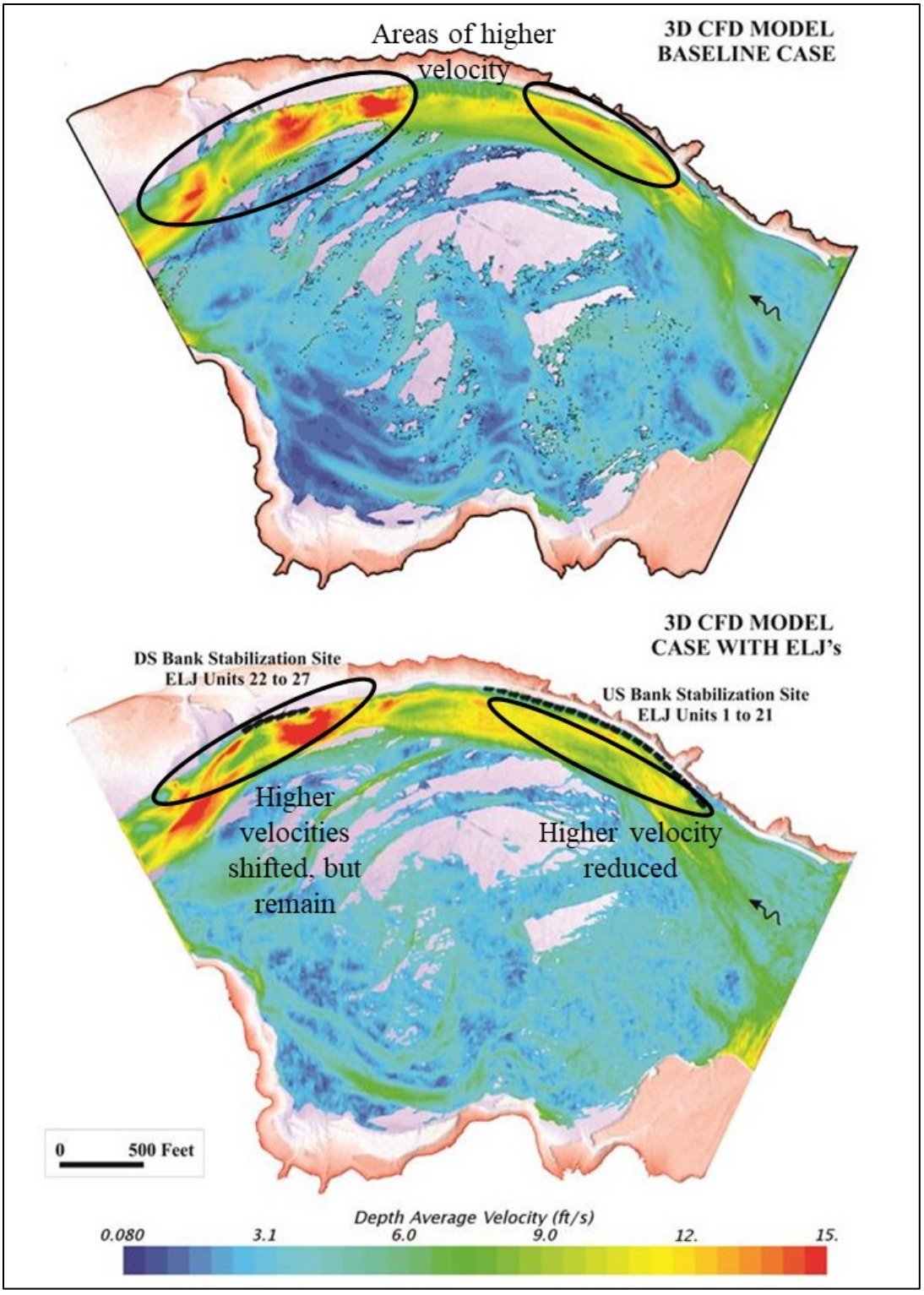


Source: FHWA.
DS = downstream; US = upstream.

**Figure 77. Graphic. CFD modeling comparison of baseline (top) and ELJ (bottom) conditions of the estimated depth-averaged velocities for the 50-yr flood.**

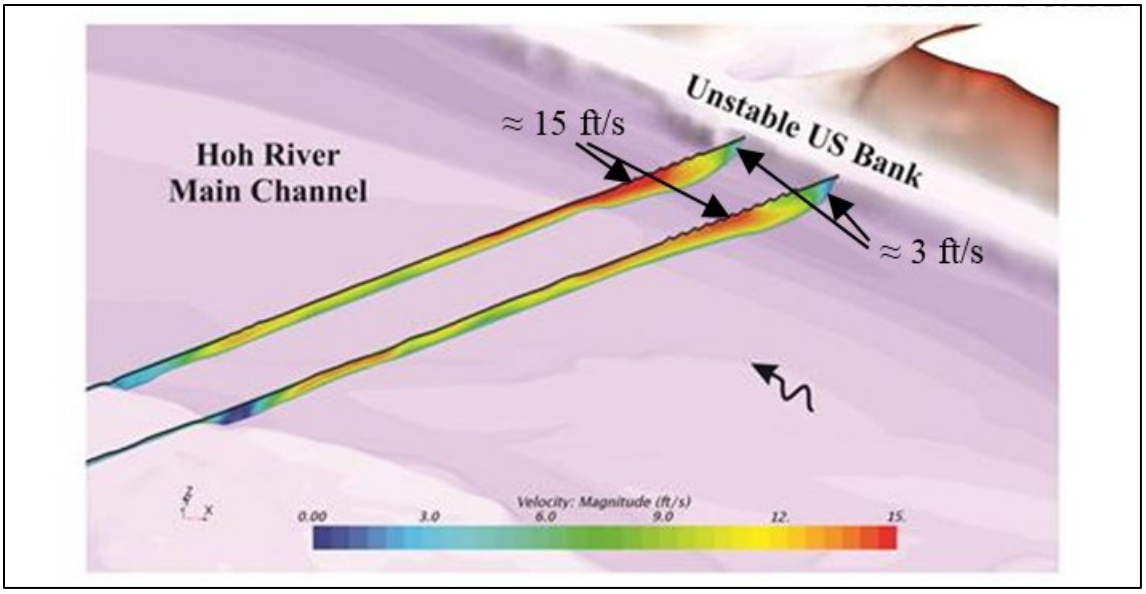


Source: FHWA.
US = upstream.
Note: The solid line on the cross section represents the water surface.

A. 3D CFD model baseline case.

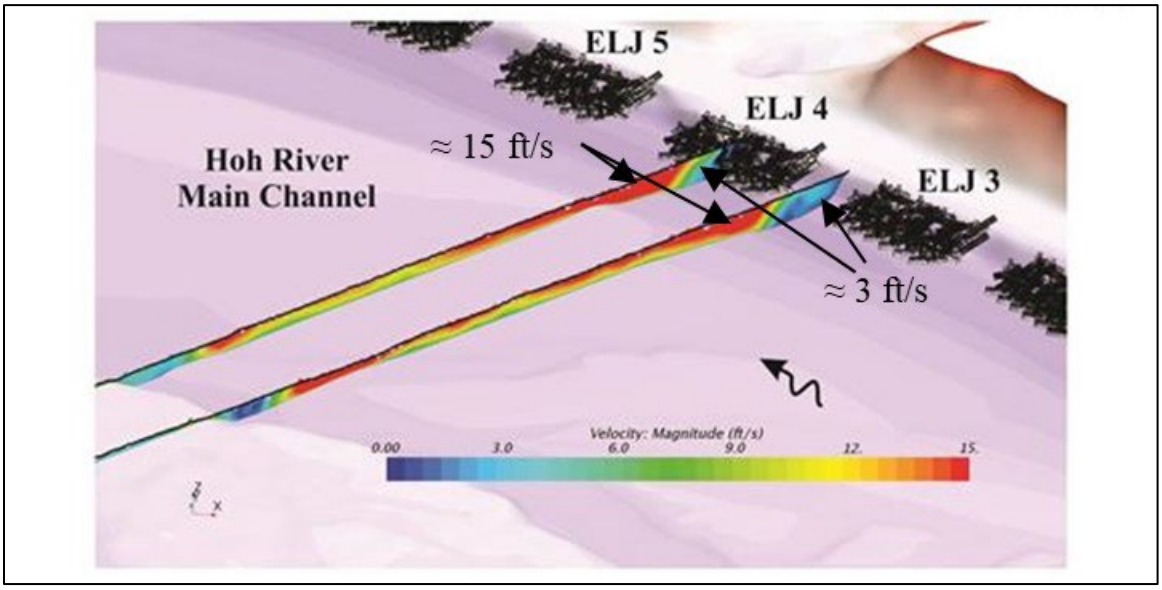


Source: FHWA.
Note: The solid line on the cross section represents the water surface.

B. 3D CFD model case with ELJs.

**Figure 78. Graphics. Comparison of velocity conditions at baseline and with ELJs at ELJs 3–5.**

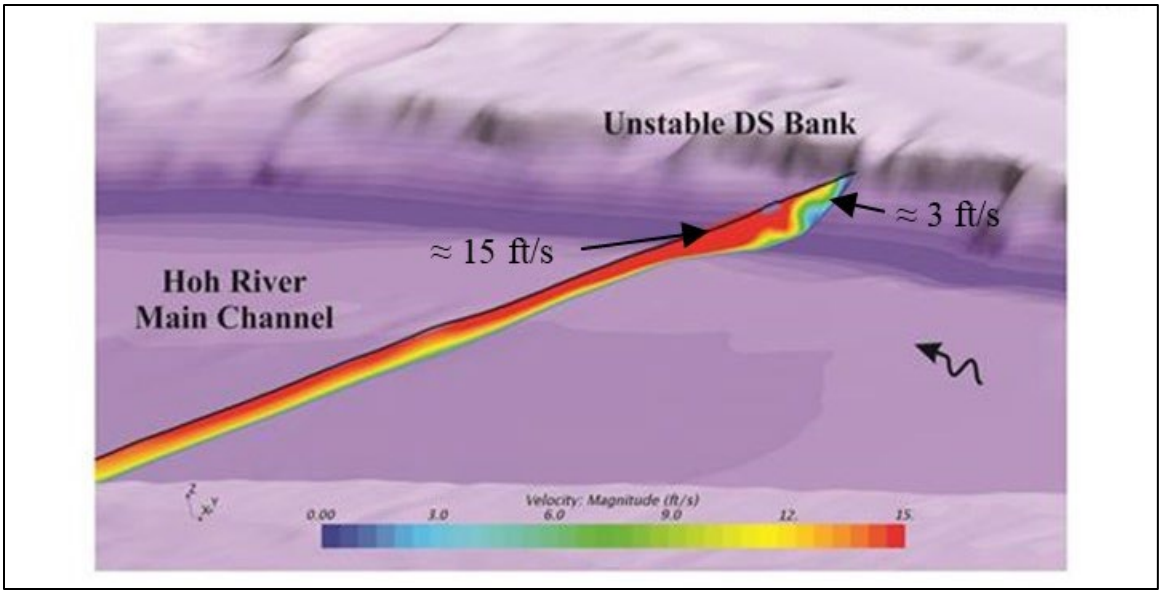


Source: FHWA.
DS = downstream.
Note: The solid line on the cross section represents the water surface.

A. 3D CFD model baseline case.

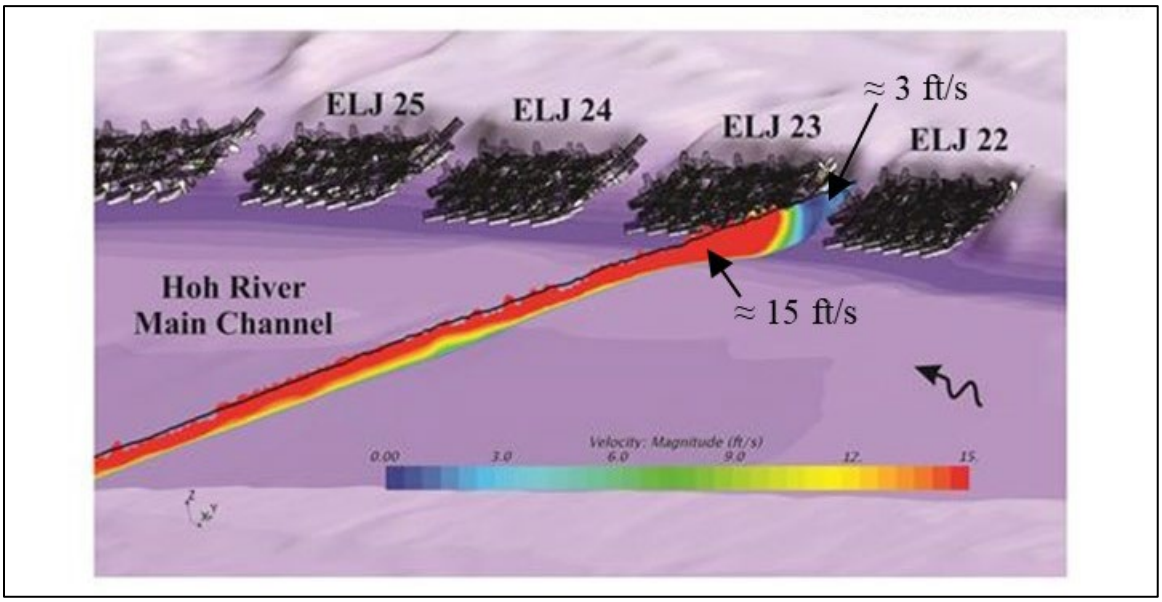


Source: FHWA.
Note: The solid line on the cross section represents the water surface.

B. 3D CFD model case with ELJs.

**Figure 79. Graphics. Comparison of velocity conditions at baseline and with ELJs at ELJs 22–25.**

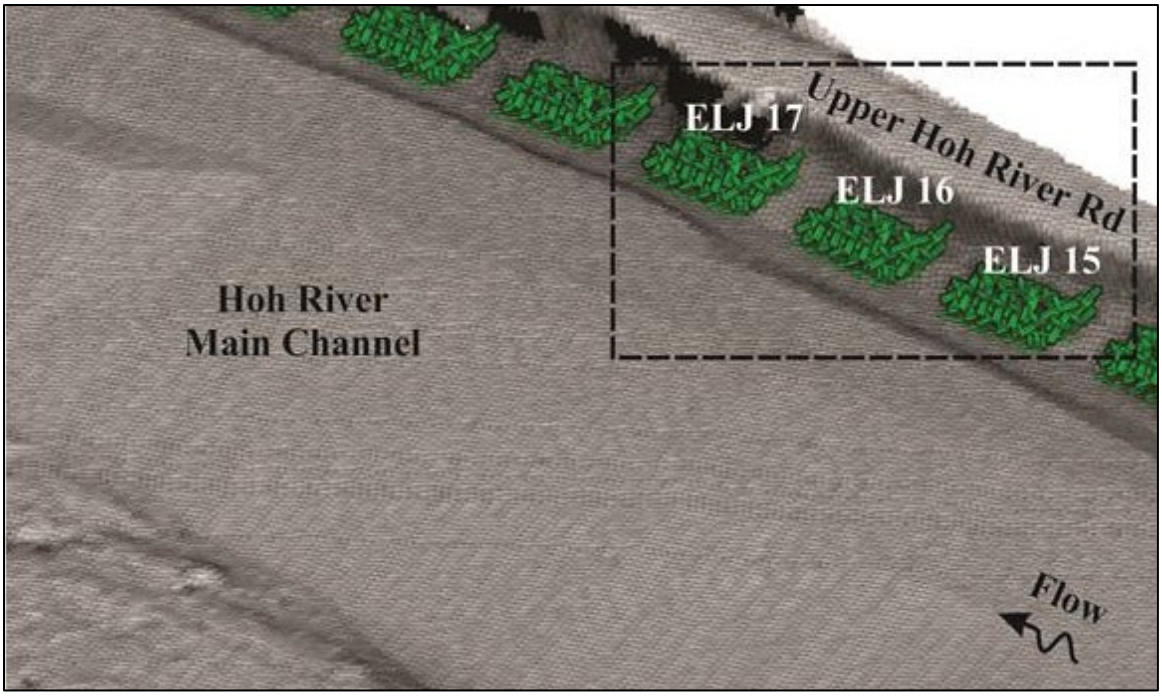


Source: FHWA.

**Figure 80. Graphic. Location in the Hoh River channel showing representation of selected installation of ELJ units 15, 16, and 17.**

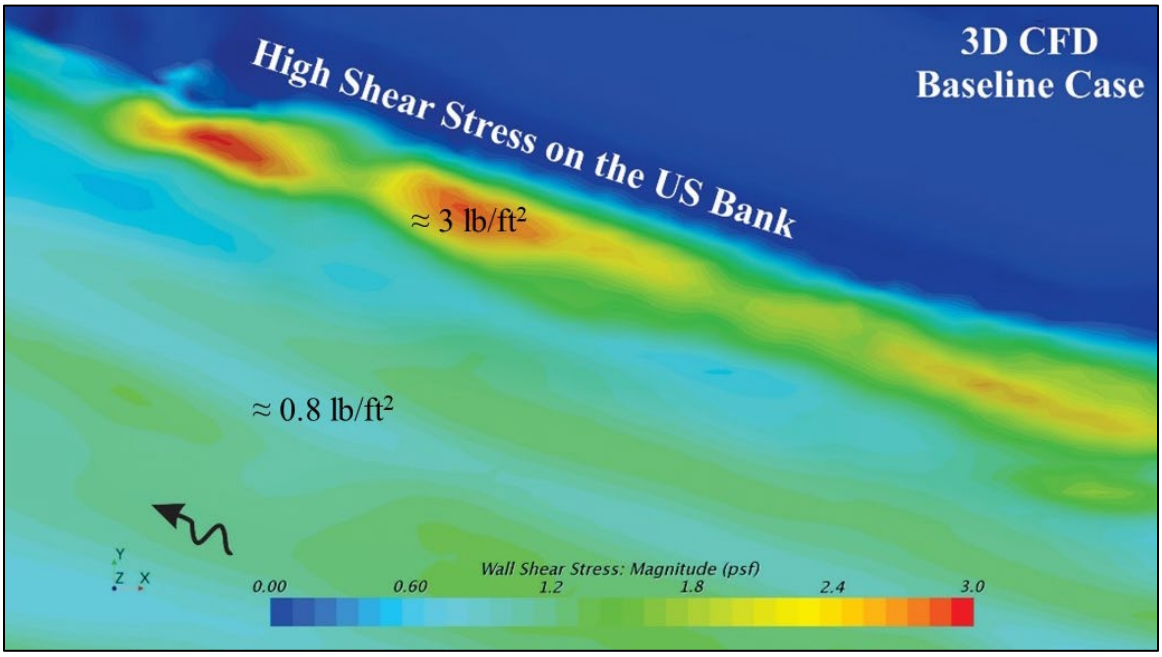


Source: FHWA.

**Figure 81. Graphic. Simulation of the shear stress distribution in the baseline case (without ELJ units) where ELJ units 15–17 would be placed.**

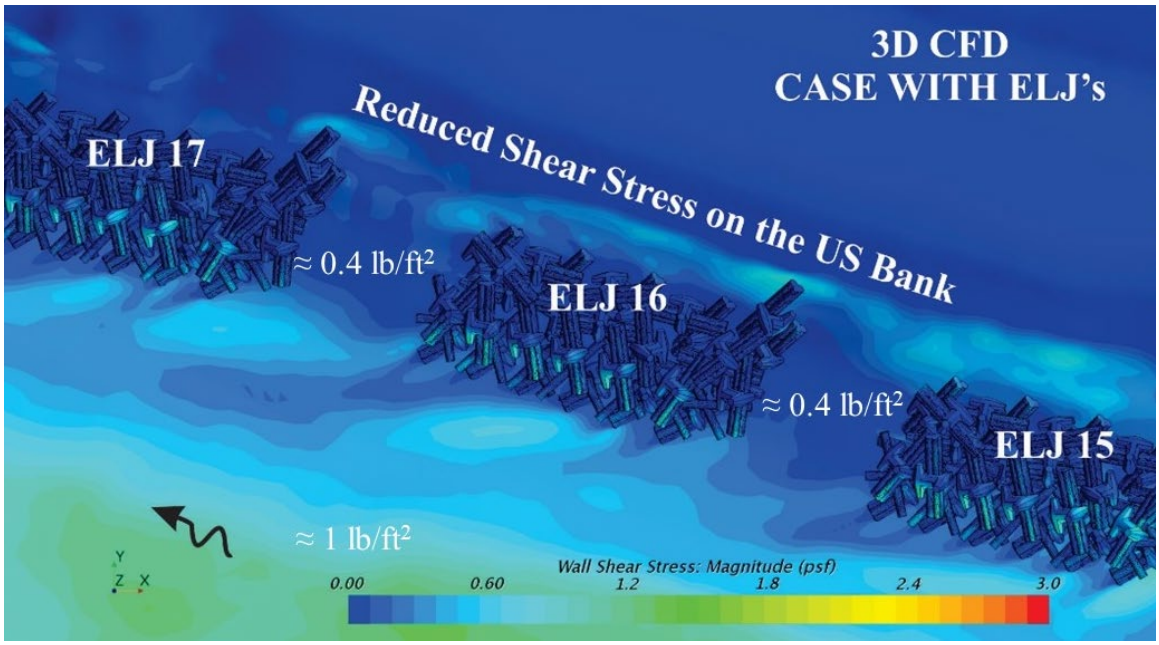


Source: FHWA.
US = upstream.

**Figure 82. Graphic. Simulation of the shear stress distribution in the case with ELJ units 15–17.**

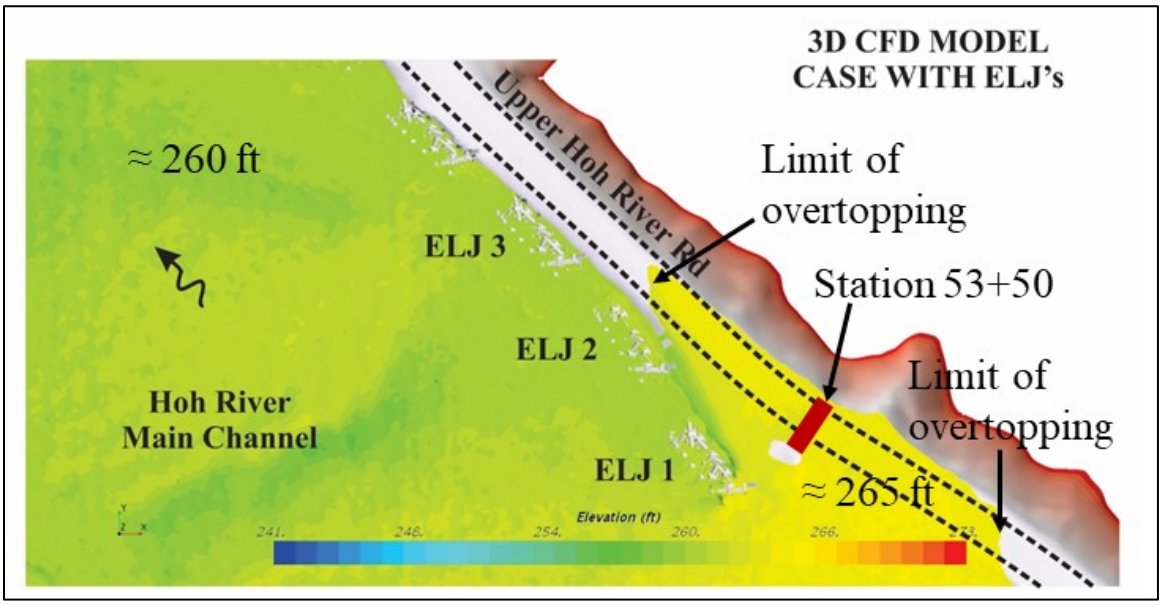


Source: FHWA.

**Figure 83. Graphic. CFD-estimated water surface elevation with ELJs showing road overtopping near road station 53+50.**

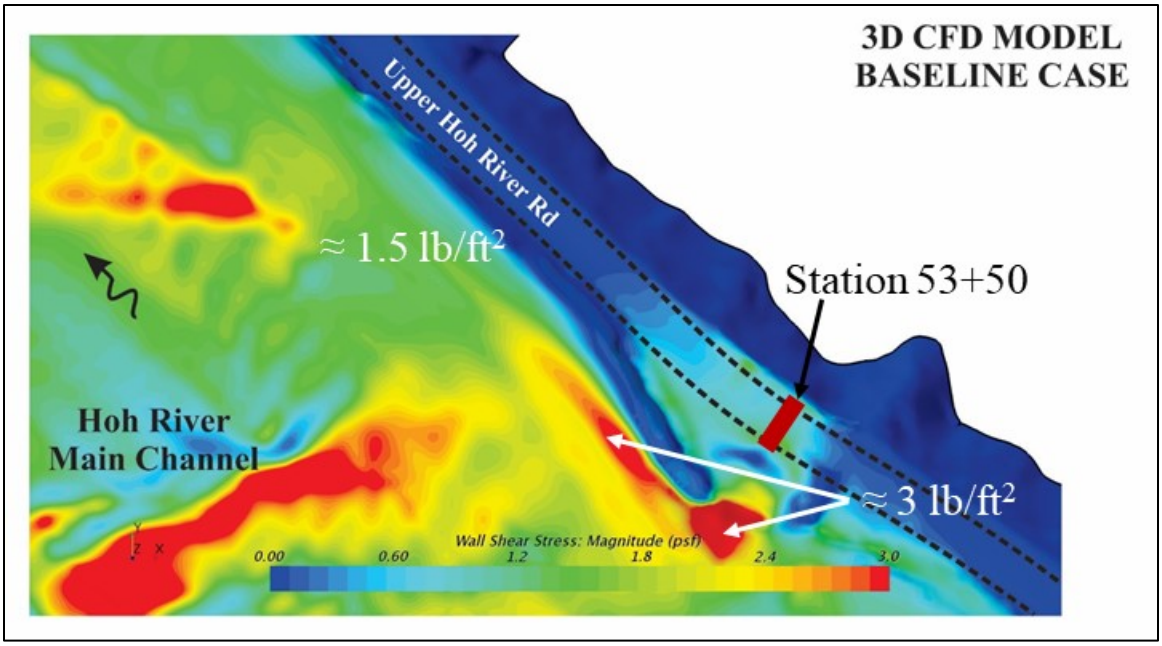


Source: FHWA.

**Figure 84. Graphic. Simulation of the shear stress distribution near road station 53+50 for the baseline case under 50-yr flood conditions.**

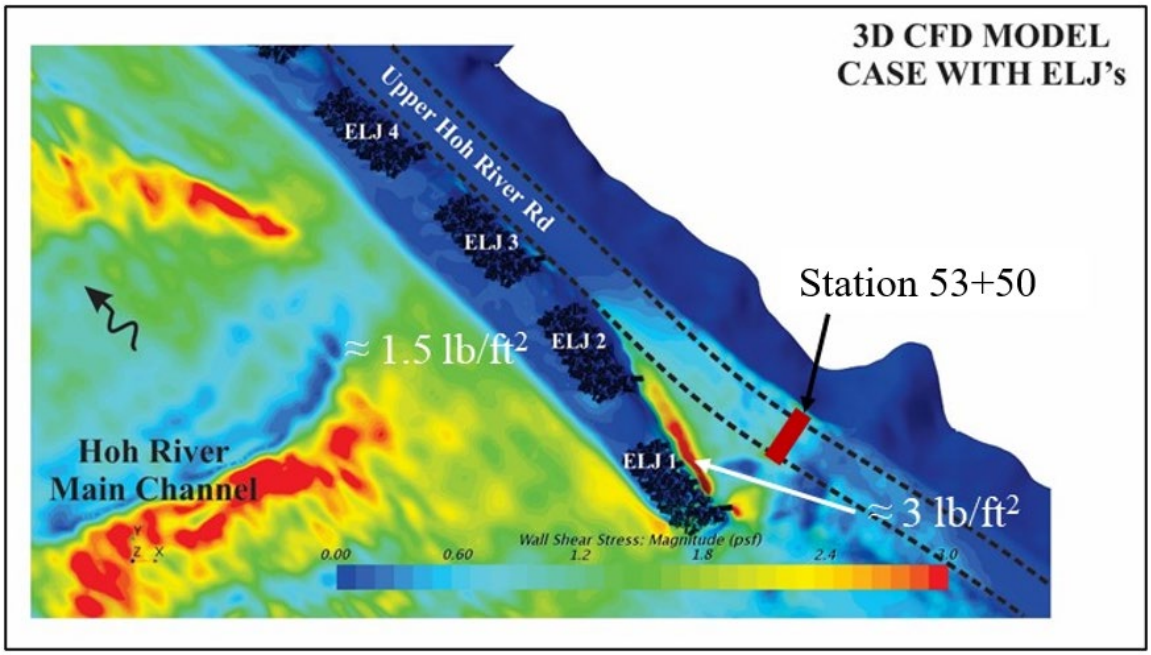


Source: FHWA.

**Figure 85. Graphic. Simulation of the shear stress distribution near road station 53+50 for the ELJ case under 50-yr flood conditions.**

# CHAPTER 5. RESULTS AND DESIGN RECOMMENDATIONS

## HYDRAULIC STABILITY ANALYTICAL MODEL DEVELOPMENT

The development of a theoretical model to assess the hydraulic stability of a single ELJ structure is described in this section. The researchers developed an analytical approach based on the drag coefficient for ELJs derived from physical and numerical modeling. They also applied additional experiments to define friction coefficients for model ELJs seated on an erodible channel bed to develop the stability model. Parts of the stability experiments described in chapter 3 were used to validate the hydraulic stability model described here.

Figure 86 displays a force balance schematic for a partially submerged ELJ unit. The proposed stability model relies on good interlocking of the ELJ elements so that the ELJ unit can be considered a rigid body. The forces considered included the following:

- Buoyancy corrected weight ($m_T g - F_B$), where $m_T$ is the total ELJ mass, $g$ is gravitational acceleration, and $F_B$ is the buoyancy of the submerged portion of the ELJ.
- Drag force ($F_D$) on the ELJ from the water flow. (Flow induced lift and transverse forces are ignored because their values were small in the flume experiments.)
- Resisting force ($F_{fs}$) with the channel bed defined as the resisting friction force. (The channel bank is not considered to simplify the analysis. This assumption is a conservative assumption for the analysis.)

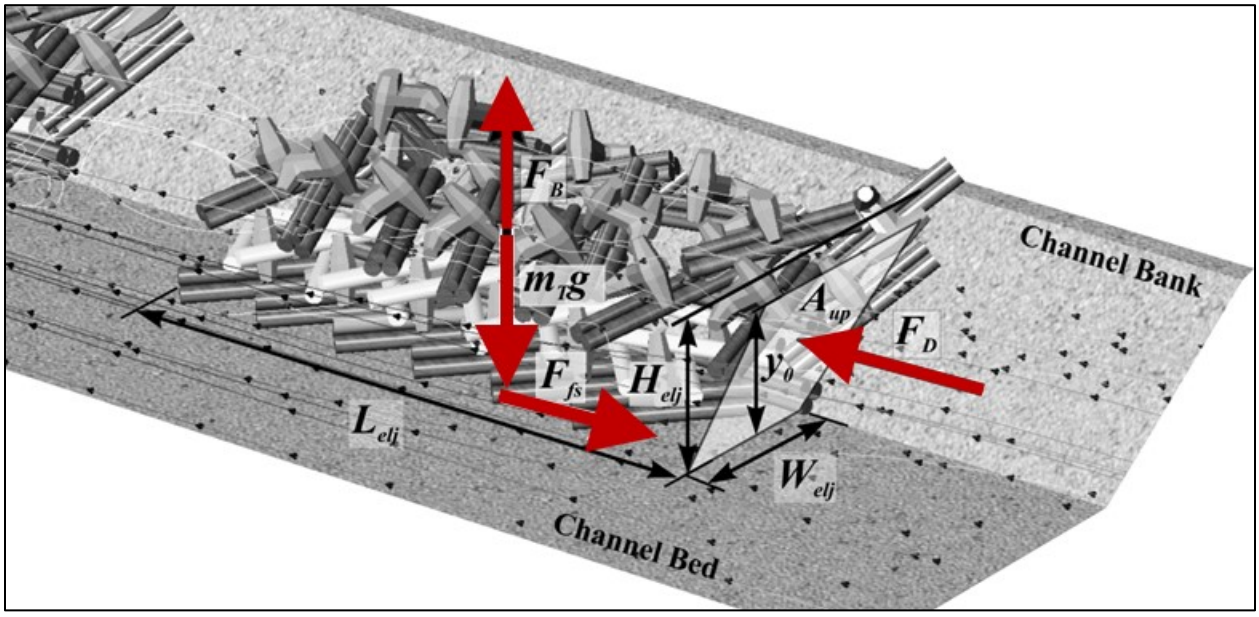


Source: FHWA.

**Figure 86. Schematic. Forces acting on an ELJ under hydrodynamic loads.**

A single ELJ structure becomes unstable against flow attack when the drag force ($F_D$) on the ELJ structure exceeds the resisting force ($F_{fs}$). When this occurs, the ELJ will start to move or slide, causing the structure to fail. This analysis only considers installation of the ELJ on the surface of

the channel bed and bank with no embedment or supplemental anchoring of the ELJ unit. The analysis also only considers longitudinal forces. Within this framework, the ELJ is stable when the resisting force exceeds the drag force, as illustrated in equation 6:

$$F_{fs} \geq F_D \tag{6}$$

Resisting force ($F_{fs}$) is defined in equation 7 as follows:

$$F_{fs} = (m_T g - F_B) \cdot \mu \tag{7}$$

Where:

$F_B$ = buoyant force.
$m_T$ = total mass of the ELJ unit.
$g$ = acceleration resulting from gravity.
$\mu$ = friction coefficient between the ELJ and the streambed.

Drag force ($F_D$) is defined in equation 8 as follows:

$$F_D = \frac{1}{2} C_D \rho A_{up} V_U^2 \tag{8}$$

Where:

$C_D$ = drag coefficient.
$\rho$ = density of water.
$A_{up}$ = effective projected area of the upstream face of the ELJ unit.
$V_U$ = uniform upstream flow velocity.

The relationship of the destabilizing forces (drag and buoyancy) to the stabilizing force (the ELJ weight in contact with the streambed) is described by substituting equation 7 into equation 6 to yield the following in equation 9:

$$m_T g \mu \geq F_D + F_B \mu \tag{9}$$

Based upon the geometry and total average material density of the ELJ unit, the ELJ total mass can be expressed as illustrated in equation 10:

$$m_T = \forall_{elj} \rho_{elj} = \left(W_{elj} L_{elj} H_{elj}\right) \rho_{elj} \tag{10}$$

Where:

$\forall_{elj}$ = volume of the ELJ unit.
$W_{elj}$ = base width of the ELJ unit.
$L_{elj}$ = length of the ELJ unit.
$H_{elj}$ = height of the ELJ unit.
$\rho_{elj}$ = average density of the ELJ unit.

The average density of a single ELJ structure will be affected by the total number and type of elements (e.g., log–dolos bundles and logs with rootwads) and by the packing density and interlocking of these elements within the ELJ unit.

Buoyancy force ($F_B$) is estimated as shown in equation 11:

$$F_B = \left(W_{elj} L_{elj} y_0\right) \rho g \tag{11}$$

Where:

$y_0$ = flow depth at the ELJ unit.

$W_{elj}$ = base width of the ELJ unit.

The design flow depth near the ELJ is assumed to be the same as or similar to the flow depth in the main channel for wide and shallow rivers.

Substituting equation 8, equation 10, and equation 11 into equation 9 and then solving for ELJ height, the stability relation can be expressed as shown in equation 12:

$$H_{elj} \geq \frac{\rho}{\rho_{elj}} \left( \frac{C_D V_U^2}{2 L_{elj} g \mu} + 1 \right) y_0 \tag{12}$$

Restating the equation as an equality, as shown in equation 13, yields the following:

$$H_{elj-MIN} = \frac{\rho}{\rho_{elj}} \left( \frac{C_D V_U^2}{2 L_{elj} g \mu} + 1 \right) y_0 \tag{13}$$

Equation 13 defines the minimum ELJ height required for hydrodynamic stability for given flow depth and approach velocity, which are its primary parameters. The equation also illustrates the effect of $\rho$ on the unit's structural hydraulic stability, which is counterbalanced by $\rho_{elj}$. Thus, $\rho_{elj}$ becomes a sensitive parameter and plays a major role in the hydraulic stability of the ELJ structure. Moreover, the equation shows how the minimum ELJ height can be adjusted by varying ELJ length.

Figure 87 displays a plot for the hydraulic stability relationship based on equation 13 for three different ELJ design lengths, where the vertical axis is presented as a ratio of structure height to flow depth ($H_{elj-MIN}/y_0$) plotted against the Froude number. The analysis used a $C_D$ value of 1.75 and a $\mu$ value of 0.6. The $C_D$ value was determined from the flume force measurements and CFD modeling. The $\mu$ value was derived from pulling tests of model log–dolos bundles on rough beds representative of field conditions to determine the friction angle. The friction coefficient is estimated as the tangent of the friction angle. The analysis also used the spatially averaged $V_U$ value immediately upstream of the ELJ unit.

Figure 87 illustrates an effective framework for evaluating the hydraulic stability of an ELJ for different design lengths and for a range of approach flow conditions, represented by the Froude number, showing how flow depths and approach velocities have an impact on the hydraulic stability of an ELJ. The range of Froude numbers is representative of design conditions in the field.

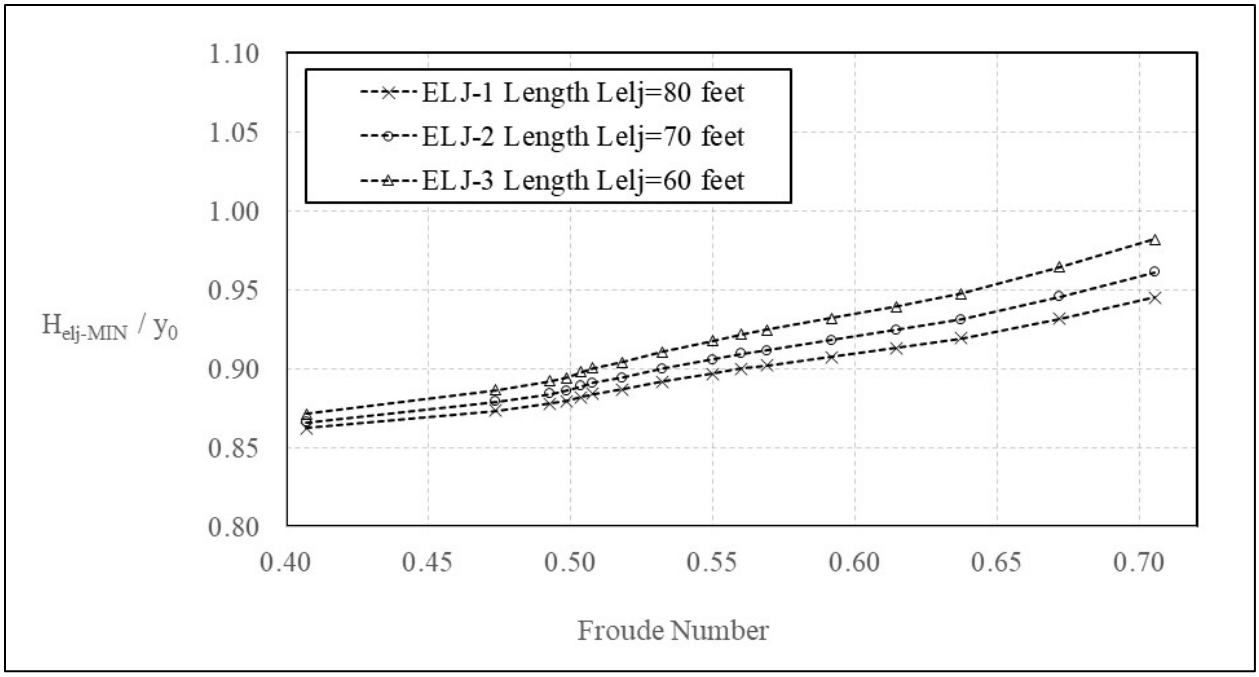


Source: FHWA.

**Figure 87. Graph. Minimum structure–height to flow–depth ratio required for stability of three ELJ lengths.**

The stability model described in equation 13 was validated with flume experiments (phase III) in which the standard ELJ installation was tested under both partially submerged and fully submerged conditions. In these tests, *Fr* ranged from 0.41 to 0.55, and the ELJ length equaled 75 ft. Referencing figure 87, the ratio of stable structure height to the flow depth should be no less than approximately 0.87 to 0.92 depending on the Froude number. Since the ELJ unit is fully submerged with a ratio less than 1, the stability model described in equation 13 predicts that ELJ units can be stable for some fully submerged conditions.

During phase III, full submergence was tested in the flume in runs III-5 and III-6 (refer to table 10 for the run parameters) and resulted in failure of the ELJ at the point where the structure height-to-flow-depth ratio was equal to 0.96. This contradicts the prediction of stability down to a ratio of 0.92. The difference in result is mainly because the stability model does not consider channel-bank erosion. During the flume experiments, researchers observed that channel-bank erosion developed for the fully submerged ELJ condition. When ELJ structures became inundated, highly turbulent flow developed above the ELJ on the top of the unprotected channel bank. Consequently, bank erosion occurred rapidly, affecting the interlocking of the elements and increasing the vulnerability of the upstream face of the ELJ unit to hydrodynamic forces.

Additional phase III experiments in the flume, including runs III-8 and III-9, demonstrated that reinforcing the upstream face (failure zone) increased hydraulic stability but did not mitigate the bank erosion induced by the highly turbulent erosive flow right above and between the ELJ elements and the existing bank top.

## HYDRAULIC DESIGN CONSIDERATIONS FOR ELJ STRUCTURES

When properly designed, ELJs can be structurally stable against hydrodynamic forces and streambed scour. Moreover, scour experiments and CFD modeling in the prototype scale showed the effectiveness of ELJs in deflecting river flow away from an eroding bank area and reducing velocities and shear stresses along the unstable, eroding bank area in the gap between ELJ units in series. However, flume experiments showed that the ELJs do not perform well for fully submerged conditions, suggesting that the design of ELJ height should include some sort of safety factor (*SF*) or freeboard (*FB*) to avoid unintended submergence of the ELJs. *FB* is defined as the distance from the top of the ELJ to the water surface ($H_{elj} - y_0$).

Adding ELJs to a stream or river channel changes flow conveyance patterns, preventing erosion and protecting banks. Hydraulic modeling of pre- and post-installation conditions is appropriate to determine whether changes in conveyance might create unintended erosion or instability issues elsewhere in the channel. The risks of unintended consequences may be greater for ELJ units that are large compared with the size of the river. While no specific limits for ELJ size compared with river width are suggested in this research report, hydraulic modeling is a useful tool for identifying potential problems.

### Safety Factors and Freeboard

Safety factors can be embedded as coefficients in the design equations or as correction coefficients for a few parameters, such as flow velocities. HEC-23 Design Guideline 4 for riprap revetment recommends an *SF* equal to or larger than 1.1 when designing bank revetments used to provide erosion protection for streambanks (Lagasse et al. 2009). Safety factors greater than 1.1 are recommended where there is significant potential for impact from large debris or uncertainty in the estimated design velocity. However, there is likely much more uncertainty associated with ELJ installations compared with riprap revetment. USBR and ERDC (2016) employ *SF*s ranging from 1.5 to 2.0.

Figure 88 displays an example of applying an *SF* of 1.3 compared with 1.5 in equation 13 based on design uncertainties, such as the estimated velocity distribution in meandering rivers, and because of the potential for woody debris carried by the river entangling on the ELJ and creating additional destabilizing forces. This was observed during the flume stability experiments, when dislodged logs with rootwads from ELJ units upstream were entangled by the downstream ELJ installations.

Freeboard is another approach for considering uncertainty in the design. A minimum *FB* of 3 ft is recommended by the WFLHD as shown in appendix A for the Upper Hoh River Road project. Figure 89 provides a comparison of a family of curves from figure 87 with a set of curves where 3 ft is added to the calculated ELJ height from equation 13. Since the minimum height values computed from equation 13 are less than the water depth, adding 3 ft to the minimum ELJ height will not provide 3 ft of freeboard. In this case, the required minimum height with 3 ft of freeboard is the water-surface depth plus 3 ft.

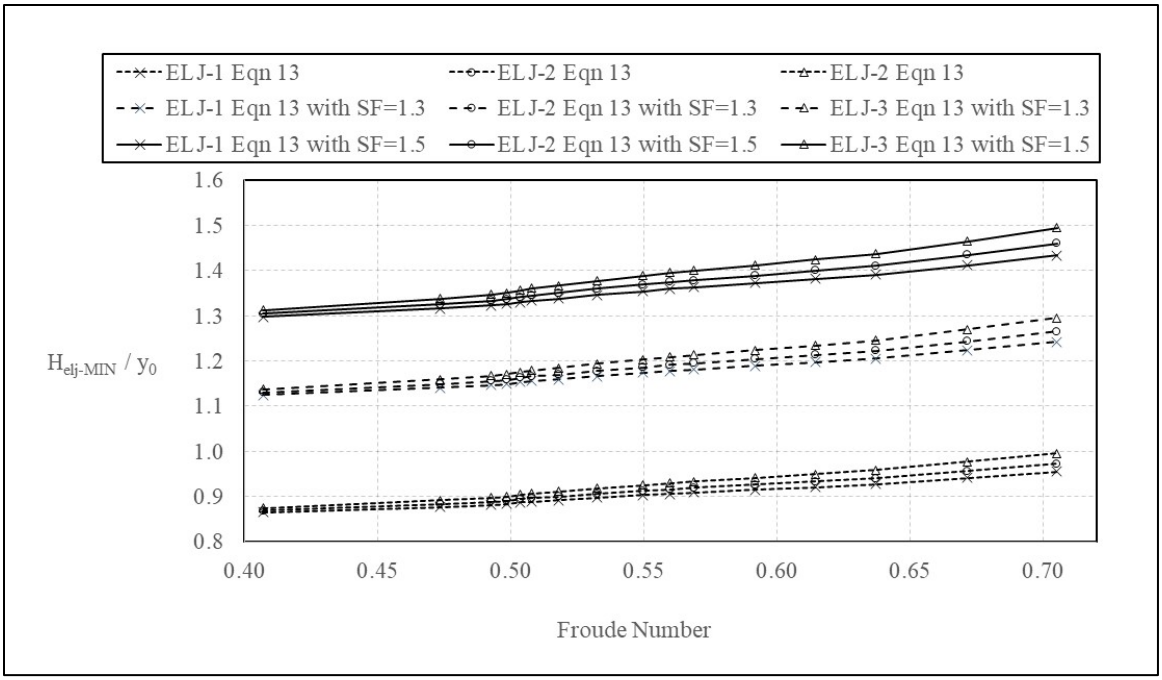


Source: FHWA.

**Figure 88. Graph. Hydraulic stability model from equation 13 compared with curves with *SF*s of 1.3 and 1.5.**

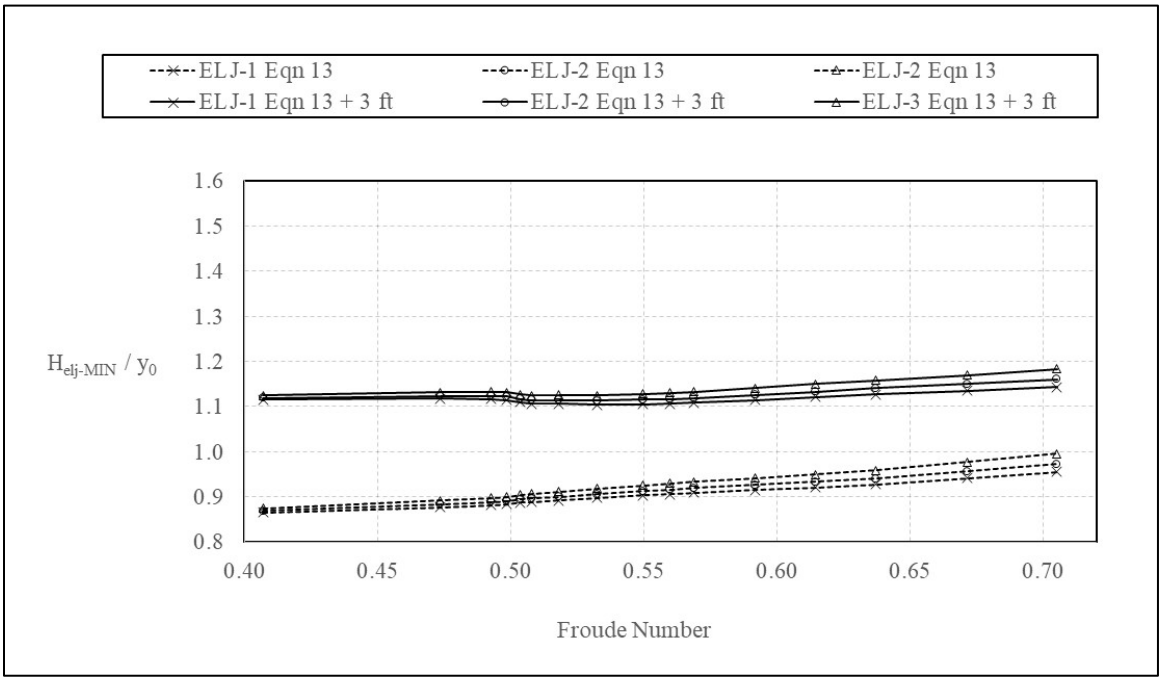


Source: FHWA.

**Figure 89. Graph. Hydraulic stability model from equation 13 compared with curves with 3 ft added to the minimum value.**

The recommended design procedure is to first apply the appropriate *SF* to the minimum ELJ height computed from equation 13 (based on the stability model), as shown in equation 14:

$$H_{elj-SM} = \left[\frac{\rho}{\rho_{elj}}\left(\frac{C_D V_U^2}{2L_{elj} g \mu} + 1\right) y_0\right] SF \quad (14)$$

Where $H_{elj–SM}$ is the minimum height of the ELJ unit based on the stability model.

This computation defines the minimum ELJ height required for hydrodynamic stability for a given flow depth and approach velocity. The equation includes an *SF* with a recommended value of no less than 1.5 to account for uncertainties in the hydraulic conditions, materials, and construction.

For the type of ELJs used in this research report, a $C_D$ of 1.75 is used in the design equation. The value of $\mu$ is taken to be 0.6 based on a friction angle of 31 degrees for the bed material. For other bed materials with a different friction angle, the friction coefficient should be taken as the tangent of the friction angle.

This equation provides an estimate of height, ensuring that that ELJ unit is above the water surface elevation during design flow conditions. As previously noted, a minimum *FB* requirement of 3 ft is recommended. To assess this, compute the freeboard-based height, as shown in equation 15:

$$H_{elj-FB} = y_0 + FB \quad (15)$$

Where $H_{elj–FB}$ is the minimum height of the ELJ unit based on the *FB* requirement.

Height estimates from both the stability model and freeboard are then compared. The larger of the two is taken as the recommended minimum height of the ELJ unit, as represented in equation 16:

$$H_{elj} = max\left[H_{elj-SM}, H_{elj-FB}\right] \quad (16)$$

**Packing and Material Density**

Stability of an ELJ unit requires sufficient material density and packing density to resist buoyancy and drag forces. A tighter packing density using 33 log–dolos bundles (rather than 25) in addition to 14 rootwads and 7 key dolosse was employed in the flume experiments. This resulted in a packing density of 0.001 log–dolos bundles per cubic foot of ELJ unit volume and a density of 0.00042 rootwad logs per cubic foot of ELJ unit volume. This higher packing density resulted in the densities and void ratios summarized in table 13. The unit weights used for the single elements in this analysis are wood at 30 lb/ft$^3$, concrete dolos at 150 lb/ft$^3$, and water at 62.4 lb/ft$^3$. ELJ units with lower densities, higher void ratios, or both will exhibit a reduction in stability.

**Table 13. Density and void ratios for 33 log–dolos ELJ units (excluding key dolosse).**

| Parameter | Prototype | Model |
|---|---|---|
| Net density (lb/ft$^3$) | 72.9 | 71.5 |
| Void ratio | 0.71 | 0.71 |
| Submerged density (lb/ft$^3$) | 65.5 | 65.1 |

Table 14 summarizes the minimum recommendations for packing density, net density, and submerged density of the ELJ units. The minimum packing densities are used to estimate the number of log–dolos bundles and rootwads required in each unit.

**Table 14. Minimum packing density and material density.**

| Parameter | Minimum Requirement |
|---|---|
| Log–dolos bundle packing density (bundles/ft$^3$) | 0.001 |
| Rootwad packing density (rootwad logs/ft$^3$) | 0.00042 |
| Net density (lb/ft$^3$) | 72.9 |
| Submerged density (lb/ft$^3$) | 65.5 |

The volume of the ELJ unit is computed from the dimensions $W_{elj}$, $H_{elj}$, and $L_{elj}$ combined with the side slope of the unit on the stream side and streambank side. As shown in figure 21, the side slope (H:V) of the ELJ unit on the stream side should be 1:1. The side slope on the streambank side may vary with conditions, but should allow for good installation of the ELJ unit, preferably between 1:1 and 1.5:1. Flatter streambank slopes are acceptable, but will require more material to complete the ELJ units.

**ELJ Design Layout Recommendations**

One of the goals for this research study was to test and, if possible, enhance the design of ELJs with dolosse initially developed by the WFLHD. This section presents an improved recommended installation sequence with particular attention to layer B. The installation sequence resulted from an assessment of the physical modeling experiments (phase I). Its goal is to optimize the ELJ installation against flow attack. The recommended installation procedure is as follows:

1. Place layer A, as shown in figure 90, based on the WFLHD design drawings.

2. Place the first part of the layer B plan, with seven deflector log–dolos bundles, on the existing unstable bank, as illustrated in figure 91. Care must be taken with the placement of the two log–dolos bundles located on the upstream end of the ELJ unit, with the main objective being to close any potential gaps between the bank top and top elements of the ELJ unit so the approach flow will be efficiently slowed and deflected from the upstream face into the main channel.

3. Place six connector log–dolos bundles on top and rotated in a direction similar to the approach flow, as shown in figure 92. This figure illustrates an efficient way to connect the deflector log–dolos bundles seated on the existing bank. An important parameter in this approach is to transfer effectively the weight of the log–dolos bundles located on top downward onto the deflector log–dolos bundles on the bottom.

4. Place an additional seven deflector or connector log–dolos bundles in layer B to connect the elements installed on the bank with the elements from layer A, as shown figure 93. In addition, three logs with rootwads should be added to layer B, filling the large voids encountered in the system.

5. Place additional deflector log–dolos bundles and four logs with rootwads to connect elements and fill unintended voids between the elements installed, as shown in figure 94.

6. Add key dolosse at the front face of the ELJ for additional hydraulic stability (optional).

7. Measure the volume of the ELJ unit. Calculate log–dolos bundle, rootwad, and net densities as well as the void ratio. Log–dolos bundle and rootwad densities should be no less than 0.001 and 0.00042, respectively. Net density should be no less than 71.5 $lb/ft^3$, and the void ratio should be no greater than 0.71.

Figure 95 shows an elevation view of the upstream face for the completed installation of the ELJ unit. As noted previously and illustrated in the figure, the H:V slope of the channel bank may vary between 1:1 and 1.5:1 based on existing conditions and recommendations provided by WFLHD.

This research did not evaluate alternative spacing lengths between ELJ units. Therefore, the recommended design adopts the 30-ft spacing recommended by WFLHD, which was tested in the flume experiments and used in the CFD model of the MP 4.0 site in prototype scale.

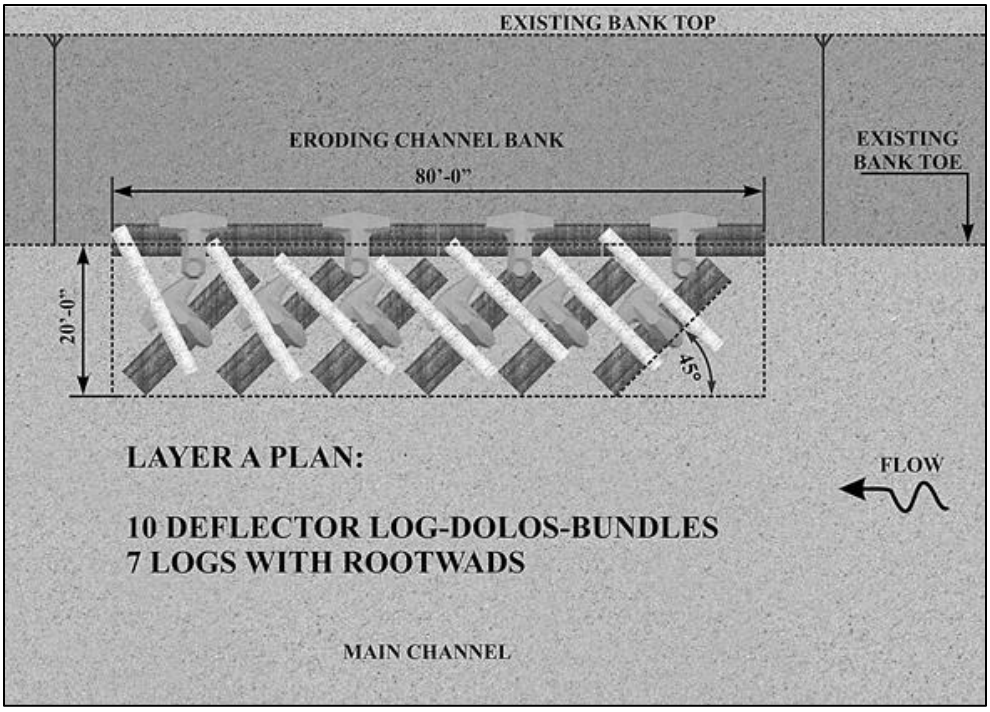


Source: FHWA.

**Figure 90. Graphic. Plan view of the installation sequence of an ELJ unit (layer A).**

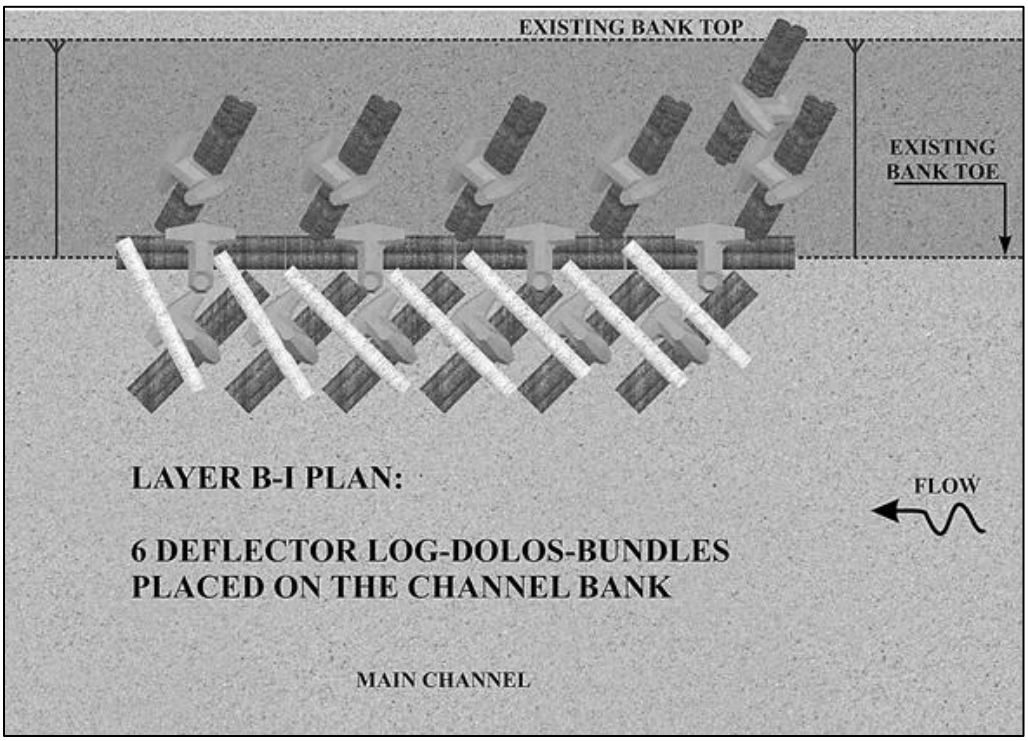


Source: FHWA.

**Figure 91. Graphic. Plan view of the installation sequence of an ELJ unit (layer B-I).**

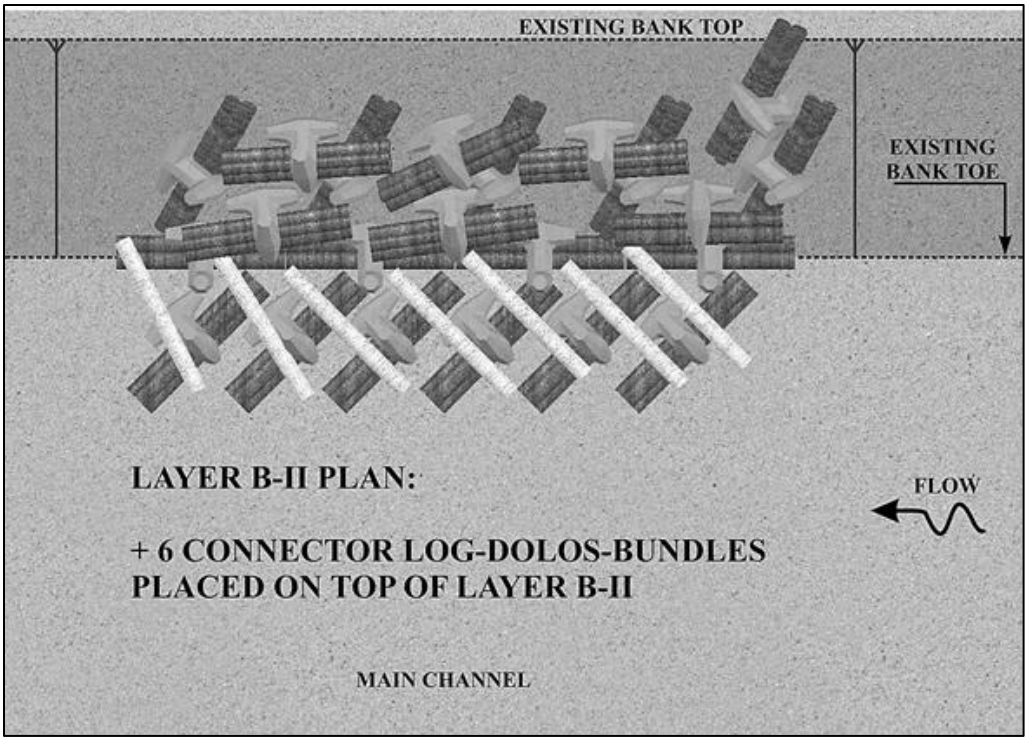


Source: FHWA.

**Figure 92. Graphic. Plan view of the installation sequence of an ELJ unit (layer B-II).**

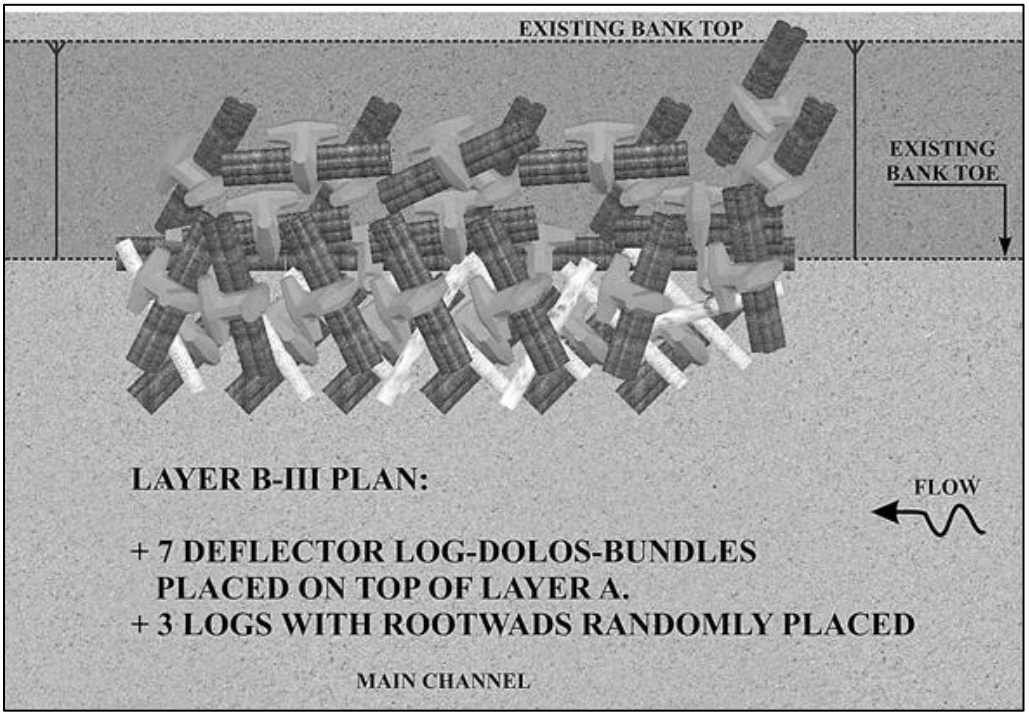


Source: FHWA.

**Figure 93. Graphic. Plan view of the installation sequence of an ELJ unit (layer B-III).**

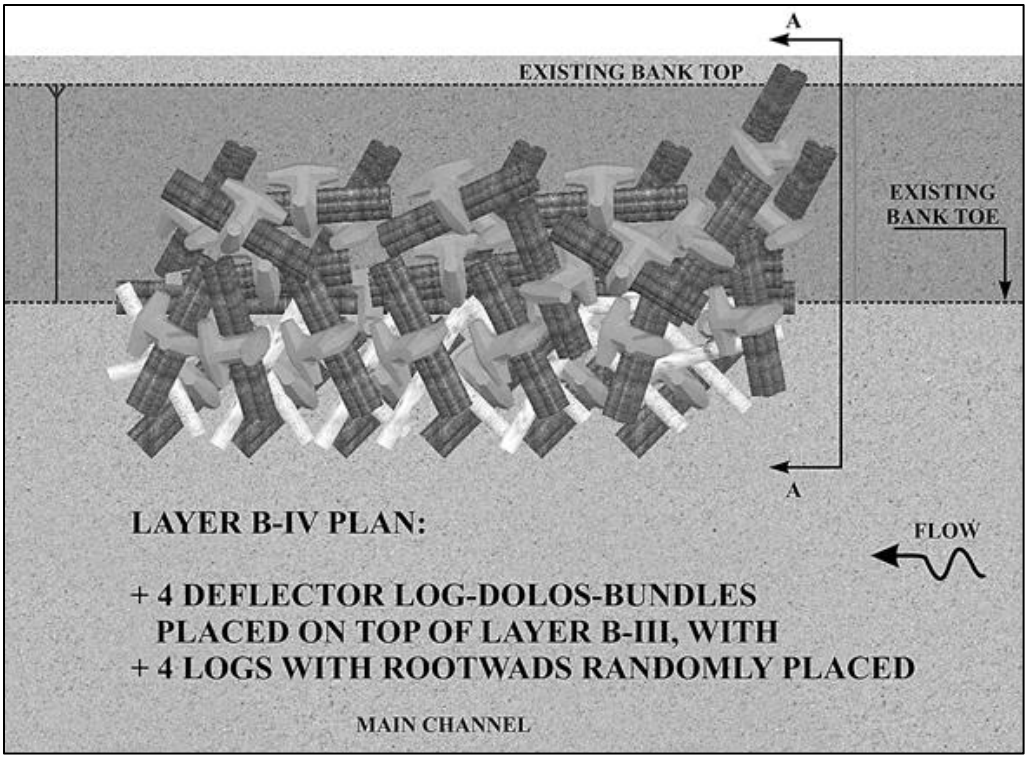


Source: FHWA.

**Figure 94. Graphic. Plan view of the installation sequence of an ELJ unit (layer B-IV).**

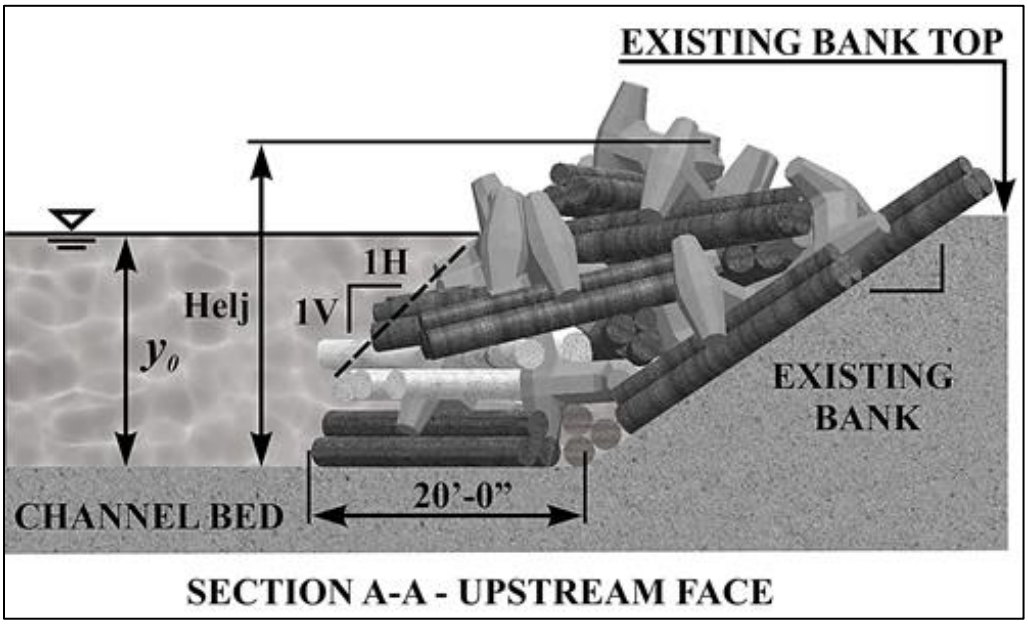


Source: FHWA.

**Figure 95. Graphic. Elevation view of the final ELJ installation.**

# CHAPTER 6. SUMMARY

Engineers at WFLHD are installing long-term stream-bank stabilization solutions that are intended both to stabilize the highway infrastructure and to minimize environmental impacts. ELJs with precast concrete dolosse are being considered for use in the Upper Hoh River Road bank stabilization project. These constructed logjams mimic those found in nature. In a natural river system, logjams typically form when large trees fall into the water and become embedded in the riverbed, creating an obstruction that captures additional logs and debris moving downstream. Such logjams can redirect the channel and mitigate destructive erosive forces. As an additional benefit, the logs and debris can create or enhance fish habitat.

The researchers tested a 1:25 scale model of a proposed ELJ design in a flume at TFHRC under different flow conditions on both movable bed and bank material and a fixed bed and bank. The team complemented physical modeling with CFD modeling to investigate the stability of proposed ELJ installations during floods and to advance the design of ELJs for stream-bank stabilization.

Based on the cases evaluated, several findings were developed from this research project:

- ELJs proved to be effective in deflecting high-velocity approach flow away from the erodible streambank and into the main channel.
- Drag coefficients and friction factors were derived for this type of ELJ unit based on force measurements and CFD modeling.
- The effectiveness of important structural modifications to the ELJs, such as placement of key dolosse, addition of riprap, and partial burial of the ELJ, was determined.
- Results obtained from the ELJ model with movable bed and bank material showed that localized streambed scour around this structure does influence its stability.
- A repeatable ELJ unit design can provide structural stability against high-velocity flows and streambed scour with an appropriate combination of wood and ballast meeting specific density- and void-ratio requirements.

For ELJs to be effective, they must be stable and effectively protect the erodible bed and bank. As developed in this study, stability depends on ensuring sufficient packing density of the ELJ elements, such as the log–dolos bundles; sufficient anchoring; alignment with the flow field; and an ELJ unit height that extends above the anticipated water surface under design flow conditions. In this study, anchoring was achieved by providing sufficient ballast (the concrete dolos) rather than with pins, piles, or other strategies. The development of a design equation and physical model testing ensured a sufficient height for stability that extended above the anticipated water surface.

As part of the stability analysis, drag coefficients were developed with a value of approximately 1.75 when using the approach velocity and full-frontal area of the ELJ to estimate longitudinal drag forces. Transverse forces were measured to be minor and were, therefore, neglected in the force balance analyses.

Based on the physical experiments, a friction factor was also estimated to determine the friction angle. For this study, a value of 0.6 was estimated based on a friction angle of 31 degrees and provided consistent results. However, the ability to transfer this value to other sites or to reliably estimate a friction angle given the variability of ELJ designs and bed materials has not been evaluated.

With respect to scour around the base of the ELJ unit, scour was observed in the channel bed, but not with sufficient magnitude to cause failure of the ELJ unit. Strategies for reducing scour, such as locating key dolosse at the base of the ELJ unit or adding riprap to the bed in the ELJ voids, tended to increase or not affect scour and did not improve stability of the unit. Therefore, the use of key dolosse at the base of the ELJ parallel to the channel and installation of a riprap layer are not recommended. Other strategies such as partially burying the lowest layer of log–dolos bundles or placing key dolosse at the upstream face of the ELJ unit provide minor benefit in increasing hydraulic stability but do not protect against bank erosion.

Channel-bank erosion was consistently observed when the ELJ unit became submerged even if the unit remained stable. This led to the recommendation that the ELJ unit must extend above the anticipated water-surface elevation. It was also observed that strategies that reduced channel bed scour, as described previously, did not prevent channel-bank erosion.

Several design recommendations emerged from this research related to ELJ height, packing density, unit spacing, and safety factors. ELJ height recommendations are based on a force stability analysis that estimates the minimum recommended height with the further restriction that the ELJ not be fully submerged under design conditions. In addition, maximizing packing density is important for increasing stability by adding mass, reducing the porosity of the unit, and ensuring the log–dolos bundles and rootwad logs interlocked firmly.

While the researchers did not broadly study spacing between ELJ units, they did confirm the 30-ft spacing developed by WFLHD as reasonable to protect an erodible channel bank. In addition, the spacing provides habitat diversity and reduces the cost of installation compared with a continuous installation without spacing between units.

The researchers also evaluated safety factors, including the use of freeboard. There are many uncertainties in ELJ design, including hydrologic uncertainty, variations in materials and installation practices, possibility of interaction with large woody debris, and others. A safety factor is strongly recommended for selecting an ELJ height. This study illustrated the use of an *SF* of 1.5 for the Upper Hoh River Road project.

The results of this study are intended to be useful for other projects. Variations in materials, channel bed and bank conditions, hydraulic conditions, drag coefficients, and other parameters require that the designer consider the site-specific characteristics before adapting these findings to other sites. However, the methods presented in this study provide a template for adapting these findings to other sites.

This research achieved the goal of creating environmentally friendly stream-bank protection and local fish habitat. Findings from this research should be of considerable interest to river engineering designers who may build similar structures for road-bank stabilization projects.

## APPENDIX A. WESTERN FEDERAL LANDS HIGHWAY DIVISION ELJ DESIGN DRAWING

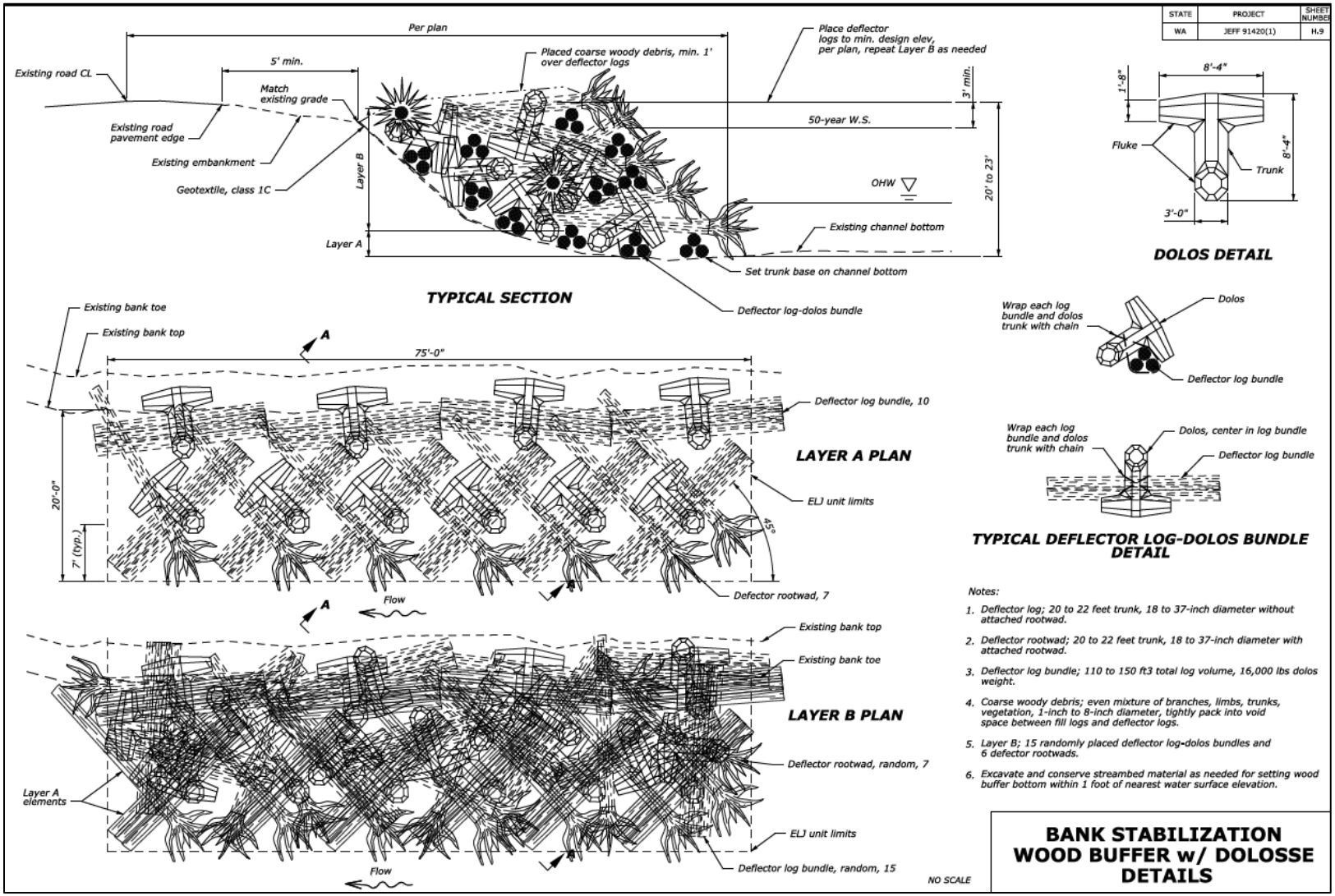


Source: FHWA.

**Figure 96. Drawing. WFLHD design details.**

# APPENDIX B. DESIGN EXAMPLE

This appendix contains an example of an ELJ design based on the Hoh River sites at MP 4.0 and MP 7.8 described in chapter 1. For ELJs composed of log–dolos bundles and rootwads, implementers should follow these design steps:

1. Determine the appropriate hydrologic design conditions and compute preinstallation hydraulic conditions.
2. Select trial log and dolos dimensions, ELJ unit dimensions, and spacing consistent with site characteristics.
3. Estimate an initial ELJ unit height ($H_{elj}$).
4. Select densities for log–dolos bundles, rootwad packing, and materials.
5. Validate initial assumptions and revise design, if necessary.
6. Lay out ELJ unit.

These steps are described in the following sections as applied to the MP 4.0 and MP 7.8 sites, which have similar conditions.

## STEP 1: DETERMINE HYDROLOGIC AND HYDRAULIC DESIGN CONDITIONS

The hydrologic design event should be selected based on applicable design criteria for the roadway or project. For this example, the 0.02 annual exceedance probability event (50-yr return period) is selected. The estimated 50-yr design discharge is 58,000 $ft^3/s$ in the Hoh River with active channel widths ranging from 250 to more than 400 ft at the locations of interest.

A hydraulic model should then be applied to determine the average velocity ($V_U$) and flow depth ($y_U$) upstream of the anticipated ELJ installation. In this example, the hydraulic model yields an average velocity of 12.1 ft/s and a depth of 15 ft resulting in a Froude number ($Fr$) of 0.55. The design methodology is applicable for a range of Froude numbers between 0.2 and 0.55.

## STEP 2: SELECT TRIAL DIMENSIONS

Implementers will next make an initial trial selection of dimensions for the logs and dolosse and the ELJ units. The log length and diameter should be chosen based on available materials, dimensions of wood in natural logjams in the area (if any), the flow depth ($y_U$), and the channel width. If onsite materials will be used, the availability of existing wood informs the selection. Log lengths should be roughly equivalent to the flow depth to provide a good opportunity for interlocking between log–dolos bundles within the ELJ units. Channel width should be considered so that the bundles do not unnecessarily constrict the channel. For the design depth of 15 ft determined in the previous step, somewhat longer log lengths are needed. Therefore, 20-ft lengths of wood with diameters of 19 to 25 inches are chosen.

The dolos dimensions should be compatible with the log dimensions and achieve the necessary packing and density requirements described in a later step. For the initial trial dimensions of the dolosse, the relationships on which this research report are based can be used. For a 20-ft log, a dolos dimension of 8 ft 4 inches can be used. Three logs and one dolos are selected as the initial

log–dolos bundle. An initial trial dimension of the ELJ unit should be selected based on the log length as follows:

- To allow for the placement of the log–dolos bundles, set the initial base width ($W_{elj}$) equal to the log length, which is 20 ft in this example.
- Set the initial longitudinal $L_{elj}$ within a range of three to four times the log length, which is between 60 and 80 ft in this example; therefore, a 75-ft length is selected.
- Set initial spacing between multiple ELJ units ($L$) to 1.5 $W_{elj}$, which is 30 ft in this example.

Initial ELJ unit dimensions and spacing may be adjusted slightly to fit the site.

**STEP 3: SELECT ELJ UNIT HEIGHT**

The ELJ height ($H_{elj}$) should be estimated from the stability model and a minimum freeboard to allow the unit to extend above the water surface under design conditions. The minimum height based on the stability model was defined previously in equation 14. Using the minimum recommended $SF$ of 1.5, the stability model minimum height is calculated as shown in equation 17:

$$H_{elj-SM} = \left[\frac{\rho}{\rho_{elj}}\left(\frac{C_D V_U^2}{2L_{elj}g\mu} + 1\right) y_0\right] SF = \left[\frac{62.4}{72.9}\left(\frac{1.75(12.1)^2}{2(75)(32.2)(0.6)} + 1\right) 15\right] 1.5 = 21 \text{ ft} \quad (17)$$

Where:

$H_{elj-SM}$ = minimum height of the ELJ unit based on a stability model.
$\rho$ = density of water.
$\rho_{-}$ = average density of the ELJ unit (unsubmerged). (Initial value = 72.9 lb/ft$^3$.)
$y_0$ = flow depth at the ELJ unit.
$V_U$ = uniform upstream flow velocity.
$C_D$ = drag coefficient (1.75).
$L_{elj}$ = length of the ELJ unit.
$g$ = acceleration resulting from gravity.
$\mu$ = friction coefficient between the ELJ and the streambed (0.6).
$SF$ = safety factor.

The second estimate of $H_{elj}$ is based on the minimum freeboard requirement, $FB$, as described in equation 15, using a minimum recommended freeboard of 3 ft, as illustrated in equation 18:

$$H_{elj-FB} = y_0 + FB = 15 + 3 = 18 \text{ ft} \quad (18)$$

Compare the height estimates from both the stability model and freeboard, and take the larger of the two as the recommended minimum height of the ELJ unit, as described in equation 16 and illustrated in equation 19:

$$H_{elj} = max\left[H_{elj-SM}, H_{elj-FB}\right] = max[21, 18] = 21 \text{ ft} \quad (19)$$

## STEP 4: SELECT ELJ UNIT PACKING AND MATERIAL DENSITY

Stability of the ELJ units relies on a combination of sufficient material density and packing density to resist buoyancy and drag forces. Table 14 summarizes the minimum density requirements for the components included in the ELJ unit as well as the materials used in those components.

Use minimum packing densities to estimate the number of log–dolos bundles and rootwads required in each unit based on the material properties and the volume of the ELJ unit. For this example, the ELJ unit has a gross cross-sectional area of 530 $ft^2$ based on ELJ H:V slopes of 1:1 on the streamside and 1.5:1 on the channel bank. With a length of 75 ft, the total gross volume of the ELJ is 39,750 $ft^3$. Based on table 14, the minimum number of log–dolos bundles is 39,750 × 0.001 = 40, and the minimum number of rootwad logs (rounding up to the nearest whole unit) is 39,750 × 0.00042 = 17.

The net density of the materials in the ELJ unit should also be computed based on the proportion of logs, dolosse, and rootwads; their dimensions; and their unit weights. The net density should be no less than the value given in table 13. The required minimum submerged density shown in the table implies a maximum void ratio in the ELJ unit of 0.71.

## STEP 5: VALIDATE INITIAL ASSUMPTIONS

Initial assumptions as to log lengths as well as values for $y_0$, ELJ dimensions $W_{elj}$ and $L_{elj}$, and $\rho_{elj}$ should be used to estimate $H_{elj}$. The hydraulic modeling with the preliminary ELJ design in place should be compared to the initial velocity and depth values. The initial assumptions about material properties should also be validated against those used in the original estimates. If significantly different, the steps should be repeated until there is no further change in the values.

## STEP 6: LAY OUT AND PLACE ELJ UNIT

Finally, the ELJ layout follows the recommended placement described in figure 90 through figure 94. The base layer (layer A) of log–dolos bundles and rootwads should be placed on the streambed to provide a foundation for the remaining ELJ installation. The remainder (layer B) will be placed in several stages. It is important that the log–dolos bundles and rootwads be interconnected so that the ELJ unit acts as a single structure. The layout and placement for this example is based on 40 log–dolos bundles and 17 rootwads for each ELJ unit:

1. Place layer A as shown in figure 90, but with a 75-ft $L_{elj}$.

2. Place the first stage of layer B with deflector log–dolos bundles on the unstable bank as illustrated in figure 91. Care must be taken with the placement of the two log–dolos bundles located on the upstream end of the ELJ unit. The main objective is to close any potential gaps between the bank top and top elements of the ELJ unit so the approach flow will be efficiently slowed and deflected from the upstream face into the main channel.

3. Place additional connector log–dolos bundles on top. Rotate them to be approximately parallel to the approach flow for layer B-II, as shown in figure 92. This is an efficient way to connect the deflector log–dolos bundles seated on the streambank. Placement must allow effective transfer of the weight of the log–dolos bundles located on top to the deflector log–dolos bundles on the bottom. Because this example requires 40 log–dolos bundles, a total of 8 bundles are placed in this layer.

4. Place an additional set of deflector or log–dolos bundles in layer B-III to connect the elements installed on the bank with the elements from layer A, as shown figure 93. In addition, logs with rootwads are added to layer B to fill the large voids. Because this example requires 40 log–dolos bundles and 17 logs with rootwads, a total of 10 bundles and 5 logs with rootwads are placed in this layer.

5. Place additional log–dolos bundles and logs with rootwads to connect elements and fill voids between the elements for layer B-IV, as shown in figure 94. Because this example requires 40 log–dolos bundles and 17 logs with rootwads, a total of 6 bundles and 5 logs with rootwads are placed in this layer.

6. Add individual dolosse at the front face of the ELJ for additional hydraulic stability (optional). In this example, none are added.

7. Measure the volume of the ELJ unit. Calculate log–dolos bundle, rootwad, and net densities as well as the void ratio. Confirm all densities remain within satisfactory limits. Figure 95 shows an elevation view of the upstream face of the completed installation of the ELJ unit.

## REFERENCES


Abbe, T. B., A. P. Brooks, and D. R. Montgomery. 2003a. "Wood in River Rehabilitation and Management." In *The Ecology and Management of Wood in World Rivers*, Proceedings of American Fisheries Society Symposium 37, ed. Stan V. Gregory, Kathryn L. Boyer, and Angela M. Gurnell. Bethesda, MD: American Fisheries Society.

Abbe, T. B., G. Pess, D. R. Montgomery, and K. L. Fetherston. 2003b. "Integrating Engineered Log Jam Technology into River Restoration." In *Restoration of Puget Sound Rivers*, ed. D. R. Montgomery, S. Bolton, D. B. Booth, and L. Wall. Seattle, WA: University of Washington Press.

Abbe, T., M. Hrachovec, and S. Winter. 2018. "Engineered Log Jams: Recent Developments in Their Design and Placement, with examples from the Pacific Northwest, U.S.A.," Reference Module in Earth Systems and Environmental Sciences. Netherlands: Elsevier. https://doi.org/10.1016/B978-0-12-409548-9.11031-0, accessed August 7, 2020.

Aquaveo. 2020. Surface-water Modeling System, v. 13.0.6.

Bennett, S. J., S. M. Ghaneeizad, M. S. Gallisdorfer, D. Cai, J. F. Atkinson, A. Simon, and E. J. Langendoen. 2015. "Flow, Turbulence, and Drag Associated with Engineered Log Jams in a Fixed-Bed Experimental Channel." *Geomorphology* 248, no. 1 (November): 172–184. https://doi.org/10.1016/j.geomorph.2015.07.046, accessed August 7, 2020.

CD-adapco. 2013. STAR-CCM+, v. 8.02.

CloudCompare 3D Point-Cloud and Mesh-Processing Software Open Source Project. n.d. CloudCompare v. 2.6.1. https://CloudCompare.org, accessed August 7, 2020.

Einstein, H. A., and N. Chien. 1954. "Similarity of Distorted River Models with Movable Bed." *Transactions of the American Society of Civil Engineers* 121 (1): 440–457.

Gallisdorfer, M. S., S. J. Bennett, J. F. Atkinson, S. M. Ghaneeizad, A. P. Brooks, A. Simon, and E. J. Langendoen. 2014. "Physical Scale Model Designs for Engineered Log Jams in Rivers." *Journal of Hydro-Environment Research* 8 (2): 115–128. https://doi.org/10.1016/j.jher.2013.10.002, accessed August 7, 2020.

Hall, M. and S. Moler. 2006. "Mimicking Mother Nature." *Public Roads* 69, no. 4 (January/February). Available online: https://www.fhwa.dot.gov/publications/publicroads/06jan/05.cfm, accessed August 7, 2020.

Julien, P. Y. 2002. *River Mechanics*, Cambridge, MA: Cambridge University Press.

Kittitas Conservation Trust. 2015. “Cle Elum River Instream Habitat and Side Channel Restoration Project.” Available online: https://www.kittitasconservationtrust.org/projects/cle-elum-river-instream-habitat-side-channel-restoration-project/, accessed August 7, 2020.

Lagasse, P. F., P.E. Clopper, J.E. Pagán-Ortiz, L.W. Zevenbergen, L.A. Arneson, J.D. Schall, and L.G. Girard. 2009. “Bridge Scour and Stream Instability Countermeasures.” *Hydraulic Engineering Circular No. 23*, vol. 2, Report No. FHWA-NHI-09-111. Washington, D.C: Federal Highway Administration.

Papanicolaou, A. N., M. A. Wyssmann, A. Merook, and S. Mohammadi. 2018. *Investigation of Flow and Local Scour Characteristics around Permeable WSDOT Dolotimber Engineered Logjams (ELJ), Final Report*, Report No. WA-RD 821.2. Olympia, WA: Washington State Department of Transportation.

Shields, F. D. and C. V. Alonso. 2012. “Assessment of Flow Forces on Large Wood in Rivers.” *Water Resources Research* 48 (6). Available online: https://doi.org/10.1029/2011WR011547, accessed August 7, 2020

U.S. Bureau of Reclamation. 2004. *Geomorphic Assessment of the Hoh River, Washington: River Miles 17 to 40 between Oxbow Canyon and Mount Tom Creek*. Denver, CO: U.S. Bureau of Reclamation.

U.S. Bureau of Reclamation and U.S. Army Engineer Research and Development Center (USBR and ERDC). 2016. *National Large Wood Manual: Assessment, Planning, Design, and Maintenance of Large Wood in Fluvial Ecosystems: Restoring Process, Function, and Structure*. Boise, ID: USBR. Available online: https://www.usbr.gov/research/projects/download_product.cfm?id=1481, accessed August 7, 2020.

Washington State Recreation and Conservation Office (WSRCO). 2000. “Elwha River Engineered Log Jams.” PRISM Project #99-1313. Last updated November 13, 2018. Available online: https://secure.rco.wa.gov/prism/search/projectsnapshot.aspx?ProjectNumber=99-1313, accessed August 7, 2020.

WSRCO. 2009. “South Fork Nooksack (Mouth to Skookum Cr.) Restoration.” PRISM Project #06-2256. Last updated January 6, 2020. Available online: https://secure.rco.wa.gov/prism/search/projectsnapshot.aspx?ProjectNumber=06-2256, accessed August 7, 2020.

WSRCO. 2012. “Deschutes River ELJ / LWD Design Project.” Project #01-03-10-06. Available online: https://srp.rco.wa.gov/project/150/17578#, accessed August 7, 2020.

Washington State Department of Transportation. 2014. *Improving Stream Habitat and Protecting Roads: WSDOT CED Program Fiscal Year 2014 Report*. Olympia, WA: WSDOT. Available online: http://citeseerx.ist.psu.edu/viewdoc/download;jsessionid=4CF876324880CF1129AA506C7520920D?doi=10.1.1.348.6617&rep=rep1&type=pdf, accessed August 7, 2020.

Xu, Y. and X. Liu. 2017. "Effects of Different In-Stream Structure Representations in Computational Fluid Dynamics Models—Taking Engineered Log Jams (ELJ) as an Example." *Water* 9, no. 2 (February): 110. Available online: https://doi.org/10.3390/w9020110, accessed August 7, 2020.

Recycled
Recyclable

HRDI-40/02-21(WEB)E